POLITECNICO DI MILANO

School of Industrial and Information Engineering
Department of Aerospace Science and Technology

Sensitivity analysis and applicability domain of the Keplerian map approach and application to distant retrograde orbits design

Master Thesis

Candidate:
Lorenzo Chianella
ID: 10746407 / 940482

Supervisor:
Prof. Dr. Camilla Colombo

Co-supervisor:
Lorenzo Giudici

M.Sc in Space Engineering
A.Y. 2020-2021

When referring to this work, full bibliographic details must be given, i.e. Lorenzo Chianella , "Sensitivity analysis and applicability domain of the Keplerian map approach andapplication to Quasi-Satellite Orbits design". 2021, Politecnico di Milano, Master in Space Engineering, Supervisors: Camilla Colombo, Lorenzo Giudici.

Printed in Italy

"Remember to look up at the stars and not down at your feet.
Try to make sense of what you see and wonder about what makes the
Universe exist. Be curious. And however difficult life may seem, there
is always something you can do and succeed at.
It matters that you don't just give up."

Stephen Hawking

Abstract

THE effect of a secondary attractor on the dynamics of a spacecraft orbiting around a primary, has been always a challenge to be modeled in an efficient and, at the same time, accurate way. The equations of the Restricted Three Body Problem accomplish this task, but they require to be numerically integrated since they do not have a close form solution. Such numerical integration results to be expensive in terms of computational time when the motion of the probe shall be predicted for a long period.
In recent years, the Keplerian Map theory was developed with the purpose of approximating the solution of such equations saving time and with good accuracy, possibly with a (semi-)analytical model. Implemented for the first time by Petrosky and Broucke in 1988, the latest evolution of the theory includes in its mathematical model the eccentric motion of the third body and it is obtained without making assumptions on the mass parameter of the system. The approach was applied to propagate the motion of a body in different scenarios, as in the Jovian system or for a Near Earth Asteroid. However, it is still not clear when it is possible or not to approximate the trajectory with good accuracy. In order to know a priori if the Keplerian Map approach can be used without introducing a significant error on the motion prediction, there is the necessity to identify an applicability domain. This region can be identified through a comparison with the solution obtained with the numerical integration of the three-body problem equations.
The aim of this thesis is to determine the Keplerian Map applicability domain. Such purpose is achieved with a sensitivity analysis in which the initial conditions of the spacecraft are made to vary and then propagated. This procedure is performed many times comparing the results with the solution of the three-body problem through a relative percentage error. The output of this analysis are different plots in which the error value is reported in function of some system parameters. By reading these maps graphically, scenarios in which the theory can be applied are recognised.
Finally, after that an applicability domain is defined, the theory is applied to design direct retrograde orbits with the exploitation of an optimisation process, highlighting the advantages in doing that with the Keplerian Map approach.
This thesis project is part of the project COMPASS "Control for Orbit manoeuvring through perturbations for application to space systems". The COMPASS project has received funding from the European Research Council (ERC) under the European Union's Horizon 2020 research and innovation programme (grant agreement No 679086 - COMPASS).

Sommario

MODELLARE in modo efficace e allo stesso tempo accurato l'effetto di un secondo corpo sulla dinamica di uno spacecraft che sta orbitando attorno ad un attrattore primario, è stata da sempre una sfida. Le equazioni del problema dei tre corpi ristretto riescono in ciò, ma richiedono di essere integrate numericamente, non avendo una soluzione in forma chiusa. Questa integrazione numerica risulta essere dispendiosa in termini di tempo computazionale quando il moto del satellite deve essere predetto per un lungo periodo.
Negli ultimi anni, la teoria della Keplerian Map è stata sviluppata con l'intenzione di approssimare con buona accuratezza la soluzione di queste equazioni in modo da risparmiare tempo nell'integrazione, essendo un modello (semi-)analitico. Implementata per la prima volta da Petrosky e Broucke nel 1988, l'ultima evoluzione della teoria include nel suo modello matematico il moto eccentrico del terzo corpo, ed è ottenuta senza fare assunzioni sul parametro di massa del sistema. Questo approccio è stato utilizzato per propagare il moto di un corpo in diversi scenari, come nel sistema Gioviano o per un asteroide vicino alla Terra. Ad ogni modo, non è ancora chiaro quando è possibile o no approssimare la traiettiera con buona accuratezza. In modo tale da sapere a priori se la Keplerian Map può essere utilizzata senza introdurre errori significanti, c'è la necessità di identificare un suo dominio di applicabilità. Questa regione può essere trovata comparando i risultati con quelli numerici proposti dal problema dei tre corpi.
L'obiettivo di questa tesi è di determinare il dominio di applicabilità della Keplerian Map. Tale scopo è raggiunto tramite un'analisi di sensibilità nel quale le condizioni iniziali della particella sono fatte variare e poi propagate. Questa procedura è effettuata molte volte, comparando i risultati con quelli del problema dei tre corpi tramite un errore relativo. L'output sono diversi grafici nei quali è riportato il valore dell'errore in funzione di alcuni parametri del sistema, dai quali è possibile identificare quando le soluzioni convergono.
Infine, dopo che un dominio di applicabilità è stato definito, la teoria viene applicata per progettare orbite retrogradi distanti, sfruttando un processo di ottimizzazione ed evidenziando i vantaggi nel fare ciò con la Keplerian Map.
Questo lavoro di tesi è parte del progetto COMPASS "Control for Orbit manoeuvring through perturbations for application to space systems". Il progetto COMPASS ha ricevuto fondi dall'European Research Council (ERC) per il programma di ricerca e innovazione dell'European Union's Horizon 2020 (accordo di sovvenzione No 679086 - COMPASS).

Acknowledgements

First, I have to express my most sincere gratitude to my Supervisor, Prof. Dr. Camilla Colombo, for giving me the chance to work on a very interesting topic, following my work and supporting me with advice and stimulating talks. The same thanks go to my Co-Supervisor, Lorenzo Giudici. He really motivated and helped me during this period, taking an interest in what I have done as it was his own project.

Then, I have to say thank you to my family, that totally supported me during this amazing journey. From the day I moved out to nowadays, it is as if you have always been beside me. I dedicate to you all the achievements and goals I reached, hoping to make you proud of me again and again. To my mother and my father, there are no words to express how grateful I am to you for giving me the opportunity to live and study in other cities, without asking for anything in return, and showing me only love. Special thanks go to my twin brother Riccardo, you have been my example to follow during these years, more than you know.

Another piece of my gratitude goes to my colleagues, who walked with me in the past two years, being my new family. To Lorenzo, the guy who shared a lot of laughter and thoughts with me: "«respect»". To Martino, one of the smartest and most passionate people of astrophysics I have ever met. To Cecilia, that worked with me every single day being a real emotive support.

Finally, I have to thank my best friends, who have always cheered for me even if distances tried to split us. To Marco, Lorenzo, Alessandro and Francesco, you are the friends that everyone needs, I could not ask for best supporters. I grow up with you sharing the best memories and I hope to have you around me forever.

Table of Contents

Abstract **I**

Sommario **II**

Acknowledgements **III**

Symbols and Acronyms **VI**

List of Figures **VIII**

List of Tables **XII**

1 Introduction **1**
1.1 State of the art . . . 2
1.2 Aim of the thesis . . . 6
1.3 Thesis outline . . . 7

2 The Keplerian map **9**
2.1 The Framework . . . 9
2.1.1 Three-Body Problem . . . 9
2.1.2 Variation of Parameters . . . 13
2.2 Mathematical Model of the Keplerian Map . . . 18
2.2.1 Semi-analytical approach . . . 27
2.2.2 Numerical Approach . . . 28
2.2.3 The Kick Map . . . 29

3 Limits of the Keplerian map theory **32**
3.1 Jacobi Constant dependence . . . 33
3.1.1 Synodic reference frame and Libration points . . . 34
3.1.2 Jacobi Constant - Mass parameter - Error Map . . . 37
3.1.3 Influence of the energy with respect to the third body . . . 45
3.2 Minimum Relative Distance dependence . . . 46
3.3 Results and considerations . . . 49

3.3.1 Comparison with Patched Conics approach 50
3.3.2 Error threshold as criterion for the Keplerian map applicability 51
3.3.3 Minimum Relative Distance prediction 54
3.3.4 Other error maps 56

4 Model validation **57**
4.1 Earth - Moon system 58
4.1.1 Trajectory with high energy 58
4.1.2 Trajectory with low energy 61
4.2 Jupiter - Europa system 63

5 Lagrange's Planetary Equations in hyperbolic form **69**
5.1 Hyperbolic LPEs Mathematical Model 69
5.2 Application procedure and remarks 73

6 Distant retrograde orbits design with the Keplerian map **77**
6.1 Quasi-Satellite Orbits definition 78
6.2 Modeling Martian environment 80
6.3 New disturbing function and Keplerian Map applicability 82
6.4 Optimisation Process 84
6.5 Analysis of the results 87
6.5.1 Phobos QSO 87
6.5.2 Deimos QSO 93
6.6 CPU time comparison 97

7 Conclusions and Further Developments **99**

References **101**

Symbols & Acronyms

The following list of symbols is compiled in alphabetical order.

a	Semi-major axis [km]
e	Eccentricity [-]
C_J	Jacobi constant [-]
E	Eccentric anomaly [rad]
$\mathcal{E}$	Orbital energy [km^2/s^2]
h	Altitude [km]
$\mathcal{H}$	Hamiltonian [km^2/s^2]
i	Inclination [rad]
$\mathcal{J}$	Cost function [-]
$\mathcal{K}$	Keplerian energy term [km^2/s^2]
L	Libration point, Length
m	Mass [kg]
M	Mean anomaly [rad]
n	Mean motion [rad/s]
p	Generalized momentum [km^2/s^2]
r	Distance [km]
R	Distance, Disturbing function, Rotation matrix
s	State
t	Time [s]
T	Period [s]
U	Potential function [kg km^2/s^2]
v	Velocity [km/s]
x, X	Coordinate
y, Y	Coordinate
z, Z	Angle, Coordinate
α	Generic orbital element, Angle
γ	Phasing angle [rad]
δ	Angle, Coefficient
ε	Error
θ	Angle, True anomaly [rad]
λ	Longitude [rad]
μ	Mass Parameter [-]
ν	True anomaly [rad]
π	Number
ρ	Cost function coefficient [-]
ϕ	Latitude [rad]
Ω	Right Ascension of the Ascending Node [rad]
ω	Argument of pericentre [rad]

The following list of acronyms is compiled in alphabetical order.

$CR3BP$	Circular Restricted Three Body Problem	NEA	Near-Earth Asteroid
DRO	Distant Retrograde Orbit	ODE	Ordinary Differential Equation
GVE	Gauss' Variational Equations	QSO	Quasi-Satellite Orbit
ECI	Earth Centered Inertial	$R2BP$	Restricted Two Body Problem
FOV	Field Of View	$R3BP$	Restricted Three Body Problem
LPE	Lagrange's Planetary Equations	$RAAN$	Right Ascension of the Ascending Node
$LVLH$	Local-Vertical Local-Horizontal	S/C	Spacecraft
$MOID$	Minimum Orbit Intersection Distance	SOI	Sphere Of Influence
MRD	Minimum Relative Distance	SRP	Solar Radiation Pressure
		$JUICE$	JUpiter ICy moons Explorer

List of Figures

1 Inertial barycentric reference frame $\{G, X, Y, Z\}$. 10
2 Non-inertial (rotating) Synodic reference frame. Axis z exiting from the paper, coinciding with axis Z of the inertial reference frame in Fig. 1. 11
3 Libration points representation. The three collinear points are L_1, L_2 and L_3, while the triangular points are L_4 and L_5. 13
4 Planet-centered reference frame $\{\xi, \eta, \zeta\}$ used in the perturbation approach. Axis ζ exiting from the paper. 15
5 Barycentric reference frame $\{G, x', y', z'\}$ used in the Keplerian Map theory. 19
6 Perturbed reference frame $\{G, x', y', z'\}$ and unperturbed reference frame $\{m_1, x'', y'', z''\}$. Axes z' and z'' exiting from the paper. 21
7 Spherical triangle used to obtain the expression of the phasing angle γ_{CR3BP}. 30
8 Spherical triangles used to obtain the expression of the phasing angle γ in the R3BP context. 31
9 Zero velocity curves for five values of the Jacobi constant C_J (one in each of the cases), computed for a test case with $\mu = 0.3$. Particle's position denoted with P, gray regions are forbidden and white regions are allowed. In the last subfigure on the right it is represented how the value of C_{L_i} changes with the value of μ [3]. 35
10 Blocks scheme summarizing the procedure to obtain the $C_J - \mu - \varepsilon_{\Delta a}$ Map and the $MRD - \mu - \varepsilon_{\Delta a}$ Map. 37
11 $C_J - \mu - \varepsilon_{\Delta a}$ Map. Red regions identify errors in the numerical integration of the Lagrange's Planetary Equations. Color-map showing the relative percentage error defined in Eq. (70). 40
12 Error Map in Jacobi Constant dependence with the addition of two different features: C_{L_i} lines or 3^{rd} body SOI transitions (identified with red crosses). 42
13 $C_J - \mu - \varepsilon_{\Delta a}$ Map with region in which the error increases highlighted through a pink curve. 44

14 Two test trajectories belonging to the pink curve in Fig. 13. The plot contains the paths of the particle according to the CR3BP and the Keplerian Map numerical propagation, and even the trajectory traveled by the third body during the time span. . . 44
15 $C_J - \mu - \bar{\mathcal{E}}_2$ Map. Color-map representing the energy of the particle with respect to the third body, normalised to the energy of the third body with respect to the primary. 46
16 $MRD - \mu - \varepsilon_{\Delta a}$ Map. Y axis is containing the Minimum Relative Distance (MRD) reached by the particle with respect to the third body, normalised to its sphere of influence (Eq. (71)). Color-map representing the relative percentage error defined in Eq. (70) between CR3BP and Keplerian Map propagation. 47
17 3D surface and level curves of the $MRD - \mu - \varepsilon_{\Delta a}$ Map represented in Fig. 16. Pink lines highlighting the behavior of the error with the increasing of the MRD. Now the MRD is not normalised to obtain a better visibility of the feature. 49
18 $C_J - \mu - \varepsilon_{\Delta a}$ Map comparing CR3BP and Patched Conics approach. Color-map showing the error defined in Eq. (75). Set of initial conditions of Table 1 and Table 2. 51
19 $MRD - \mu - \varepsilon_{\Delta a}$ Map comparing CR3BP and Patched Conics approach. Color-map showing the error defined in Eq. (75). Set of initial conditions of Table 1 and Table 2. MRD normalised to the third body sphere of influence radius (Eq. (71)). 52
20 Binary $C_J - \mu - \varepsilon_{\Delta a}$ Map. Color-map showing acceptable and non-acceptable cases according to the error limit of Eq. (76). Same building procedure of the map in Fig. 11. 53
21 Binary $MRD - \mu - \varepsilon_{\Delta a}$ Map. Color-map showing acceptable and non-acceptable cases according to the error limit of Eq. (76). Same building procedure of the map in Fig. 16. 53
22 Trajectory of the particle with initial conditions in Table 4, propagated with CR3BP and Keplerian Map, represented in the Inertial Barycentric and Synodic reference frames. 61
23 Orbital elements evolution(referred to the case of Section 4.1.1). Comparison of numerical propagation through CR3BP and Keplerian Map. 62

24 Trajectory of the particle with initial conditions in Table 7, propagated with CR3BP and Keplerian Map, represented in the Inertial Barycentric and Synodic reference frames. 64
25 Orbital elements evolution (referred to the case of Section 4.1.2). Comparison of numerical propagation through CR3BP and Keplerian Map. 65
26 Trajectory of the particle in Inertial Barycentric reference frame of Jupiter-Europa system (initial conditions in Table 9). Comparison between numerical propagation through CR3BP or Keplerian Map (the prediction almost exact). 67
27 Orbital elements evolution (referred to the Jupiter-Europa example). Comparison of numerical propagation through CR3BP and Keplerian Map (the prediction is almost exact). 68
28 Rotating barycentric reference frame ($\{G, x', y', z'\}$) and planet-centered reference frame ($\{m_2, x'', y'', z''\}$) used to derive the disturbing function R. Axes z' and z'' exiting from the paper. . . . 72
29 $C_J - \mu - \varepsilon_{\Delta a}$ Map obtained with the Keplerian Map + Hyperbolic LPEs when the particle flies inside the SOI of the third body. . 75
30 $MRD - \mu - \varepsilon_{\Delta a}$ Map obtained with the Keplerian Map + Hyperbolic LPEs when the particle flies inside the SOI of the third body. 76
31 Three main reference frames used in the design of the QSO. The Phobos/Deimos Equatorial frame contains even the right ascension and declination. 81
32 Main perturbations acting in Martian environment [36] with corresponding orders of magnitude as function of the distance from the surface. 82
33 QSO around Phobos represented in Mars IAU frame. Trajectory propagated for one day (to obtain a better visibility). 88
34 Ground track of the QSO around Phobos, with initial and final points. 88
35 QSO around Phobos in LVLH frame seen from two different point of views. 89
36 Orbital elements evolution with time for Phobos QSO. 91
37 Relative percentage error (defined in Eq. (116)) between numerical integration of R3BP equations and LPE evolution with time for each orbital element, referred to Phobos QSO. 92

38 QSO around Deimos represented in Mars IAU frame. Trajectory propagated for two days (to obtain a better visibility). 94
39 Ground track of the QSO around Deimos, with initial and final points. 94
40 QSO around Deimos in LVLH frame seen from two different point of views. 95
41 Orbital elements evolution with time for Deimos QSO. 96
42 Relative percentage error (defined in Eq. (116)) between numerical integration of R3BP equations and LPE evolution with time for each orbital element, referred to Deimos QSO. 97

List of Tables

1 Block particle initial conditions used to build the $C_J - \mu - \varepsilon_{\Delta a}$ Map and the $MRD - \mu - \varepsilon_{\Delta a}$. 38
2 Initial conditions of the third body used to build the $C_J - \mu - \varepsilon_{\Delta a}$ Map and the $MRD - \mu - \varepsilon_{\Delta a}$. 39
3 Mass parameters μ for most common systems studied in the Three-Body Problem field [27]. 41
4 Initial conditions of the particle in the Earth - Moon system (trajectory with $C_J < C_{L_1}$). 59
5 Initial conditions of the Moon used in the Earth - Moon system examples. Orbital elements of 30/10/2021 from NASA Horizons [28] but CR3BP case ($e_0 = 0$). 59
6 Jacobi Constant values in the Libration points of the Earth - Moon system in the dimensionless Synodic reference frame. . . . 60
7 Initial conditions of the particle in the Earth - Moon system (trajectory with $C_J > C_{L_1}$). 63
8 Initial conditions of Europa used in the Jupiter - Europa system example. Orbital elements of 30/10/2021 from NASA Horizons [28] but CR3BP case ($e_0 = 0$). 64
9 Initial conditions of the particle in the Jupiter-Europa system. . 66
10 Planetary constants of Mars, Phobos and Deimos [27]. 80
11 Initial states in Phobos LVLH frame and features of the corresponding QSO if the motion is propagated for 30 days. Initial epoch: 21^{th} December, 2021 $13:30\ UTC$ 87
12 Initial states in Deimos LVLH frame and features of the corresponding QSO if the motion is propagated for 30 days. Initial epoch: 21^{th} December, 2021 $13:30\ UTC$ 93
13 Computational time comparison required for the optimisation process aimed in finding the initial conditions of Phobos and Deimos QSO. Processor: $1.8GHz$ Intel Core i7 98

CHAPTER 1

Introduction

SINCE the beginning of the space age, there is the needing to predict the motion of a satellite in order to design trajectories such that the mission objectives are satisfied. The modeling of the system in which the spacecraft is involved have always been a real challenge for scientists, that developed mathematical models to reconstruct the dynamics of a probe orbiting around a planet.

The two-body problem [1] is the most intuitive and simple model used in celestial mechanics, being a sufficiently faithful representation of the motion that a particle follows around a major celestial body. However, it is an approximation in which the effect of perturbing bodies that simultaneously influence the motion of a mass-less particle is neglected. This assumption leads to wrong results when such motion is predicted for a long period, especially in environments in which the perturbing bodies are massive and/or numerous (as in the Jovian system). For this reason, it is necessary to use a multi-body problem to reconstruct the behavior of any space system for practical applications [2].

More accurate predictions can be obtained with the use of the three-body problem [3], in which it is accounted the presence of a third body that influences the motion of the spacecraft. Such expansion is used when modeling any gravity assist maneuver: a close encounter phenomenon widely used nowadays in space mission design. It is a technique that allows to save propellant mass, taking advantage of a natural energy exchange between the celestial body and the spacecraft.

In several cases the third body acts only as a perturbation for the particle, whose dynamics remains in majority dictated by the gravity field of the primary celestial body. This is what happens when the third body is far from the spacecraft, and its gravity is so small with respect to the one of the primary. In these contexts it is possible to simplify the problem, accounting only for long-period effects of the third body, adopting the orbital perturbations technique [4].

In between the three-body problem and the perturbation technique, the Keplerian Map theory was developed [5]. It is an approach which is born to predict the behavior of a particle in distant encounters with a secondary attractor. Being a semi-analytical model, it allows to save the computational time required for the numerical integration of the three-body problem equations (which have not a close form solution). However, it is a theory that sometimes leads to completely wrong predictions, as will be introduced in this chapter and then explained in the following.
This study has been performed with the final target of developing a propagator able to predict the motion of a particle considering the effect of the presence of a third body, approximating the solution of the three-body problem. This can be done using different models (e.g Keplerian Map, perturbations technique, patched conics, etc...), each one applied when leading to results with higher accuracy.
In this introductory section it is explained the state of the art in this field, then the objectives of the thesis are meticulously listed, and finally it is presented the thesis outline.

1.1 State of the art

As anticipated above, the simplest way to represent the motion of a spacecraft orbiting around a celestial body is to model the system with the two-body problem. By assuming that the mass of the spacecraft is small, it does not affect the motion of the planet. This physical model is called Restricted Two Body Problem (R2BP) [1]. It is the fastest and most intuitive model that can be adopted, especially when searching for very preliminary solutions.
The mathematical model of the two-body problem is directly obtained by Newton's 2^{nd} law [1]. It has an analytical closed-form solution, such that the trajectory of the particle follows different conics sections depending on its orbital energy, allowing for an easy dynamical interpretation which can be exploited for space missions design.
However, in most of the cases the orbital perturbations play a significant role which shall be taken into account if a more refined solution is needed.
The path followed by a mass-less particle can be represented in a particular set of coordinates, called Keplerian elements (since they uniquely represent an orbit respecting Kepler's laws). Except for the true anomaly of the particle, it is asserted that in the two-body problem these coordinates remain constant

with time [1]. An extension of the R2BP used to design interplanetary trajectories is the patched-conics model, in which the trajectory of the particle is divided in different arcs, each one modelled with the two-body problem. The gravitational attraction exerted by a celestial body on the particle is considered only inside the body Sphere Of Influence (SOI) [1], whose size depend on the body mass. For instance, this approach could be applied to predict the path of a spacecraft going away from the Earth and approaching the interplanetary space. After the particle goes outside the SOI of the Earth, only the gravitational attraction of the Sun is considered.
Even if the patched-conics approach allows to design an interplanetary mission in a short time, the solution can be used only as a preliminary one. Indeed, because of the assumptions made, the error introduced is significantly large in multiple cases (as when the oblateness of a celestial body provokes a non-uniform gravity field, or when there is a strong effect of the Solar Radiation Pressure, or when there is an atmosphere, ...). The most relevant case for this discussion The most relevant for this discussion is when the gravitational force exerted by two or more bodies is of the same order of magnitude, meaning that none of them can be assumed negligible.
In order to obtain a solution that is more faithful to the exact one, it is necessary to account for the effect of the orbital perturbations that alter the motion of the particle, causing its orbital elements to vary over time. This theory is also called Variation of Parameters [4], and it makes use of dynamics equations that includes the effects of the orbital disturbances. If only conservative forces are acting on the particle, the disturbing force can be described as gradient of a potential function and its effect obtained through the Lagrange's Planetary Equations (LPE) [6]; if non-conservative forces are modelled (as the Aerodynamic drag) the Gauss' Variational Equations (GVE) [4] shall be used. These set of equations allows to obtain the variation of the orbital elements of the particle through numerical integration.
Whenever the study is focused only in the long-period dynamics of the particle, different applications of the perturbation approach have been developed. A relevant one is the use of a single or double-averaging technique following the approach of Kaufman and Dasenbrock [7], which is a semi-analytical approach that allows to isolate long-period effects of the third-body disturbance. Applications of this method can be the re-entry prediction of a satellite through the use of a disposal maneuver, exploiting for instance the Planetary Orbital Dynamics [8].

Since the studies carried out in this thesis are centered on the effect of the third body on the motion of the particle, the Variation of Parameters will be used considering the third-body disturbance only. Then, in Section 6, even other perturbations will be added to the mathematical model. Works accounting for the luni-solar disturbances and zonal harmonics, focused in Highly-Elliptical Orbits (HEO) have been carried out exploiting a double-averaging technique [9]. A similar procedure to develop the disturbing function is exploited in the current studies.
When the third body effect cannot be considered as a perturbation, but it strongly influences the particle dynamics, it is necessary to adopt a different model, moving to the three-body problem dynamical regime. For sake of clarity, it is useful to specify that in this thesis the "third body" and the "secondary attractor" have the same meaning, being two notations used in literature for different topics (but now are considered as the same thing).
The Circular Restricted Three-Body Problem (CR3BP) [3] is a widely used model when working in the three-body context, since it is a good compromise between accuracy of the solution and complexity of the mathematical model.
In the CR3BP the states of the particle are expressed in a rotating frame called Synodic Frame, centered in the barycentre of the system. Under the assumptions of the CR3BP 5 equilibrium points of the system can be found [3]. These points are widely exploited in space missions, since they allow to design trajectories in which the spacecraft keeps the same position relative to the Sun and the Earth with almost null fuel consumption for station keeping. Their stability properties are also exploited in mission design for low-cost transfers.
An extension of the CR3BP is considered when dealing with non-circular orbits of the attractive bodies around their centre of mass, entering in the more general field of the Restricted Three-Body Problem (R3BP) [3]. This model does not benefit from the same features present in the CR3BP, but it can be used when an high-accuracy solution is needed.
In between of the Variation of Parameters and the Three-body problem, there is the Keplerian Map theory. Such theory makes use of the third-body potential in the perturbation approach, to approximate the solution of the three-body problem [10].
It was initially developed by Petrosky and Broucke [11],[12]; then it was adopted to model the effect of successive distant encounters with the third body by Ross and Scheeres [5], who developed a kick energy function able to predict the evolution of the orbital elements after each distant passage. Afterwards, the model

was refined by the works of Alessi et al. [13], [14], [15] and Sanchez et al. [16], where the accuracy of the method was compared to the solution of the CR3BP. The actual state of the art of the Keplerian Map has been reached with the work by Giudici [17] which extended the method for the general case of the R3BP, obtaining the model without assumptions on the mass parameter of the system. In its work the theory is validated with the reproduction of some steps of JUICE mission (JUpiter ICy moons Explorer) [18], and then exploited to design a mission towards a Near Earth Asteroid (NEA).
Another model which has been developed to describe the motion of the particle in close encounters with the third body is the Öpik's flyby theory, explained by Valsecchi et al. [19],[20],[21]. The method introduces further simplifications on the CR3BP to easily predict the dynamics when the spacecraft is passing near the secondary attractor.
Despite of the analysis done on the accuracy of the Keplerian Map theory, a clear limit of applicability of the method has not been found yet. In recent studies [16] a comparison of the method with the Double averaging technique and Öpik's flyby theory has been done, declaring that:

- The third body perturbative approach (single or double averaging) can be more efficiently used (with respect to the Keplerian Map) whenever the particle remains very far from the perturbative body
- In some cases the Keplerian map can also be used for encounters occurring within the Sphere Of Influence, as long as the perturbation does not change drastically the original Keplerian motion

These two statements can be used as starting points for the present work. The first one suggests that it is pointless to use the Keplerian Map theory when the third body is several sphere of influence radii far from the spacecraft. The limit at which the use of the double averaging approach becomes advantageous has still to be defined.
The second statement is proposing to quantify the effect of a close encounter and exploit it as a limit for the applicability of the Keplerian Map theory. If the flyby with the third body follows a strong variation of the particle motion, another method shall be used to predict the trajectory instead of the Keplerian Map. This happens in general when the secondary attractor has an high planetary constant, since the gravity field exerted on the particle is of the same order of magnitude of the main attractor. However, a single parameter may

not be sufficient to fully characterize the effect of a close encounter, and further studies are needed in this direction.

1.2 Aim of the thesis

As aforementioned in the first part of the chapter, a series of studies has been done searching for suitable methods that allow to approximate the solution of the three-body problem. The purpose of such studies is to develop a propagator capable of approximating the motion of the spacecraft, exploiting different methods and combining them. Since each single method (e.g. Öpik's flyby theory [19]) works well only in certain circumstances, by merging together different approaches it is possible to propagate the motion in every situation. It is necessary to identify the limits of each method such that an accurate switch can be done. The idea is that this switching procedure is done automatically by the final propagator, hence it must be able to identify when it is better to use a certain method instead of another one through a sharp borders definition. Such software can be used in missions design not only to predict the trajectory, but also to plan the effect of successive encounters independently of the distance from the disturbing body. It shall work even in systems in which there are multiple perturbing bodies at the same time (as in the Jovian system).
Among the different methods analysed as candidates for being part of the propagator, a particular and intense study is performed on the Keplerian Map theory. This method constitutes the core of the propagation, acting as a "bridge" between models considering the third body as a perturbation and models considering the third body for flybys (in which it becomes the primary attractor within its sphere of influence).
The main thesis objective is to define an applicability domain of the Keplerian Map approach. The identification of such region is done selecting a wide range of particle initial conditions, which are then numerically propagated with the Keplerian Map and the results are compared with the solution of the three-body problem. Through this analysis it is possible to know a priori when is better to use the Keplerian Map instead of another model as the double averaging technique or the flyby theory.
The second aim of this work is to apply the method to design distant retrograde orbits, as will be presented in Section 6. Such family of orbits are usually found with a numerical analysis in the three-body problem, through the integration of the R3BP equation [22]. The initial conditions of the probe

are obtained with an optimisation algorithm, such that the stability period of the orbit is imposed. This is a completely novel application of the Keplerian Map theory that has been never done in past works. The numerical integration of the Keplerian Map allows to save computational time with respect to the integration of the R3BP equations, especially when the search domain of the optimisation process is wide. The results obtained (that will be shown in the dedicated chapter) confirmed that it is particularly advantageous to use the Keplerian Map in such context.

1.3 Thesis outline

The different chapters of this thesis are organised sequentially as follow:

- **Chapter 2:** The Keplerian Map – This chapter starts with the explanation of the framework in which the Keplerian Map is defined. The three-body problem and its properties are introduced, as well as the perturbation technique. After that, the Keplerian Map theory is explained through the demonstration of its mathematical model, showing how it can be applied to predict the motion of the particle.

- **Chapter 3:** Limits of the Keplerian Map theory – In this chapter it is presented the analysis on the boundaries of applications of the Keplerian Map. This part constitutes the core of the thesis. A completely novel analysis on the Jacobi Constant dependence is included, adding in parallel an analysis on the energy of the particle with respect to the third body during the close encounters. Then, the error dependence on the Minimum Relative Distance between the particle and the third-body is studied, concluding the chapter with remarks on the limits of the Patched Conics approach and the explanation of how the minimum distance reached by the particle can be analytically predicted.

- **Chapter 4:** Model Validation – This chapter includes practical examples to show the validity of the results obtained in Chapter 3. Three test cases are analysed: the first two consider the Earth-Moon system (in which the Keplerian Map shows significant errors in the propagation) and the last one the Jupiter-Europa system. The latter represents the scenario in which it is possible to use the theory in order to obtain almost exact results in the propagation.

- **Chapter 5:** Alternative model – In this chapter it is explained a possible alternative model that can be used instead of the Keplerian Map to numerically propagate the motion of the particle. The approach under consideration adopts the Lagrange's Planetary Equations in their hyperbolic form, and it is applied when the particle enters in the sphere of influence of the third body. However, as explained in this part, no improvements are observed and a deeper analysis on this alternative is needed.

- **Chapter 6:** Keplerian Map for trajectory design – The theory of the Keplerian Map is used to design particular trajectories in Martian environment, called Distant Retrograde Orbits or Quasi-Satellite Orbits. In order to find the initial conditions of the mass-less particle, an optimisation algorithm is adopted. Through the use of the Keplerian Map theory, the optimisation process appears to be less expensive in terms of computational time with respect to the procedure that exploit the three-body problem equations. An additional orbital perturbation is here considered, and also the elliptical motion of Martian moons Phobos and Deimos are involved in the mathematical model. The output is a trajectory that can be exploited in future space missions aimed at performing remote sensing above Phobos and Deimos surfaces. The process to generate such orbits is carefully explained in the first part, and then the effectiveness of the Keplerian Map theory is highlighted.

- **Chapter 7:** Conclusions – The final part of the thesis starts with a brief resume of the work presented in the previous chapters. Then, the possible continuations in this field are proposed through suggestions on the directions that could be taken.

CHAPTER 2

The Keplerian map

In this chapter the Keplerian Map will be explained. As anticipated in Section 1.1, this model has been developed to approximate the three-body problem solution making use of the third-body potential through the Lagrange's Planetary Equations.
The first part of this section contains a brief introduction on the framework of the three-body problem and the perturbation approach. Afterwards, the mathematical model of the Keplerian Map is derived step by step. Thanks to the work done in past years [17], such derivation is carried out without making assumptions on the mass parameter of the system. However, as will be understood going through the definition of the model, this does not imply that the approach can be adopted to predict the motion of the particle in all the scenarios. Through an analysis of the error introduced, varying numerous parameters in the initial conditions of the particle, a domain of applicability of the Keplerian Map theory will be defined in the next chapter.

2.1 The Framework

In order to introduce the Keplerian Map theory, it is necessary to introduce the possible models that can be used for representing the third body disturbance, highlighting the assumptions that each method requires and therefore the possible domains of application.

2.1.1 Three-Body Problem

Consider a system composed by three bodies as represented in Fig. 1. Each mass is exerting a gravitational force on the others. The masses m_1 and m_2 represent the primary and the secondary attractors (e.g. m_1 represents the Earth, m_2 represents the Moon), while m_3 identifies the spacecraft (or a general minor body) orbiting around them. Since the spacecraft with mass m_3

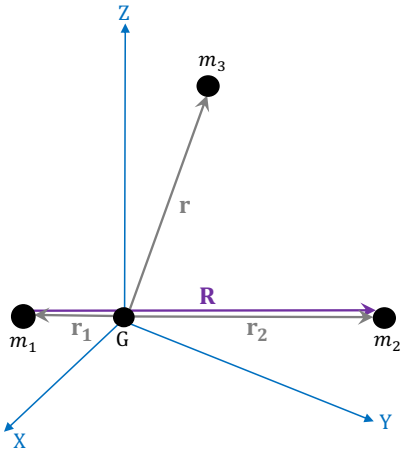

Figure 1: Inertial barycentric reference frame $\{G, X, Y, Z\}$.

has a negligible mass with respect to the values of m_1 and m_2, it can be modelled as a mass-less particle, following that it does not influence the motion of the two massive bodies. This is the assumption characterising the Restricted Three-Body Problem (R3BP).
The inertial reference frame $\{X, Y, Z\}$ is centered in the barycentre of the system (along the conjunction between m_1 and m_2). The mass parameter of the system is defined as:

$$\mu = \frac{m_2}{m_1 + m_2} \tag{1}$$

The position vector of the mass-less particle with respect to the barycentre of the system is identified with $\mathbf{r}$, while the position vectors of m_1 and m_2 from the barycentre are identified with $\mathbf{r_1}$ and $\mathbf{r_2}$, respectively. The position vector of m_2 with respect to m_1 is denominated with $\mathbf{R}$ (that has the same direction of $\mathbf{r_2}$, but different modulus).
From the barycentre definition, it is possible to obtain that:

$$\begin{cases} \mathbf{r_1} = -\mu\mathbf{R} \\ \mathbf{r_2} = (1-\mu)\mathbf{R} \end{cases} \tag{2}$$

The equation of motion in the inertial barycentric reference frame of the mass-less particle can be obtained by writing the 2^{nd} Newton's law [1]:

$$\ddot{\mathbf{r}} = -\frac{Gm_1}{\|\mathbf{r} - \mathbf{r_1}\|^3}(\mathbf{r} - \mathbf{r_1}) - \frac{Gm_2}{\|\mathbf{r} - \mathbf{r_2}\|^3}(\mathbf{r} - \mathbf{r_2}) \tag{3}$$

By defining $\mu_1 = Gm_1$ and $\mu_2 = Gm_2$, and inserting Eq. (2) in Eq. (3), the equation of motion of the mass-less particle becomes:

$$\ddot{\mathbf{r}} = -\frac{\mu_1}{\|\mathbf{r} + \mu\mathbf{R}\|^3}(\mathbf{r} + \mu\mathbf{R}) - \frac{\mu_2}{\|\mathbf{r} - (1-\mu)\mathbf{R}\|^3}(\mathbf{r} - (1-\mu)\mathbf{R}) \tag{4}$$

Note that it is more convenient to write the equations of motion of the particle in function of quantities that can be easily understood. This is why the equations are written in function of $\mathbf{R}$, which can be obtained even from analytical ephemerides.
Eq. (4) can be numerically integrated to obtain the states of the mass-less particle over time. However, the mathematical model of the R3BP does not have interesting properties that can be exploited to understand better the behavior of the system.
Introducing the assumption that the primary and secondary bodies move on circular orbits around their barycentre, the model reduces to the Circular Restricted Three-Body Problem (CR3BP).
It is better to work in a rotating (non-inertial) reference frame as shown in Fig. 2, called Synodic reference frame.

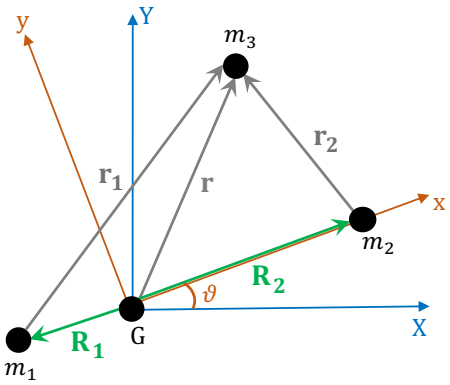

Figure 2: Non-inertial (rotating) Synodic reference frame. Axis z exiting from the paper, coinciding with axis Z of the inertial reference frame in Fig. 1.

In this reference frame $\{x, y, z\}$, the x axis is always directed from the primary to the secondary, the y axis lies on the orbital plane, while z is perpendicular to it. The frame is rotating around the barycentre of the system (which is the origin) about the z axis with constant angular velocity; as a result, m_1 and m_2 appear to be at rest.
It is useful to switch in non-dimensional coordinates [1] , assuming that:

- The sum of the primary and secondary bodies are such that $m_1 + m_2 = 1$;
- The mass value of the primary is $m_1 = 1-\mu$, and the one of the secondary is $m_2 = \mu$;
- The distance between m_1 and m_2 is equal to 1;
- The angular velocity of the frame is $\Omega = 1$, which means that a full period is equal to 2π.

Therefore, the equations of motion of the particle in this frame can be written as [1]:

$$\begin{cases} \ddot{x} - 2\dot{y} = x - \dfrac{1-\mu}{r_1^3}(x+\mu) - \dfrac{\mu}{r_2^3}(x-1+\mu) \\ \ddot{y} + 2\dot{x} = y - \dfrac{1-\mu}{r_1^3}y - \dfrac{\mu}{r_2^3}y \\ \ddot{z} = -\dfrac{1-\mu}{r_1^3}z - \dfrac{\mu}{r_2^3}z \end{cases} \tag{5}$$

where:

$$\begin{cases} r_1 = \sqrt{(x+\mu)^2 + y^2 + z^2} \\ r_2 = \sqrt{(x-1+\mu)^2 + y^2 + z^2} \end{cases} \tag{6}$$

The right-hand side in Eq. (5) is the gradient of a scalar function called Three-Body Potential U, that is defined as [1]:

$$U = \frac{1}{2}\left(x^2 + y^2\right) + \frac{1-\mu}{r_1} + \frac{\mu}{r_2} \tag{7}$$

Moreover, in the CR3BP there exists an integral of motion called Jacobi constant C_J defined as:

$$C_J = 2U - v^2 \tag{8}$$

where v is the particle velocity in the Synodic reference frame. The Jacobi constant can be considered as the total energy of the particle in the rotating frame. The existence of an integral of motion is one of the advantages of working in such frame. It can be exploited to understand the realms in which the particle with a certain energy can moves: when the velocity of the particle v is equal to zero, for a given value of C_J, there is a boundary in which m_3 can move, respecting the relation $2U > C_J$. These boundaries are called Zero

Velocity curves and they define the forbidden and allowed regions for the particle's motion.
When the value of ∇U is equal to zero, the particle is in equilibrium in the Synodic frame. There exist 5 equilibrium points, called Libration points, in which theoretically the particle remains in a fixed position relative to the massive bodies. These points can be exploited in mission design also exploiting their stability/instability features. The position of these points is represented in Fig. 3.

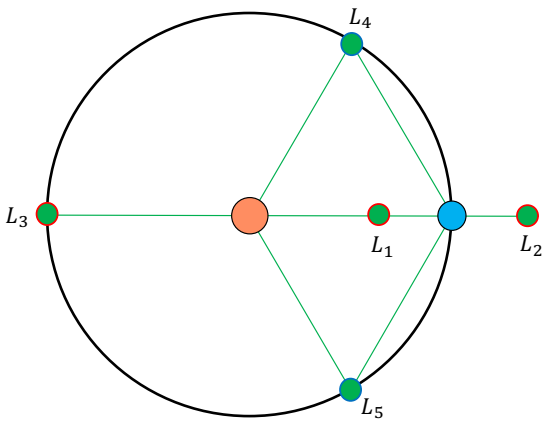

Figure 3: Libration points representation. The three collinear points are L_1, L_2 and L_3, while the triangular points are L_4 and L_5.

2.1.2 Variation of Parameters

The Variation of Parameters [4] is a formulation of the equations of motion for a particle orbiting into a perturbed dynamical system. In this theory the variation of the orbital elements of the particle are obtained integrating a set of differential equations. In the case in which only conservative perturbations are considered (which is the case of interest in this work), they can be written as gradient of a disturbing function R and inserted into the Lagrange's Planetary Equations (LPE) [6]. The LPE can assume different forms depending on the angular variable chosen to represent the motion; commonly, the angular variable considered is the initial mean anomaly M_0 of the particle [6]:

$$\begin{cases} \dfrac{da}{dt} = \dfrac{2}{na}\dfrac{\partial R}{\partial M_0} \\ \dfrac{de}{dt} = -\dfrac{\sqrt{1-e^2}}{na^2 e}\dfrac{\partial R}{\partial \omega} + \dfrac{1-e^2}{na^2 e}\dfrac{\partial R}{\partial M_0} \\ \dfrac{di}{dt} = -\dfrac{1}{na^2\sqrt{1-e^2}\sin i}\dfrac{\partial R}{\partial \Omega} + \dfrac{\cos i}{na^2\sqrt{1-e^2}\sin i}\dfrac{\partial R}{\partial \omega} \\ \dfrac{d\Omega}{dt} = \dfrac{1}{na^2\sqrt{1-e^2}\sin i}\dfrac{\partial R}{\partial i} \\ \dfrac{d\omega}{dt} = -\dfrac{\cos i}{na^2\sqrt{1-e^2}\sin i}\dfrac{\partial R}{\partial i} + \dfrac{\sqrt{1-e^2}}{na^2 e}\dfrac{\partial R}{\partial e} \\ \dfrac{dM_0}{dt} = -\dfrac{2}{na}\dfrac{\partial R}{\partial a} - \dfrac{1-e^2}{na^2 e}\dfrac{\partial R}{\partial e} \end{cases} \tag{9}$$

where $a, e, i, \Omega, \omega, M_0$ are the orbital elements of the particle, R is the disturbing potential and n is the particle mean motion.
In a semi-analytical perturbation approach, an averaged disturbing function can be taken to filter out high-frequency perturbations, isolating long-period terms. This is an elegant technique to analyze the effect of the perturbations, allowing a deeper understanding of the dynamics [9]. Following the approach developed by Kaufman [7], in a planet-centered reference frame (depicted in Fig. 4), the disturbing potential due to the third-body perturbation can be written as [9]:

$$R\left(r, r_{3B}\right) = \mu_{3B}\left(\frac{1}{\|\mathbf{r} - \mathbf{r_{3B}}\|} - \frac{\mathbf{r}\cdot\mathbf{r_{3B}}}{r_{3B}^3}\right) \tag{10}$$

where $\mathbf{r}$ is the position vector of the particle from the primary body, $\mathbf{r_{3B}}$ and μ_{3B} are the position vector of the third-body (i.e. the secondary attractor) with respect to the primary and its planetary constant.
By exploiting the angle ψ between the vectors $\mathbf{r}$ and $\mathbf{r_{3B}}$ (Fig. 4), the disturbing potential becomes [9]:

$$R\left(r, r_{3B}\right) = \frac{\mu_{3B}}{r_{3B}}\left(\frac{1}{\sqrt{1 - 2\left(r/r_{3B}\right)\cos\psi + \left(r/r_{3B}\right)^2}} - \frac{r}{r_{3B}\cos\psi}\right) \tag{11}$$

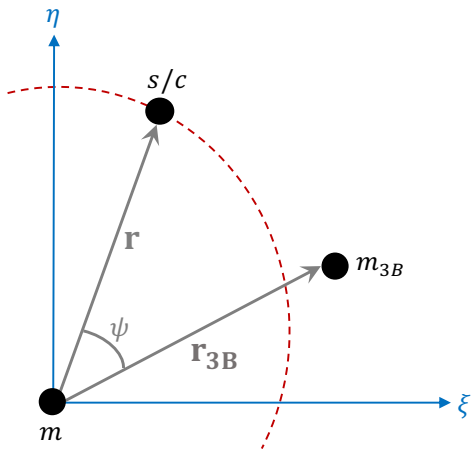

Figure 4: Planet-centered reference frame $\{\xi, \eta, \zeta\}$ used in the perturbation approach. Axis ζ exiting from the paper.

In order to substitute the disturbing potential inside the LPE, it is necessary to express it as function of the particle orbital elements $[a, e, i, \Omega, \omega, \nu]$.
According to Kaufmann and Dasenbrock procedure [7] (also explained in [9]), this can be achieved by using the eccentric anomaly E as angular variable (in alternative to the true anomaly ν), expressing the ratio between the orbit semi-major axis and the distance from the third body as:

$$\delta = \frac{a}{r_{3B}} \tag{12}$$

Then, the eccentricity direction $\hat{\mathbf{P}}$ and the semi-latus rectum direction $\hat{\mathbf{Q}}$ expressed in the inertial frame are obtained through a multiple rotation:

$$\begin{aligned} \hat{\mathbf{P}} &= R_3(\Omega) R_1(i) R_3(\omega) \begin{bmatrix} 1 \\ 0 \\ 0 \end{bmatrix} \\ \hat{\mathbf{Q}} &= R_3(\Omega) R_1(i) R_3\left(\omega + \tfrac{\pi}{2}\right) \begin{bmatrix} 1 \\ 0 \\ 0 \end{bmatrix} \end{aligned} \tag{13}$$

with $R_i(\alpha)$ (with $i = 1, 2, 3$) being the rotation matrix of angle α around the i^{th} axis.
The position vector of the particle can be written exploiting Eq. (13):

$$\mathbf{r} = \cos\nu \hat{\mathbf{P}} + \sin\nu \hat{\mathbf{Q}} \tag{14}$$

and the term $\cos\psi$ becomes:

$$\cos\psi = \hat{\mathbf{r}} \cdot \hat{\mathbf{r}}_{\mathbf{3B}} = \left(\hat{\mathbf{P}}\cos\nu + \hat{\mathbf{Q}}\sin\nu\right) \cdot \hat{\mathbf{r}}_{\mathbf{3B}} = A\cos\nu + B\sin\nu \tag{15}$$

with:

$$\begin{aligned} A &= \hat{\mathbf{P}} \cdot \hat{\mathbf{r}}_{\mathbf{3B}} \\ B &= \hat{\mathbf{Q}} \cdot \hat{\mathbf{r}}_{\mathbf{3B}} \end{aligned} \tag{16}$$

By applying Eq. (12) and Eq. (15) in Eq. (11), the disturbing function R is [9]:

$$\begin{aligned} R = &\frac{\mu_{3B}}{r_{3B}}\left(\frac{1}{\sqrt{1-2\delta\left(A\left(\cos E - e\right) + B\sqrt{1-e^2}\sin E\right) + \delta^2\left(1 - e\cos E\right)^2}}\right. \\ &\left. -\delta\left(A\left(\cos E - e\right) + B\sqrt{1-e^2}\sin E\right)\right) \end{aligned} \tag{17}$$

Assuming that the particle is far enough from the perturbing body, this follow that the parameter δ is small, and Eq. (17) can be rewritten as a McLaurin series around δ [7]:

$$R\left(r, r_{3B}\right) = \frac{\mu_{3B}}{r_{3B}} \sum_{k=2}^{\infty} \delta^k F_k\left(A, B, e, E\right) \tag{18}$$

where the summation starts from $k = 2$ since the zero-order term is constant (therefore irrelevant), and the first-order term simplifies with the second term of Eq. (17).
Now the first averaging operation is performed by integrating the function F_k over one particle orbital period [7], assuming that the orbital elements remain fixed during one revolution (valid assumption since δ is assumed to be small):

$$\bar{F}_k\left(A, B, e\right) = \frac{1}{2\pi}\int_{-\pi}^{\pi} F_k\left(A, B, e, E\right)\left(1 - e\cos E\right) dE \tag{19}$$

and the averaged disturbing function becomes [9]:

$$\bar{R}\left(r, r_{3B}\right) = \frac{\mu_{3B}}{r_{3B}} \sum_{k=2}^{\infty} \delta^k \bar{F}_k\left(A, B, e\right) \tag{20}$$

The next step is to compute the partial derivatives of the averaged disturbing function with respect to the orbital elements, in order to insert them into the LPE of Eq. (9) [9]:

$$\begin{aligned}
\frac{\partial \bar{R}}{\partial a} &= \frac{\mu_{3B}}{r_{3B}} \sum_{k=2}^{\infty} \frac{k}{a} \delta^k \bar{F}_k \\
\frac{\partial \bar{R}}{\partial e} &= \frac{\mu_{3B}}{r_{3B}} \sum_{k=2}^{\infty} \delta^k \frac{\partial \bar{F}_k}{\partial e} \\
\frac{\partial \bar{R}}{\partial i} &= \frac{\mu_{3B}}{r_{3B}} \sum_{k=2}^{\infty} \delta^k \left(\frac{\partial \bar{F}_k}{\partial A} \frac{\partial A}{\partial i} + \frac{\partial \bar{F}_k}{\partial B} \frac{\partial B}{\partial i} \right) \\
\frac{\partial \bar{R}}{\partial \Omega} &= \frac{\mu_{3B}}{r_{3B}} \sum_{k=2}^{\infty} \delta^k \left(\frac{\partial \bar{F}_k}{\partial A} \frac{\partial A}{\partial \Omega} + \frac{\partial \bar{F}_k}{\partial B} \frac{\partial B}{\partial \Omega} \right) \\
\frac{\partial \bar{R}}{\partial \omega} &= \frac{\mu_{3B}}{r_{3B}} \sum_{k=2}^{\infty} \delta^k \left(\frac{\partial \bar{F}_k}{\partial A} \frac{\partial A}{\partial \omega} + \frac{\partial \bar{F}_k}{\partial B} \frac{\partial B}{\partial \omega} \right)
\end{aligned} \tag{21}$$

A possible continuation can be a further averaging of the disturbing function, integrating over the fast variable of the perturbing body orbital motion. This can be done assuming that the orbital elements of the particle do not change significantly during a full revolution of the third body.
The double-averaged disturbing function R becomes [9]:

$$\bar{\bar{R}}_{3B}\left(r, r_{3B}\right) = \frac{\mu_{3B}}{r_{3B}} \sum_{k=2}^{\infty} \delta^k \bar{\bar{F}}_k \left(e, i, \Omega, \omega, i_{3B}\right) \tag{22}$$

where i_{3B} is the third-body inclination.
Note that the disturbing potential can be expressed in different frames, but the double-averaging procedure remains the same.
A first frame [23] is centered in the central body, the $x-y$ plane is the perturbing body orbital plane and the z direction is directed as the perturbing body angular momentum. This is the same rotating frame used in the CR3BP (the Synodic frame), with the only difference that it is not centered in the centre of mass of the system.
Another possible frame that can be used is a planet-centered inertial one [9] (if the central planet is the Earth, than it is the ECI frame). Making use of this frame, the Eq. (22) assumes a more complex form but it does not introduce the assumption that all the disturbing bodies lie on the same plane. This can lead to wrong results when the planes are not similar (as in the Jovian system,

or even when working with the luni-solar perturbation around the Earth) and it is facilitating the introduction of other perturbation effects in the potential as the zonal harmonics.
In the latter frame, the double-averaging is obtained integrating the single-averaged disturbing function over one period of the disturbing body [9]:

$$\bar{\bar{F}}_k\left(e, i, \Delta\Omega, \omega, i_{3B}\right) = \frac{1}{2\pi}\int_0^{2\pi} \bar{F}_k\left(A, B, e\right) d\theta_{3B} \tag{23}$$

where $\Delta\Omega = \Omega - \Omega_{3B}$ and θ_{3B} is the third-body true anomaly. Note that the dependency of $\bar{\bar{F}}_k$ by θ_{3B} is in the coefficients A and B, since [9]:

$$\begin{aligned} A &= A\left(i, \Omega, \omega, i_{3B}, \Omega_{3B}, \omega_{3B} + \theta_{3B}\right) \\ B &= B\left(i, \Omega, \omega, i_{3B}, \Omega_{3B}, \omega_{3B} + \theta_{3B}\right) \end{aligned} \tag{24}$$

Even in this case the temporal variation of the orbital elements can be obtained by computing the partial derivatives of Eq. (22) with respect to the particle orbital elements, and then inserted into the LPE in Eq. (9).

2.2 Mathematical Model of the Keplerian Map

The Keplerian Map theory is now presented starting from the derivation of its mathematical model in the CR3BP and expanding it in the general case of the R3BP. In this paragraph, the approach described by [17] is followed.
The starting point can be considered the expression of the Hamiltonian of the CR3BP in the inertial reference frame (referring to Fig. 1), which can be written as [5]:

$$\mathcal{H}_{in} = \frac{1}{2}\left(p_x^2 + p_y^2 + p_z^2\right) - \frac{1-\mu}{r_1} - \frac{\mu}{r_2} \tag{25}$$

where p_x, p_y, p_z are the generalized momenta of the mass-less particle, μ is the mass parameter of the system (defined in Eq. (1)), r_1 and r_2 are the absolute values of the position vectors of the particle from the primary and the secondary (defined in Eq. (6)).
Following the approach initially suggested by Ross and Scheeres [5], by taking the assumption that the mass parameter μ is small, the Eq. (25) can be decomposed in two parts: a Keplerian term $\mathcal{K}$ plus a perturbative one U:

$$\mathcal{H}_{in} = \mathcal{K} + U + \mathcal{O}\left(\mu\right)^2 \tag{26}$$

Before showing the procedure to obtain the disturbing function R of the Keplerian Map, an important consideration can be done:: while in the perturbation approach shown in Section 2.1.2 the disturbing function R was computed assuming that the parameter δ of Eq. (12) is small, now there are no assumptions on the distance between the particle and the third-body. On the other hand, an important assumption is made on the mass parameter of the system μ, which is assumed to be small. This will affect the field of application of the two models. In order to remain in line with the literature and to reduce the complexity of the model, it is better to switch in polar coordinates making use of the angle θ defined as the angle between the x axis and the particle position vector from the barycentre $\mathbf{r}$, with norm r:

$$\begin{cases} r\cos\theta = x' \\ r\sin\theta = y' \end{cases} \tag{27}$$

This new reference frame $\{x', y', z'\}$ is represented in Fig. 5.

As can be deduced, this new frame follows the mass-less particle, which lies

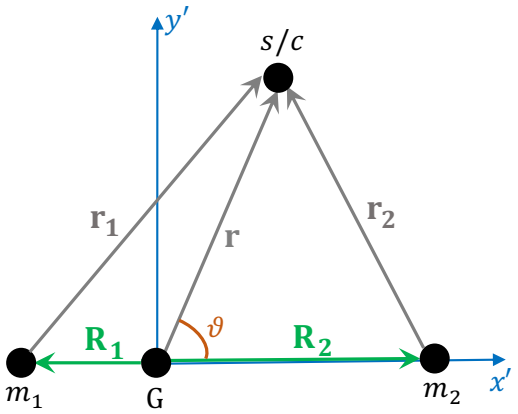

Figure 5: Barycentric reference frame $\{G, x', y', z'\}$ used in the Keplerian Map theory.

always in the $x' - y'$ plane. $\mathbf{R_1}$ represents the position vector of the primary from the centre of mass, and $\mathbf{R_2}$ the position vector of the secondary from the barycentre:

$$\mathbf{R_1} = -\mu\hat{\mathbf{x}}' \quad , \quad \mathbf{R_2} = -(1-\mu)\hat{\mathbf{x}}' \tag{28}$$

Thanks to these new coordinates, the vectors $\mathbf{r_1}$ and $\mathbf{r_2}$ (identifying the particle position from the primary and the secondary respectively), can be computed

as:

$$\begin{aligned} \mathbf{r_1} &= \mathbf{r} - \mathbf{R_1} = \begin{bmatrix} r\cos\theta + \mu \\ r\sin\theta \end{bmatrix} \\ \mathbf{r_2} &= \mathbf{r} - \mathbf{R_2} = \begin{bmatrix} r\cos\theta - 1 + \mu \\ r\sin\theta \end{bmatrix} \end{aligned} \tag{29}$$

Therefore, the norms of $\mathbf{r_1}$ and $\mathbf{r_2}$ also in Eq. (6) can be rewritten as:

$$\begin{aligned} r_1 &= \sqrt{r^2 + \mu^2 + 2\mu r\cos\theta} \\ r_2 &= \sqrt{r^2 + (1-\mu)^2 - 2(1-\mu)r\cos\theta} \end{aligned} \tag{30}$$

From Eq. (30) it is possible to write the terms K and U appearing in the Hamiltonian of Eq. (25) as [5]:

$$\begin{aligned} \mathcal{K} &= \frac{1}{2}\left(p_x^2 + p_y^2 + p_z^2\right) - \frac{1-\mu}{r} \\ U &= \mu\left(\frac{\cos\theta}{r^2} - \frac{1}{\sqrt{r^2 + 1 - 2r\cos\theta}}\right) \end{aligned} \tag{31}$$

It can be noticed that $\mathcal{K}$ is the term representing the total specific energy of the particle if the primary were located in the centre of mass, while the perturbing potential U is due to the presence of the third body and it provokes the divergence of the particle motion from its nominal Keplerian orbit.
The disturbing function R of the Keplerian Map in the CR3BP is therefore the opposite of the disturbing potential U in Eq. (31):

$$R = -U = -\mu\left(\frac{\cos\theta}{r^2} - \frac{1}{\sqrt{r^2 + 1 - 2r\cos\theta}}\right) \tag{32}$$

In order to insert the disturbing function into the Lagrange's Planetary Equations, it is necessary to reformulate the expression in Eq. (32) in function of the particle orbital elements $R = R(a, e, i, \Omega, \omega, \nu)$.
This can be done in two steps. The first one consists in writing the expression of r and $\cos\theta$ in a non-dimensional form. This can be obtained with the use of the eccentric anomaly E and the resolution of a spherical triangle [17]:

$$\begin{aligned} r &= \frac{a}{R_2}\left(1 - e\cos E\right) \\ \cos\theta &= \cos(\Omega - \theta_{3B})\cos(\omega + \nu) - \sin(\Omega - \theta_{3B})\sin(\omega + \nu)\cos i \end{aligned} \tag{33}$$

where:

$$\cos\nu = \frac{\cos E - e}{1 - e\cos E} \quad , \quad \sin\nu = \frac{\sqrt{1-e^2}\sin E}{1 - e\cos E} \tag{34}$$

The second step is the computation of the true anomaly of the third body θ_{3B} in function of the particle orbital elements. This can be obtained thanks to the fact that the third body moves on a circular orbit according to the CR3BP assumptions, by exploiting the Kepler's equation of time [1]:

$$\begin{cases} M - M_0 = n(t - t_0) \\ \theta_{3B} - \theta_{3B_0} = n_{3B}(t - t_0) \end{cases} \Bigg\| \rightarrow \theta_{3B} = \theta_{3B_0} + \left(\frac{a}{R_2}\right)^{3/2} (E - e\sin E - M_0) \tag{35}$$

By substituting Eq. (35) into Eq. (33) it is possible to write the expression of R in function of the particle orbital elements $R = R(a, e, i, \Omega, \omega, E)$. Thus, its partial derivatives can be computed and inserted into the LPE of Eq. (9).
The derivation of the Keplerian Map presented so far has been specifically developed for CR3BP. Recent studies [17] expanded this theory in the more general case of the Restricted Three-Body Problem, and obtained the expression of the disturbing function R without taking the assumption of $\mu << 1$.
Thanks to a novel demonstration, it is possible to obtain the expression of R in Eq. (32) as difference between the gravitational potentials, changed in signs, exerted by the celestial bodies in the perturbed and unperturbed motions of the particle.
This is done with the following passages:

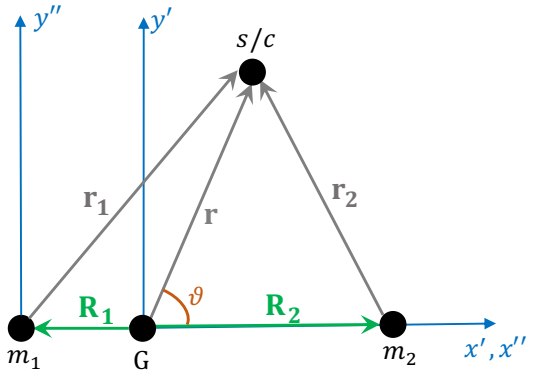

Figure 6: Perturbed reference frame $\{G, x', y', z'\}$ and unperturbed reference frame $\{m_1, x'', y'', z''\}$. Axes z' and z'' exiting from the paper.

1. Referring to the perturbed and unperturbed reference frames depicted in Fig. 6, the differential acceleration is computed as difference between the acceleration of the particle in the perturbed case, and the one in the unperturbed case [17]:

$$\delta\mathbf{a} = \mathbf{a_{pert}} - \mathbf{a_{unpert}} = \frac{1-\mu}{r_1^3}(\mathbf{r} - \mathbf{R_1}) - \frac{\mu}{r_2^3}(\mathbf{r} - \mathbf{R_2}) - \left(-\frac{1-\mu}{r^3}\mathbf{r}\right) \quad (36)$$

2. After rearranging Eq. (36), a change of variables is performed, switching from polar to Cartesian coordinates (referring to the frame $\{G, x', y', z'\}$ in Fig. 6):

$$r = \sqrt{(x')^2 + (y')^2} \quad \text{and} \quad \begin{cases} \cos\theta = \dfrac{x'}{r} \\ \sin\theta = \dfrac{y'}{r} \end{cases} \quad (37)$$

which allows to write $\delta\mathbf{a}$ in function of only x', y' and μ.

3. The differential acceleration can be seen as the gradient of the differential potential function δU:

$$\delta\mathbf{a} = \begin{bmatrix} -\dfrac{\partial\delta U}{\partial x} \\ -\dfrac{\partial\delta U}{\partial y} \end{bmatrix} \quad (38)$$

This means that by integrating the expression of $\delta\mathbf{a}$ in x' and y', and changing by sign the result, it is possible to obtain the disturbing function R.

4. As demonstration, the expression of $\delta\mathbf{a}$ in Eq. (36) in its rearranged version (expressed in function of x', y', μ) is expanded in Taylor series of μ around 0. The expression is then integrated and changed by sign, leading to the same expression of Eq. (32) if a switch in polar coordinates is done, verifying the procedure.

Thus, it has been demonstrated that the disturbing function of the Keplerian Map can be obtained without making the assumption of the small parameter μ, and it can be written as summation of the gravitational potentials acting on the particle [17] as:

$$R = -\left(-\frac{1-\mu}{r_1}\right) - \left(-\frac{\mu}{r_2}\right) + \left(-\frac{1-\mu}{r}\right) \quad (39)$$

The first and the second terms in Eq. (39) are the gravitational potentials exerted on the particle by the primary and the secondary attractor bodies that are moving around the barycentre of the system. The last term is the gravitational potential that the primary would exerts if it was located in the barycentre. It can be noticed that in all the terms appearing in Eq. (39), the minus sign is highlighted in order to recall the fact that the disturbing function is none but the disturbing potential U changed by sign.
The exact expression of R can now be expressed in function of the particle orbital elements, such that it is possible to compute its partial derivatives to be inserted into the LPE.
This can be done extending the application to the R3BP without making the assumption that the third body moves on a circular orbit around the barycentre. Such assumption implies that now it is not possible to express the third body true anomaly in function of the particle eccentric anomaly as in Eq. (35). Indeed, now it is not possible to obtain the exact position of the secondary knowing just the position of the particle, but it can be achieved whenever the use of the ephemerides is possible.
To remain in the same framework of the three-body problem, a dimensionless form of the Keplerian Map is obtained, where the distance from the primary and the secondary is equal to one. Moreover, from the definition of the barycentre it is possible to write that:

$$\mathbf{R_1} = \frac{\mu}{1-\mu}\mathbf{R_2} \tag{40}$$

Thus, the expression of the primary and the secondary position vectors from the centre of mass of the system can be computed as:

$$\mathbf{R_1} = \begin{bmatrix} -\dfrac{\mu}{1-\mu}\dfrac{1-e_{3B}^2}{1+e_{3B}\cos\theta_{3B}} \\ \\ 0 \end{bmatrix}, \quad \mathbf{R_2} = \begin{bmatrix} \dfrac{1-e_{3B}^2}{1+e_{3B}\cos\theta_{3B}} \\ \\ 0 \end{bmatrix} \tag{41}$$

The expression of the position vector of the particle with respect to the barycentre can be written as:

$$\mathbf{r} = \begin{bmatrix} r\cos\theta \\ \\ r\sin\theta \end{bmatrix} \tag{42}$$

Thanks to Eq. (42) and Eq. (41), exploiting the same relations in Eq. (29), the norms of the position vectors of the mass-less particle with respect to the

primary and the secondary are [17]:

$$r_1 = \sqrt{r^2 + \frac{\mu^2}{(1-\mu)^2}\left(\frac{1-e_{3B}^2}{1+e_{3B}\cos\theta_{3B}}\right)^2 + 2r\frac{\mu}{1-\mu}\cos\theta\frac{1-e_{3B}^2}{1+e_{3B}\cos\theta_{3B}}}$$
$$r_2 = \sqrt{r^2 + \left(\frac{1-e_{3B}^2}{1+e_{3B}\cos\theta_{3B}}\right)^2 - 2r\cos\theta\frac{1-e_{3B}^2}{1+e_{3B}\cos\theta_{3B}}} \tag{43}$$

After the substitution of r, r_1 and r_2 into Eq. (39), the disturbing function becomes [17]:

$$R = \frac{1-\mu}{\sqrt{r^2 + \frac{\mu^2}{(1-\mu)^2}\left(\frac{1-e_{3B}^2}{1+e_{3B}\cos\theta_{3B}}\right)^2 + 2r\frac{\mu}{1-\mu}\cos\theta\frac{1-e_{3B}^2}{1+e_{3B}\cos\theta_{3B}}}} +$$
$$+ \frac{\mu}{\sqrt{r^2 + \left(\frac{1-e_{3B}^2}{1+e_{3B}\cos\theta_{3B}}\right)^2 - 2r\frac{1-e_{3B}^2}{1+e_{3B}\cos\theta_{3B}}}} - \frac{1-\mu}{r} \tag{44}$$

The remaining terms that shall be written in function of the particle orbital elements are the radial distance from the centre of mass r and the $\cos\theta$. The first one can easily be written in dimensionless form as:

$$r = \frac{a}{a_{3B}}\frac{1-e^2}{1+e\cos\nu} \tag{45}$$

while the $\cos\theta$ can be obtained from the scalar product of $\hat{\mathbf{r}}$ and $\hat{\mathbf{R}}_\mathbf{2}$ in the inertial frame:

$$\left\{\begin{array}{l} \hat{\mathbf{r}}^{\mathbf{in}} = R_3(\Omega)R_1(i)R_3(\omega+\nu)\begin{bmatrix}1\\0\\0\end{bmatrix} \\ \\ \hat{\mathbf{R}}_\mathbf{2}^{\mathbf{in}} = R_3(\Omega_{3B})R_1(i_{3B})R_3(\omega_{3B}+\theta_{3B})\begin{bmatrix}1\\0\\0\end{bmatrix} \end{array}\right\| \rightarrow \cos\theta = \hat{\mathbf{r}}^{\mathbf{in}}\cdot\hat{\mathbf{R}}_\mathbf{2}^{\mathbf{in}} \tag{46}$$

Now the disturbing function of Eq. (44) can be written in terms of only the particle orbital elements thanks to Eq. (45) and Eq. (46): $R = R(a, e, i, \Omega, \omega, \nu)$,

assuming that the position of the third body is known from an ephemerides model.
In the case that this is not possible, an approximated solution can be obtained by assuming that the orbit of the third body has low eccentricity e_{3B}, thus [1]:

$$\begin{aligned} M_{3B} = E_{3B} - e_{3B}\sin E_{3B} \approx E_{3B} = \left(\frac{a}{a_{3B}}\right)^{3/2}(E - e\sin E) + M_{3B_0} \\ \theta_{3B} = \arctan\sqrt{\frac{1+e_{3B}}{1-e_{3B}}}\tan\frac{E_{3B}}{2} \end{aligned} \tag{47}$$

with M_{3B}, E_{3B} and M_{3B_0} the mean anomaly, eccentric anomaly and initial mean anomaly of the third body.
The disturbing function to be adopted inside the LPE has to be dependent on six constant orbital elements and time, where constant means that under the hypothesis of Keplerian motion, they do not change with time. Therefore, it is necessary to write the particle true anomaly in function of the time and the initial mean anomaly. This can be achieved through the following relations [1]:

$$\begin{aligned} \nu = 2\arctan\sqrt{\frac{1+e}{1-e}}\tan\frac{E}{2} \\ E - e\sin E = nt + M_0 = \sqrt{(1-\mu)\left(\frac{a_{3B}}{a}\right)^3}t + M_0 \end{aligned} \tag{48}$$

Finally, the disturbing function is ready to be partially derived, being dependent on [17]:

$$R = R\left(a, e, i, \Omega, \omega, \nu\left(E(a, e, M_0, t), e\right)\right) \tag{49}$$

The partial derivatives of the disturbing function with respect to the orbital elements can be written as [17]:

$$\begin{cases} \dfrac{dR}{da} = \dfrac{\partial R}{\partial a} + \dfrac{\partial R}{\partial \nu}\dfrac{\partial \nu}{\partial E}\dfrac{\partial E}{\partial a} \\ \dfrac{dR}{de} = \dfrac{\partial R}{\partial e} + \dfrac{\partial R}{\partial \nu}\left(\dfrac{\partial \nu}{\partial e} + \dfrac{\partial \nu}{\partial E}\dfrac{\partial \nu}{\partial E}\dfrac{\partial E}{\partial e}\right) \\ \dfrac{dR}{di} = \dfrac{\partial R}{\partial i} \quad ; \quad \dfrac{dR}{d\Omega} = \dfrac{\partial R}{\partial \Omega} \quad ; \quad \dfrac{dR}{d\omega} = \dfrac{\partial R}{\partial \omega} \\ \dfrac{dR}{dM_0} = \dfrac{\partial R}{\partial \nu}\dfrac{\partial \nu}{\partial E}\dfrac{\partial E}{\partial M_0} \end{cases} \tag{50}$$

where the notation of the total derivative is used just to highlight that in reality the orbital elements depend themselves on the true anomaly, thus even a partial derivative shall be decomposed in more terms, as sufficiently explained in literature [17].
The partial derivatives of ν and E appearing in the right terms of Eq. (50) can be analytically obtained from the following relations [17]:

$$
\begin{aligned}
&\bullet \left\{ \begin{array}{l} \cos\nu = \dfrac{\cos E - e}{1 - e\cos E} \\ \\ \sin\nu = \dfrac{\sqrt{1-e^2}\sin E}{1 - e\cos E} \end{array} \right\| \rightarrow \left\{ \begin{array}{l} \dfrac{\partial\nu}{\partial E} = \dfrac{\partial\nu}{\partial\cos\nu}\dfrac{\partial\cos\nu}{\partial E} = \dfrac{1+e\cos\nu}{\sqrt{1-e^2}} \\ \\ \dfrac{\partial\nu}{\partial e} = \dfrac{\partial\nu}{\partial\cos\nu}\dfrac{\partial\cos\nu}{\partial e} = \dfrac{\sin\nu}{1-e^2} \end{array} \right. \\
&\bullet\ a = \left(\frac{E - e\sin E - M_0}{\sqrt{a_{3B}^3(1-\mu)}t} \right)^{-2/3} \rightarrow \ \frac{\partial E}{\partial a} = \left(\frac{\partial a}{\partial E} \right)^{-1} = -\frac{3}{2a}\frac{E - e\sin E - M_0}{1 - e\cos E} \\
&\bullet\ e = \frac{E}{\sin E - \dfrac{nt + M_0}{\sin E}} \ \rightarrow \ \frac{\partial E}{\partial e} = \left(\frac{\partial e}{\partial E} \right)^{-1} = \frac{\sin\nu}{\sqrt{1-e^2}} \\
&\bullet\ M_0 = E - e\sin E - nt \ \rightarrow \ \frac{\partial E}{\partial M_0} = \left(\frac{\partial M_0}{\partial E} \right)^{-1} = \frac{1+e\cos\nu}{1-e^2}
\end{aligned}
\tag{51}
$$

Once the derivatives of R are computed, the evolution with time of the particle orbital elements can be obtained by using the LPE.
Note that the Keplerian Map theory has two different possible bifurcations from this point on, as it is explained in the following Section 2.2.1 and Section 2.2.2. However, before proceeding with them, a consideration on the mathematical model just derived can be done.
From the definition of the system in the theory, it shall be remarked that the particle orbital elements that are used are a fictitious set. Indeed, as shown in Fig. 5, the radial distance r in Eq. (45) of the mass-less particle is computed from the barycentre of the system, and not from the primary. This fact has an important consequence, and can be considered as the main reason for the error introduced when using the Keplerian Map: when the primary attractor and the barycentre are considerably distant, a large variation of the fictitious orbital elements does not correspond to the same variation that the real orbital elements undergo. This happens in close encounters when the mass parameter

of the system μ is not so small, as in the Earth-Moon system.
Therefore, even if the derivation of the mathematical model has been done without taking assumptions on the mass parameter of the system for the general case of the R3BP, carefulness shall be applied with the application of the method. This is also discussed in Section 3.

2.2.1 Semi-analytical approach

The initial goal of the Keplerian Map theory was to predict the variation of the particle orbital elements during one orbital period in a distant encounter with the third body, through a semi-analytical method. In order to avoid the numerical integration of the Lagrange's Planetary Equations, it is possible to apply the first Picard's iteration [24] to approximate the integration over one orbital period.
The Picard's procedure is an analytical approximation of a differential equation. It is an iterative procedure that allows to obtain more and more accurate results by increasing the number of iterations performed, and it is valid only if the time span is sufficiently small [13]. To approximate the integration of the LPE, just the first Picard's iteration is sufficient. The discrete variation of each orbital element during one orbital period is computed as in Eq. (54) [13], where E_i and E_f represents the initial and final particle eccentric anomaly. Note that the discrete "kick" of the orbital elements is assumed to happen all at the pericentre of the particle orbit (the nearest point with respect to the secondary) [5].
The integral variable chosen is the eccentric anomaly rather than the time since in reality the orbital period is not constant due to the semi-major axis variation.
This approach seems by now to be only analytical. However, the integrals appearing in Eq. (54) can be easily computed with a numerical procedure. Different integration schemes can be adopted, one of them is the Simpson's integration rule [25]:

$$I_{\alpha_i}^{j+1} = I_{\alpha_i}^{j} + \frac{d\nu}{6}\left(\left.\frac{\partial R}{\partial \alpha_i}\right|_{\nu=\nu_{j-1}} + 4 \left.\frac{\partial R}{\partial \alpha_i}\right|_{\nu=\nu_{j}} + \left.\frac{\partial R}{\partial \alpha_i}\right|_{\nu=\nu_{j+1}} \right) \tag{52}$$

where $d\nu$ is the step in true anomaly and [17]:

$$I_{\alpha_i} = \int_{\nu_i}^{\nu_f} \frac{\partial R}{\partial \alpha_i} d\nu \tag{53}$$

$$\begin{cases} \Delta a = \dfrac{2}{n^2 a} \displaystyle\int_{E_i}^{E_f} \frac{\partial R}{\partial E} dE \\ \Delta e = \dfrac{1-e^2}{n^2 a^2 \sin i} \displaystyle\int_{E_i}^{E_f} \frac{\partial R}{\partial E} dE - \frac{(1-e^2)^2}{n^2 a^2 e} \int_{E_i}^{E_f} \frac{\partial R}{\partial \omega} (1 - e\cos E)\, dE \\ \Delta i = -\dfrac{1-e^2}{n^2 a^2 \sin i} \displaystyle\int_{E_i}^{E_f} \frac{\partial R}{\partial \Omega} (1 - e\cos E)\, dE + \\ \qquad\qquad + \dfrac{(1-e^2)\cos i}{n^2 a^2 \sin i} \displaystyle\int_{E_i}^{E_f} \frac{\partial R}{\partial \omega} (1 - e\cos E)\, dE \\ \Delta \Omega = -\dfrac{1-e^2}{n^2 a^2 \sin i} \displaystyle\int_{E_i}^{E_f} \frac{\partial R}{\partial i} (1 - e\cos E)\, dE \\ \Delta \omega = -\dfrac{(1-e^2)^2}{n^2 a^2 e} \displaystyle\int_{E_i}^{E_f} \frac{\partial R}{\partial e} (1 - e\cos E)\, dE + \\ \qquad\qquad - \dfrac{(1-e^2)^2}{n^2 a^2 \sin i} \displaystyle\int_{E_i}^{E_f} \frac{\partial R}{\partial i} (1 - e\cos E)\, dE \end{cases} \tag{54}$$

2.2.2 Numerical Approach

The main drawback in using a semi-analytical approach to solve the LPE, is that it does not allow to track the evolution of the orbital elements inside the extremes of integration. This is something that can be acceptable when searching for preliminary solutions, but not when a detailed and complete orbital elements variation is needed.

However, in certain applications may be useful to obtain the full evolution with time of the particle orbital elements, and this can be done by numerically integrating the Lagrange's Planetary Equations.
That procedure is necessary especially when the variation of the orbital elements is extremely large and when the time span of the propagation is large. Indeed, by applying successives Picard's procedures there is a small error introduced at each iteration, that becomes large if the number of periods considered is high.
The easiest and the fastest way to integrate Eq. (9) is to use an ODE solver available in different programming languages.
A simple one-step or multi-step solver can be used. Since an high tolerance is necessary in general when integrating space systems models, the best choice could be to use an explicit Runge-Kutta $4^{th} - 5^{th}$ order scheme, or a multi-step variable order method as the Adams-Bashforth-Moulton scheme. These two schemes can be used in MATLAB® software under the names of `ode45` and `ode113` respectively. In the present work the latter is preferred since the computational time required does not change significantly even for long integration, and it has an higher accuracy at stringent tolerances [26].
It is important to remark that in this thesis the numerical approach has been preferred to the semi-analytical one. Indeed, with the numerical integration of the LPE it is possible to save computational time with respect to the procedure needed to solve them in the semi-analytical approach. Moreover, the orbital elements evolution during the whole period is needed to compare the results of the Keplerian Map propagation with the ones of the three-body problem.

2.2.3 The Kick Map

An useful way to apply the Keplerian Map is to compute the kick in orbital elements obtained by each distant encounter, in function of the initial phase angle between the particle and the third body.
A Kick Map for a given osculating orbital element is defined as the set of variations experienced by the given orbital element over one orbital period, in function of the relative angular phasing between the initial position of the mass-less particle and the third body [13].
In the case of the CR3BP, the phasing angle γ_{CR3BP} can be obtained from the resolution of the spherical triangle represented in Fig. 7, through the use of the

cotangent law [17]:

$$\gamma_{CR3BP} = \Omega - \theta_{3B_0} + \arctan\cos i \tan\omega \tag{55}$$

In the case of the R3BP the expression of the phasing angle γ becomes more complicated since now the third body does not move on a circular orbit. Considering the two spherical triangles depicted in Fig. 8, by applying the cotangent law to the orange triangle [17]:

$$\cos z \cos i = \cot\omega \sin z \quad \rightarrow \quad z = \arctan\tan\omega\cos i \tag{56}$$

and applying it to the green triangle:

$$\cos z + \Delta\Omega \cos i_{3B} = \cot\gamma + \omega_{3B} + \theta_{3B} \sin z + \Delta\Omega \tag{57}$$

where $\Delta\Omega = \Omega - \Omega_{3B}$.
If the Eq. (56) is substituted into Eq. (57), after an algebraic manipulation is possible to obtain the phasing angle [17]:

$$\gamma = \arctan\left(\frac{1}{\cos i_{3B}} \tan(\arctan(\tan\omega\cos i) + \Delta\Omega)\right) - \omega_{3B} - \theta_{3B} \tag{58}$$

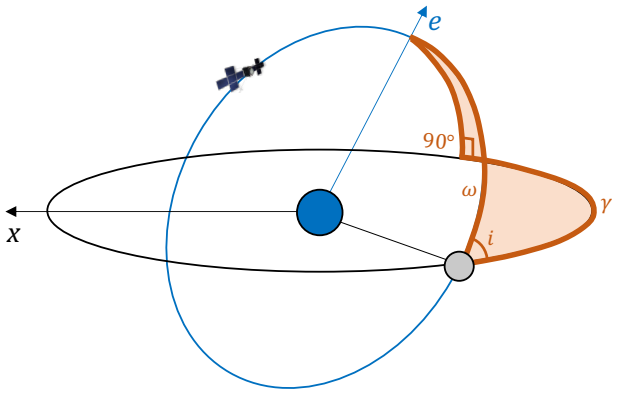

Figure 7: Spherical triangle used to obtain the expression of the phasing angle γ_{CR3BP}.

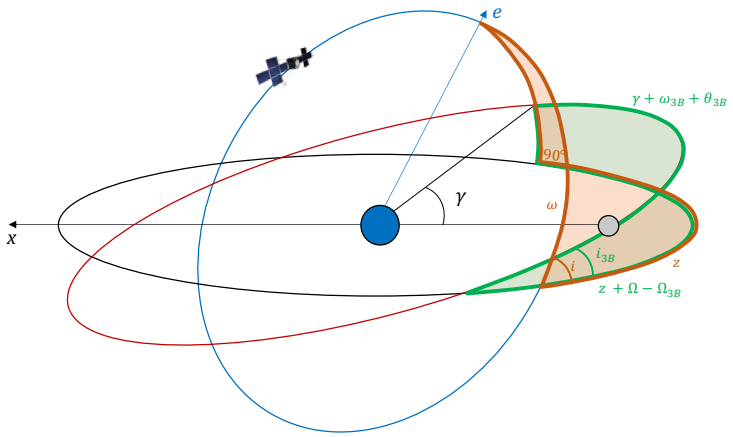

Figure 8: Spherical triangles used to obtain the expression of the phasing angle γ in the R3BP context.

CHAPTER 3

Limits of the Keplerian map theory

THE mathematical model of the Keplerian Map has been obtained in Section 2.2, without making assumptions on the mass parameter of the system μ. This theory can be usefully exploited for a high-fidelity prediction of the motion of a spacecraft influenced by the presence of a third-body. However, it is not always possible to apply it, since the prediction can be not sufficiently accurate in particular situations.
In this chapter the studies done to identify the limits for the application of the Keplerian Map theory are presented, highlighting the dynamical analysis of the model and its dependence on particular parameters of a system. A massive number of simulations have been performed to identify the optimal conditions in which this theory can be applied.
The accuracy of the model is measured through an error, computed as difference between a state of the spacecraft obtained with the Keplerian Map propagation and the same state obtained with a theory considered exact (e.g. the R3BP). The strategy used to compare the propagation of the particle motion exploiting the Keplerian Map and the Three-Body Problem is a sensitivity analysis, where particular parameters of the system are made to vary by changing the initial conditions of the system. Each initial condition is then propagated for one orbital period with the Keplerian Map, and the final states are compared with the ones obtained with the three-body problem model.
Before presenting the analysis done, it is important to highlight one more time a core concept about the definition of the Keplerian Map theory. As explained in Section 2.2, the peculiarity of this method is that the orbital elements of the particle are referred to the centre of mass of the system and not to the primary body. Hence, the variation that they experience due to the presence of the third body is not the same variation experienced by a set of orbital elements

referred to the main attractor. The difference between them becomes larger when the barycentre of the system is significantly displaced from the main attractor, meaning that the mass parameter of the system μ is high. Moreover, if the encounter between the particle and the third body happens very close (e.g. inside the 3^{rd} body SOI), the variation of the orbital elements experienced is large, as the error with respect to the variation of the orbital elements referred to the main attractor.
The mass parameter of the system can be seen as a weight of the third-body effect on the spacecraft dynamics. An high mass parameter implies that the effect of the disturber is strongly influencing the motion of the particle. Hence, it is clear that for high mass parameters, a close encounter of the particle with the third body provokes a large variation of its orbital motion, following a large error of the Keplerian Map with respect to the solution proposed by the Three-Body Problem.
The mass parameter of the system μ plays undeniably a key role when searching for an applicability domain of the Keplerian Map; therefore, its dependence will be always included in the analyses done in this chapter, since it represents the main indicator of the third body effect.

3.1 Jacobi Constant dependence

In the context of the CR3BP, as presented in Section 2.1.1, the Jacobi Constant is an integral of motion that remains constant during the motion of the particle.
This is valid in the Synodic reference frame (reported in Fig. 2), which rotates following the secondary attractor that lies on the x axis. In this frame the value of the Jacobi Constant can be written as in Eq. (8), or as:

$$C_J = x^2 + y^2 + 2\left(\frac{1-\mu}{r_1}\right) + 2\left(\frac{\mu}{r_2}\right) - v^2 \tag{59}$$

where r_1 and r_2 are reported in Eq. (6). The value of the Jacobi constant (also called Jacobi integral) is a measure of the total energy $\mathcal{E}$ that a particle has in the Synodic frame, that is defined as:

$$\mathcal{E} = \frac{1}{2}v^2 + U = \frac{1}{2}v^2 - \frac{1}{2}(x^2+y^2) - \left(\frac{1-\mu}{r_1} + \frac{\mu}{r_2}\right) \tag{60}$$

Therefore, from Eq. (59) and Eq. (60) it is possible to obtain that:

$$\mathcal{E} = -\frac{1}{2}C_J \tag{61}$$

This latter relation explains that high values of C_J corresponds to low values of $\mathcal{E}$, and viceversa.
The theory of the Keplerian Map starts from the expression of the Hamiltonian of the CR3BP (as shown in Section 2.2), which contains the particle's Keplerian energy of the two-body problem and a perturbing term [5].
In this sense, there is a dependence on the energy of the particle in the Keplerian Map theory. Therefore, an accurate analysis of the error introduced when propagating with the Keplerian Map is now presented, searching for a relation of this error with the value of the Jacobi Constant (being an indicator of the particle total energy in the Synodic frame).

3.1.1 Synodic reference frame and Libration points

As it was described in Section 2.1.1, in the Synodic reference frame there exist 5 equilibrium points named Libration points (depicted in Fig. 3). These points correspond to maximum/minimum or saddle points of the potential energy of the particle, and they have different stability properties:

- The three collinear points L_1, L_2 and L_3 are unstable equilibrium points
- The two triangular points L_4 and L_5 are stable equilibrium points

For each Libration point it corresponds to a certain energy value $\mathcal{E}_{L_i}$, and a value of the Jacobi Constant C_{L_i}. This can be exploited to understand the allowed realm of the particle that moves with a certain C_J, through the concept of the zero velocity curves [3]. In particular, for a given μ it is possible to compute the position of the Libration points and the value of the particle energy at rest on these points, such that: $\mathcal{E}_{L_5} = \mathcal{E}_{L_4} > \mathcal{E}_{L_3} > \mathcal{E}_{L_2} > \mathcal{E}_{L_1}$, or inversely: $C_{L_1} > C_{L_2} > C_{L_3} > C_{L_4} = C_{L_5}$.
The allowed realm for each value of C_{L_i} is represented in Fig. 9.
The coordinates in the Synodic frame x, y, z are usually taken in a dimensionless form. The position of the particle and its velocity are transformed in dimensionless units through the characteristic length and characteristic time:

$$\begin{cases} L^* = R_{3B} \\ t^* = T_{3B} \end{cases} \tag{62}$$

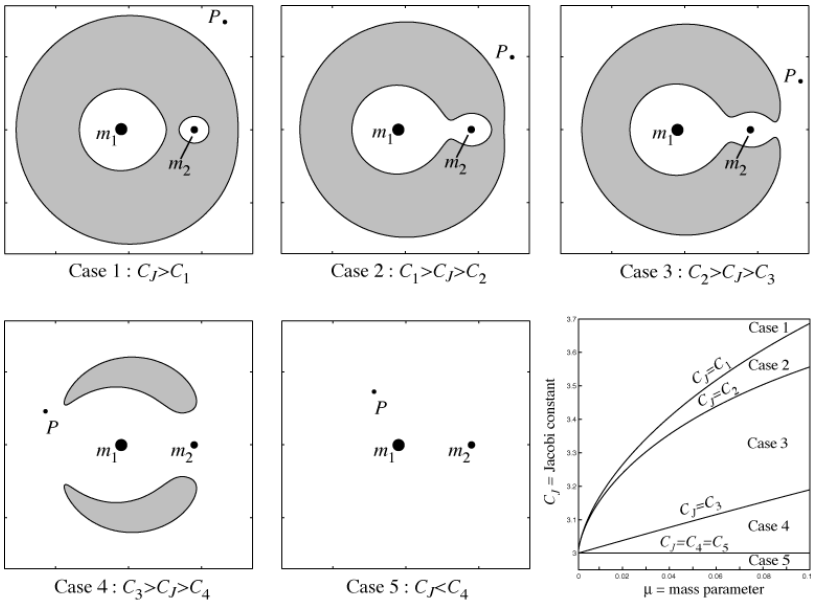

Figure 9: Zero velocity curves for five values of the Jacobi constant C_J (one in each of the cases), computed for a test case with $\mu = 0.3$. Particle's position denoted with P, gray regions are forbidden and white regions are allowed. In the last subfigure on the right it is represented how the value of C_{L_i} changes with the value of μ [3].

where R_{3B} is the distance between primary attractor and third body (it is equal to a_{3B}, that remains constant in the CR3BP), and T_{3B} is the period of rotation of the third body around the barycentre. Therefore, the relation between dimensionless and dimensional particle's states is:

$$\begin{cases} \mathbf{r}^* = \dfrac{\mathbf{r}}{L^*} \\ \mathbf{v}^* = \dfrac{t^*}{L^*}\mathbf{v} \end{cases} \tag{63}$$

Another transformation that can be mentioned is the switch from the Synodic reference frame (shown in Fig. 2) to the inertial barycentric frame (shown in Fig. 1). This change of coordinates can be achieved by exploiting a rotation along the z axis of an angle θ, that identifies the position of the third body with respect the X axis of the inertial frame. To obtain the states of the particle in the Synodic reference frame by knowing them in the inertial barycentric

reference frame, the following relation must be applied:

$$\begin{cases} \mathbf{r_{in}} = R_\theta \cdot \mathbf{r_{syn}} \\ \mathbf{v_{in}} = R_\theta \cdot \mathbf{v_{syn}} + \dot{R}_\theta \cdot \mathbf{r_{syn}} \end{cases} \tag{64}$$

in which the rotation matrix R_θ and its derivative $\dot{R}_\theta$ that shall be used are:

$$R_\theta = \begin{bmatrix} \cos\theta & -\sin\theta & 0 \\ \sin\theta & \cos\theta & 0 \\ 0 & 0 & 1 \end{bmatrix} \quad \text{and} \quad \dot{R}_\theta = n \begin{bmatrix} -\sin\theta & -\cos\theta & 0 \\ \cos\theta & -\sin\theta & 0 \\ 0 & 0 & 0 \end{bmatrix} \tag{65}$$

where $n = \dot{\theta} = const.$ is the mean motion of the third body around the barycentre of the system.
In order to compute the values of C_{L_i} (or equivalently, $\mathcal{E}_{L_i}$), it is necessary to compute the position of the Libration points in the Synodic dimensionless frame. They can be computed by imposing:

$$\nabla U \stackrel{!}{=} 0 \tag{66}$$

where U is the three-body potential defined in Eq. (7). The triangular points L_4 and L_5 are situated in a symmetric position with respect to the third body, being their coordinates:

$$L_4 = \left[\frac{1}{2} - \mu\,,\, \frac{\sqrt{3}}{2}\,,\, 0\right]^T \quad \text{and} \quad L_5 = \left[\frac{1}{2} - \mu\,,\, -\frac{\sqrt{3}}{2}\,,\, 0\right]^T \tag{67}$$

The position of the collinear points L_1, L_2 and L_3 is instead computed from a nonlinear equation [1] that has three different solutions, identifying the coordinates x_{L_i} such that $L_i = [x_{L_i}\,,\, 0\,,\, 0]^T$. The nonlinear equation is the following one:

$$\frac{1-\mu}{|x+\mu|^3}(x+\mu) + \frac{\mu}{|x-(1-\mu)|^3}(x-(1-\mu)) - x = 0 \tag{68}$$

and it can be solved by a common nonlinear solver, choosing three different initial conditions x_0:

- The value of x_{L_1} is obtained if $0 < x_0 < 1$
- The value of x_{L_2} is obtained if $x_0 > 1$
- The value of x_{L_3} is obtained if $x_0 < 0$

By exploiting the aforementioned equations, it is always possible to compute the Jacobi Constant at a certain Libration point C_{L_i} and to switch from the inertial reference frame to the Synodic dimensionless frame (and viceversa).

3.1.2 Jacobi Constant - Mass parameter - Error Map

Now that the Jacobi integral has been introduced, and after that basic concepts related to the CR3BP have been presented, it is possible to enter in the core of the current analysis.
The idea of this analysis is first of all to build a map that relates the following three parameters:

- The value of the mass parameter of the system μ
- The value of the Jacobi Constant, hence the total energy of the particle in the three-body problem
- The error introduced when propagating the motion of the particle with the Keplerian Map theory, with respect to the solution proposed by the CR3BP equations

This has been done by performing several propagation of the particle's motion by changing each time the initial conditions of the system. Every propagation is performed firstly with the numerical integration of the CR3BP equations (Eq. (5)), then with the numerical integration of Keplerian Map (scheme resumed in Section 2.2.2). The integration is always performed for a period of the particle, and then the two results are compared by computing an error ε. The block scheme representing the algorithm used to build the $C_J - \mu - \varepsilon$ Map is depicted in Fig. 10.

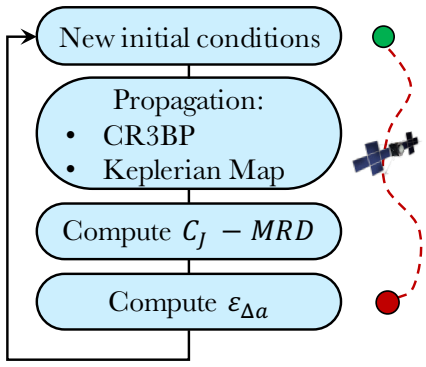

Figure 10: Blocks scheme summarizing the procedure to obtain the $C_J - \mu - \varepsilon_{\Delta a}$ Map and the $MRD - \mu - \varepsilon_{\Delta a}$ Map.

The procedure can be explained with the following passages:

1. A set of initial conditions for the system are chosen, being the initial states of the particle (position and velocity) or its initial orbital elements, and the the same for the third body.
2. The equations of the CR3BP are numerically integrated for a particle's orbital period

3. For the same time span a numerical integration of the Keplerian Map theory is performed

4. The two results are compared with different kinds of errors. They are computed at the end of the integration and at the pericentre of the particle orbit with respect to the third body. Multiple types of error have been analysed to highlight the dependence on the studied parameter

5. Some initial parameters related to the mass-less particle are let to vary, in order to change the value of the Jacobi Constant C_J and obtain different initial conditions. The initial conditions of the third body are instead kept fixed. A huge loop is run that examines hundreds of thousands of cases by just iterating this procedure with different initial conditions

Table 1: Block particle initial conditions used to build the $C_J - \mu - \varepsilon_{\Delta a}$ Map and the $MRD - \mu - \varepsilon_{\Delta a}$.

Orbital element	Initial value
Semi-major Axis	$a_0 \in [0.3\ ,\ 1.5] \cdot a_{3B_0}$
Eccentricity	$e_0 = 0.5$
Inclination	$i_0 = 10$ deg
RAAN	$\Omega_0 = 345$ deg
Argument of pericentre	$\omega_0 = 25$ deg
True Anomaly	$\nu_0 \in [0\ ,\ 360]$ deg

Before presenting a single final result that summarizes all the different quantities and calculations that have been done, it is necessary to introduce the definition of error used. Initially, the comparison between the CR3BP and the Keplerian Map propagation was done through a relative percentage error on the final value of the particle's semi-major axis after a period:

$$\varepsilon_{\Delta a}^{rel} = \left| \frac{\Delta a^{CR3BP} - \Delta a^{KM}}{\Delta a^{CR3BP}} \right| \cdot 100 \tag{69}$$

where a^{CR3BP} is the value of the particle's semi-major axis after a propagation of the CR3BP equations and a^{KM} is the semi-major axis after a propagation with the numerical Keplerian Map procedure. This relative percentage error shall be coupled with the absolute error, since when Δa tends to 0, then the

relative one tends to infinity. Therefore, the study of the behavior of $\varepsilon^{rel}_{\Delta_a}$ shall be coupled with the study of the absolute error.
To avoid this procedure, in general what is done is to adopt an error similar to the relative one, but that avoids to tend to infinity. This error is defined as:

$$\varepsilon_{\Delta a} = \left| \frac{\Delta a^{CR3BP} - \Delta a^{KM}}{\Delta a^{CR3BP} + 1} \right| \cdot 100 \tag{70}$$

A further consideration can be done regarding the choice of which semi-major axis variation to take for the computation of the error in Eq. (70). To this purpose, it is necessary to recall that the Keplerian Map theory is in general applied in its semi-analytical version (explained in Section 2.2.1), since it avoids to perform a numerical integration. From the semi-analytical formulation it is possible to compute only the variation of the particle orbital elements in a certain true anomaly interval. However, in a detailed analysis as the current one, it may be necessary to know the orbital elements evolution during the whole time period, and not only at its boundaries. The latter consideration explains why the numerical version of the Keplerian Map has been used in this analysis. Even if the error is computed with the semi-major axis variation during one orbital period, it has been obtained that the results are analogous even when taking the maximum variation of semi-major axis over the period.

Table 2: Initial conditions of the third body used to build the $C_J - \mu - \varepsilon_{\Delta a}$ Map and the $MRD - \mu - \varepsilon_{\Delta a}$.

Orbital Element	Initial Value
a_{3B_0} [km]	383078.81
i_{3B_0} [deg]	25.84
Ω_{3B_0} [deg]	10.47
ω_{3B_0} [deg]	236.82
ν_{3B_0} [deg]	177.25

The set of initial conditions that are used to build the error maps that will be presented in this chapter are listed in Table 1 for the particle, and in Table 2 for the third body. The wide ranges of initial semi-major axis and true anomaly allow to compare very different situations, where the particle motion starts far or close to the third body, with large or small Jacobi Constant.
The $C_J - \mu - \varepsilon_{\Delta a}$ Map is depicted in Fig. 11.

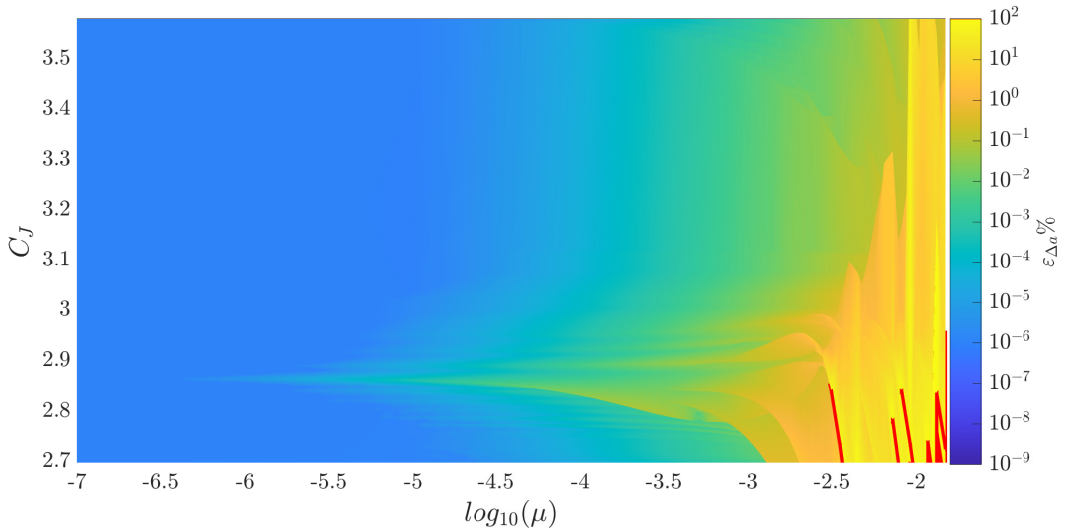

Figure 11: $C_J - \mu - \varepsilon_{\Delta a}$ Map. Red regions identify errors in the numerical integration of the Lagrange's Planetary Equations. Color-map showing the relative percentage error defined in Eq. (70).

The X-axis is the logarithmic variation of the mass parameter of the system, while the Y-axis is the variation of the Jacobi Constant. The color-map shows the logarithmic variation of the error for the different cases.
The red zones represent where the numerical integration of the Keplerian Map fails. These cases represent those initial conditions that lead to hyperbolic trajectories for which the Lagrange's Planetary Equations written in Eq. (9) are no more valid, and the ODE solver used stops the integration. Thus, it is not appropriate to associate these cases as if they were model errors, and they have been marked with a different color.
The error spans from low to significant values, and the first dependence that stands out is the one on the mass parameter μ. Increasing the mass parameter of the system, the error increases almost linearly. For high values of μ it is clear that the Keplerian Map cannot be used for almost all the values of C_J. To help the reading of the Fig. 11 in terms of mass parameter, the results can be observed coupled with Table 3, in which the mass parameters of the most common systems are listed. The Earth-Moon system seems to be inaccessible for the Keplerian Map theory, being its mass parameter of the highest. This was expected from the consideration about the dependence on μ, explained in the first part of the chapter, and now it has been confirmed.

Table 3: Mass parameters μ for most common systems studied in the Three-Body Problem field [27].

Main attractor	Third Body	Mass parameter μ
Sun	Jupiter	$9.537 \cdot 10^{-4}$
Sun	Earth + Moon	$3.036 \cdot 10^{-6}$
Earth	Moon	$1.215 \cdot 10^{-2}$
Mars	Phobos	$1.667 \cdot 10^{-8}$
Mars	Deimos	$2.310 \cdot 10^{-9}$
Jupiter	Io	$4.704 \cdot 10^{-5}$
Jupiter	Europa	$2.517 \cdot 10^{-5}$
Jupiter	Ganymede	$7.804 \cdot 10^{-5}$
Jupiter	Callisto	$5.667 \cdot 10^{-5}$
Saturn	Mimas	$6.723 \cdot 10^{-8}$
Saturn	Titan	$2.366 \cdot 10^{-4}$
Neptune	Triton	$2.089 \cdot 10^{-4}$
Pluto	Charon	$1.097 \cdot 10^{-1}$

On the other hand, systems where the mass of the third body is several order of magnitudes smaller than the one of the main attractor are suitable cases (with some exceptions as will be shown). For example, trajectories in the Jovian system and in Martian environment can be propagated with the Keplerian Map.
While the dependence on μ is very evident, it is not so clear the influence of the Jacobi Constant on the error. For high values of C_J and relatively small values of μ the method appears to work well, with an error that remains below 10^{-4} %. In the lower part, there is a raised region in which the error grows, remaining high even for small values of μ.
An interesting feature can be seen inserting into the plot of Fig. 11 the lines corresponding to C_{L_i}.

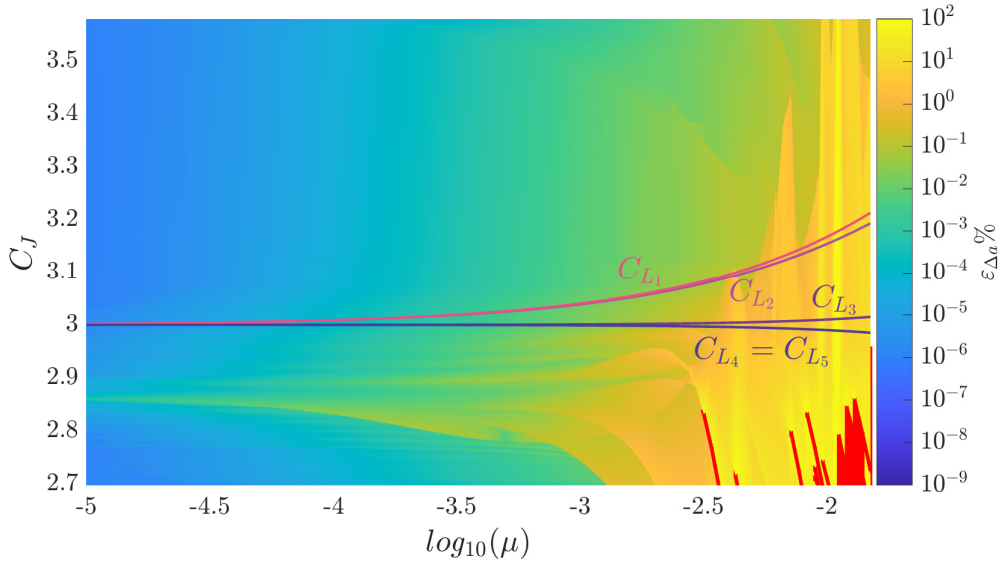

(a) $C_J - \mu - \varepsilon_{\Delta a}$ Map with C_{L_i}

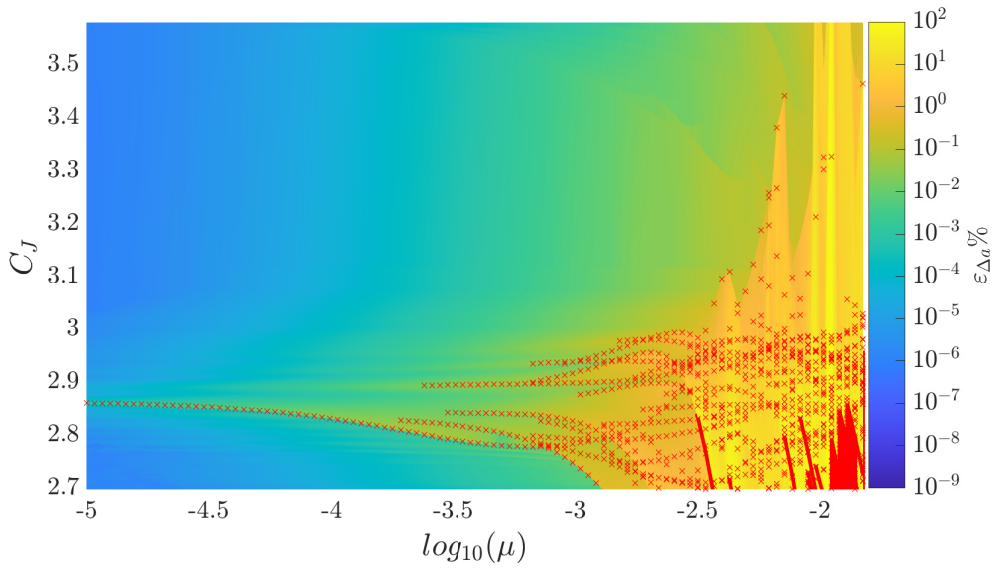

(b) $C_J - \mu - \varepsilon_{\Delta a}$ Map with SOI transitions

Figure 12: Error Map in Jacobi Constant dependence with the addition of two different features: C_{L_i} lines or 3^{rd} body SOI transitions (identified with red crosses).

This is depicted in Fig. 12a, where it is possible to recognize five lines representing the values of C_{L_i}. For each value of μ the position of the Libration points changes, and so the value of C_{L_i}. It is clear that above C_{L_1} the value of the error remains low, while below the value of C_{L_5} the error has a non-regular behavior, reaching occasionally very high values.
Trajectories with $C_J > C_{L_1}$ have low energies $\mathcal{E}$, and the particle motion is limited in the interior region of the realm (as reported in Fig. 9). The spacecraft is orbiting around the primary and is sufficiently far from the third body, so that the effect of the latter on the particle's dynamics is weak. This can be seen isolating a test case, fixing a value of μ and C_J ($> C_{L_1}$), as shown in Section 4.
In trajectories with $C_J < C_{L_5}$ the particle is able to move in the whole realm, since forbidden regions disappear, and it can reach high energies. In high energy transfers a close encounter with the third body can provokes large orbital elements variations, leading to a significant error.
In Fig. 12b the red crosses mark trajectories in which the particle reaches the third body Sphere Of Influence (SOI)whose radius is computed as [1]:

$$r_{SOI} = R_{3B} \cdot \left(\frac{\mu_2}{\mu_1}\right)^{2/5} \tag{71}$$

Almost in the whole region in which the error grows, the third body SOI is reached. Thus, a dependence of the error on the minimum relative distance that the particle and the third body experience shall be investigated, opening the discussion for another error map. A further investigation on the region in which the error increases is done, refining the grid of the simulation. The refinement is performed focusing on such low-C_J-region, and it is reported in Fig. 13.
A peak curve in pink is represented in Fig. 13. The curve follows the simulations block in which the error is larger than the other regions of the domain. Each point belonging to this line represents a simulation with different initial conditions, but isolating them one by one a correlation was found.
Taking two random initial conditions belonging to the pink line, and propagating the trajectory of the spacecraft for one orbital period, it has been found that in both cases there is a close encounter with the third body. In the case with $\mu = 10^{-2}$ (represented in Fig. 14a) the Minimum Relative Distance MRD reached between particle and third body is at $0.4 \cdot r_{SOI}$ (where r_{SOI} is the SOI radius of the third body). A similar thing happens in the case with $\mu = 10^{-4}$

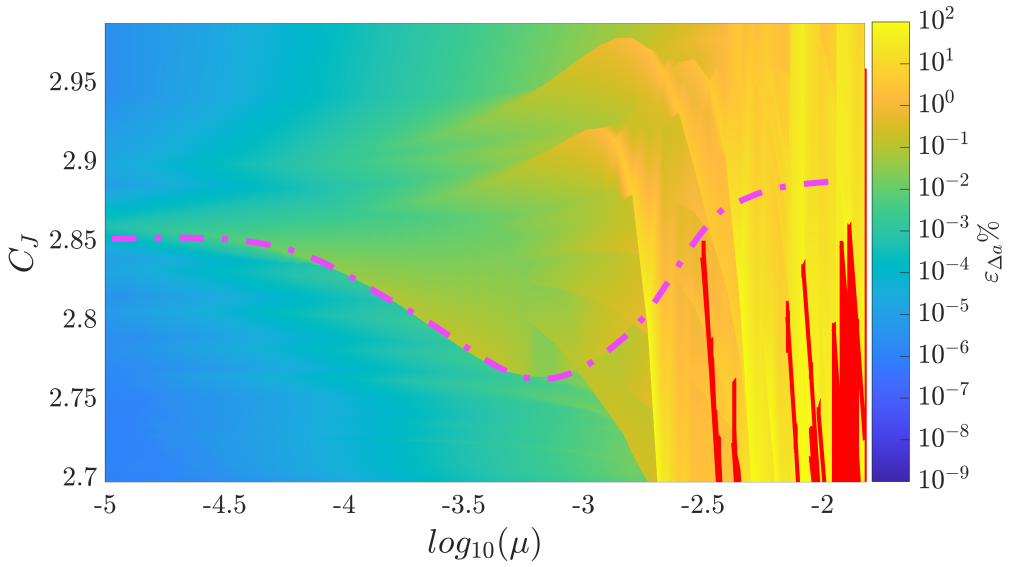

Figure 13: $C_J - \mu - \varepsilon_{\Delta a}$ Map with region in which the error increases highlighted through a pink curve.

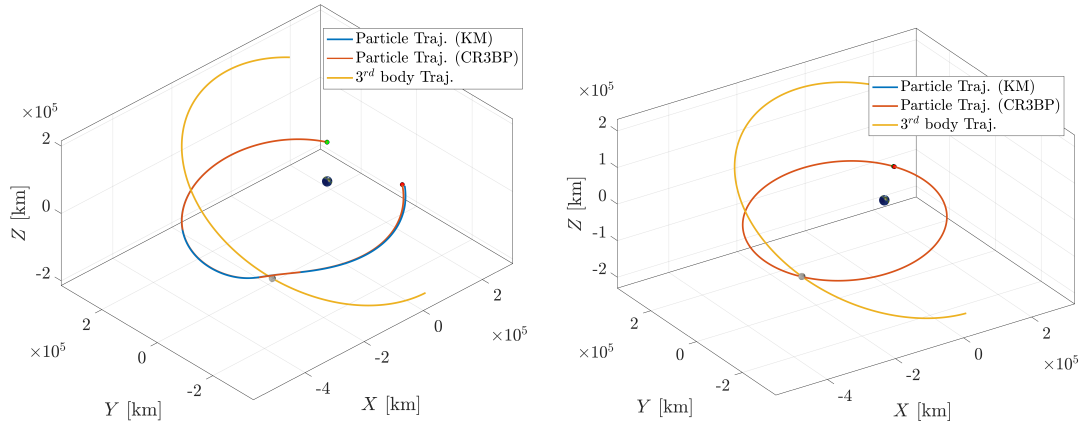

(a) $\mu = 10^{-2}$, $C_J = 2.87$, $MRD = 0.4 \cdot r_{SOI}$ **(b)** $\mu = 10^{-4}$, $C_J = 2.84$, $MRD = 5 \cdot r_{SOI}$

Figure 14: Two test trajectories belonging to the pink curve in Fig. 13. The plot contains the paths of the particle according to the CR3BP and the Keplerian Map numerical propagation, and even the trajectory traveled by the third body during the time span.

(represented in Fig. 14b), in which the MRD reached is at $5 \cdot r_{SOI}$. Even if outside the SOI of the third body, the close encounter has a considerable effect on the particle's trajectory. In the other cases that do not belong to the pink line, the close encounter happens very far from the third body, and the error is smaller.

3.1.3 Influence of the energy with respect to the third body

Before closing the discussion about the dependence on C_J, it is necessary to show another examination done on the $C_J - \mu - \varepsilon_{\Delta a}$ map. A close encounter with the third body can take place under different conditions. The best way to classify and understand the type of encounter is to look at the energy that the spacecraft has with respect to the planet, and consider the Minimum Relative Distance (MRD) reached between them. Assuming that the third body becomes the principal and only attractor, it is as modelling the encounter with the Restricted Two-Body Problem (R2BP) [1], since the effect of the main attractor is neglected when the spacecraft is closer to the third body. The mass-less particle is moving on a hyperbolic trajectory, and its energy with respect to the planet $\mathcal{E}_2$ can be computed as:

$$\mathcal{E}_2 = \frac{v^2}{2} - \frac{\mu_2}{r} \tag{72}$$

where r and v are respectively the position and the velocity of the particle with respect to the third body. μ_2 is the planetary constant of the third body. In order to obtain more readable results, the energy can be normalized with respect to the energy of the third body that moves around the main attractor on a circular orbit:

$$\mathcal{E}_{3B} = -\frac{\mu_1}{2R_{3B}} \tag{73}$$

where μ_1 is the planetary constant of the main attractor and R_{3B} the radius of the circular orbit on which the third body is orbiting around the primary. Therefore, the normalized energy used for the particle is:

$$\bar{\mathcal{E}}_2 = \left| \frac{\mathcal{E}_2}{\mathcal{E}_{3B}} \right| \tag{74}$$

Substituting the error with $\bar{\mathcal{E}}_2$ from the previous map, the $C_J - \mu - \bar{\mathcal{E}}_2$ map can be obtained, and it is represented in Fig. 15. The color-map in Fig. 15 now

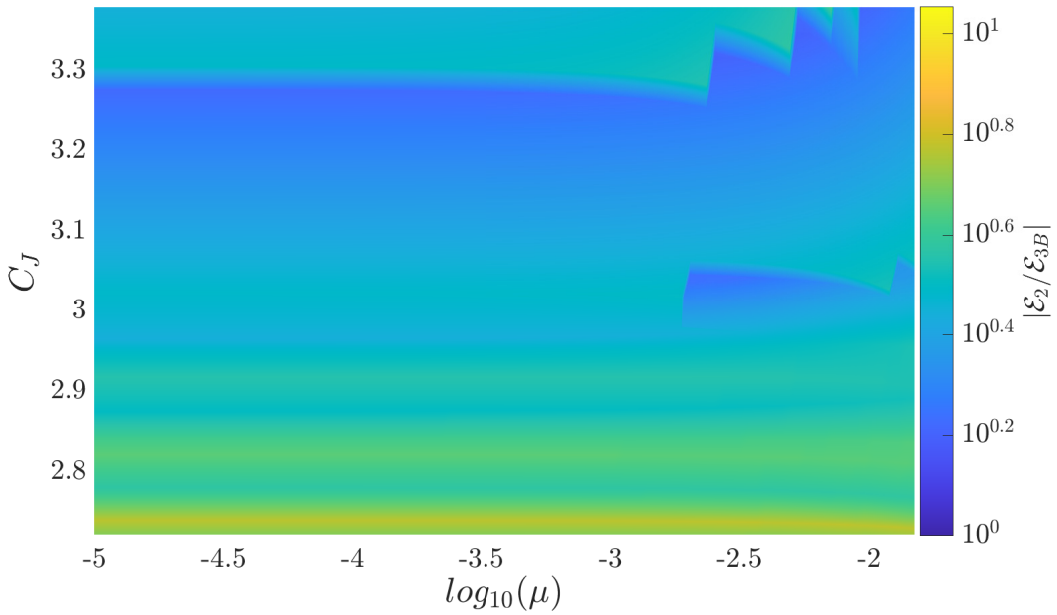

Figure 15: $C_J - \mu - \bar{\mathcal{E}}_2$ Map. Color-map representing the energy of the particle with respect to the third body, normalised to the energy of the third body with respect to the primary.

shows the $\bar{\mathcal{E}}_2$ variation. It is interesting to see that the cases in Fig. 13 in which the error was increasing, are all of them correlated to a close encounter with high energy with respect to the third body. This confirms that are not only a close encounter and a large μ that justify the large error introduced with the Keplerian Map propagation, but even the energy of the particle with respect to the third body plays a key role.

3.2 Minimum Relative Distance dependence

From the results obtained with the analysis carried out in Section 3.1 follow that the dependence upon the distance shall be investigated. The results shown highlight that in most of the cases in which the error introduced by the Keplerian Map increases, the particle trajectory passes inside or near the SOI of the third body (referring to Fig. 12b).
Adopting a similar procedure used for the $C_J - \mu - \varepsilon_{\Delta a}$ map, a massive block of simulations have been performed, this time without computing the value of the Jacobi Constant in each case but observing the Minimum Relative Distance

MRD between particle and third body reached during a period of propagation. The output is a $MRD - \mu - \varepsilon_{\Delta a}$ Map. The blocks scheme explaining the procedure to obtain the new error map is represented in Fig. 10.
The initial conditions of the particle are in line with the previous ones, with a slight change regarding the initial semi-major axis (Table 1 and Table 2).
Again, hundreds of thousands of cases have been analysed, allowing to assemble the $MRD - \mu - \varepsilon_{\Delta a}$ Map, represented in Fig. 16. The X-axis still shows the mass parameter μ, while the Y-axis now is the variation of the MRD normalized to the third body SOI (whose expression is in Eq. (71)).
The color-map still represents the percentage error as the difference between the semi-major axis variation obtained with the Keplerian Map and the CR3BP equations, as reported in Eq. (70).

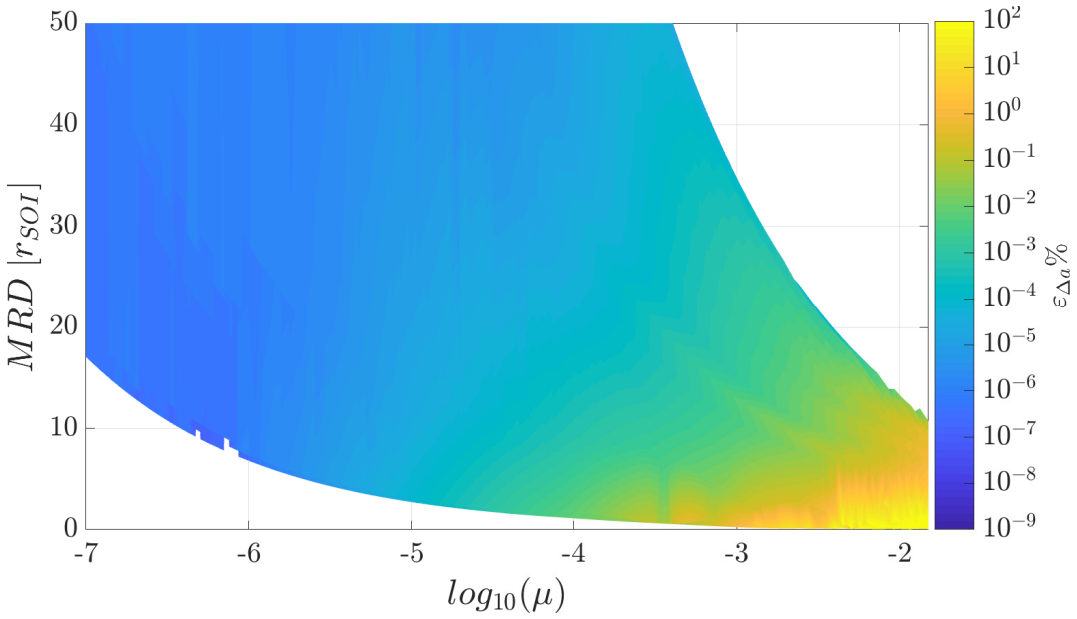

Figure 16: $MRD - \mu - \varepsilon_{\Delta a}$ Map. Y axis is containing the Minimum Relative Distance (MRD) reached by the particle with respect to the third body, normalised to its sphere of influence (Eq. (71)). Color-map representing the relative percentage error defined in Eq. (70) between CR3BP and Keplerian Map propagation.

The first characteristic that can be noticed is again the evident dependence of the error on μ.
Referring to the MRD dependence, there are few features that can be observed.

In general, the idea is that the higher the MRD, the lower is the error introduced by the Keplerian Map propagation. However, this variation is not linear. Looking at the map as a surface Fig. 17a, the error stops to decrease over a certain value of MRD. A better understanding are the vertical pink lines in Fig. 17b, that highlight that the error does not depends anymore on the MRD. This is because when the spacecraft passes very far from the third body, the orbital elements variation is low compared to the intrinsic error of the model that becomes more relevant (in coherence with what has been understood in literature [17]).
It shall be mentioned that for very distant passages from the 3^{rd} body, the effect of the latter on the particle's motion can be seen as just a small perturbation. In these cases, it is more useful to adopt another method to predict the orbital elements variation, as the averaged technique explained in Section 2.1.2 which is fully-analytical, and the numerical integration of the Keplerian Map is excessive.
For very low encounters instead the orbital elements variation is large, and the error increases. This is again due to the fact that the orbital elements of the Keplerian Map are fictitiously defined with respect to the barycentre of the system, while their variation follows the primary's movement.
Following these considerations, it can be understood that in reality the optimal range in which the Keplerian Map theory shall be applied is situated in the middle: neither for very far encounters (large MRD), nor for very close encounters (small MRD).
It is inappropriate to set the lower limit to exactly the sphere of influence of the third body, since:

- The meaning of the SOI loses sense when the mass parameter of the system is very large (as in the Earth-Moon system). The effect of the secondary remains significant even outside from its SOI if its mass is large, and neglecting this would lead to wrong results.

- From the results obtained the error is significant even outside from the third body SOI, reaching large values even up to 10 times the SOI for high values of μ.

For low values of μ the dependence by the MRD can be neglected, and the only analysis that can be done is the one regarding the energy of the particle (explained in Section 3.1. These considerations conclude the analysis of the $MRD - \mu - \varepsilon_{\Delta a}$ Map.

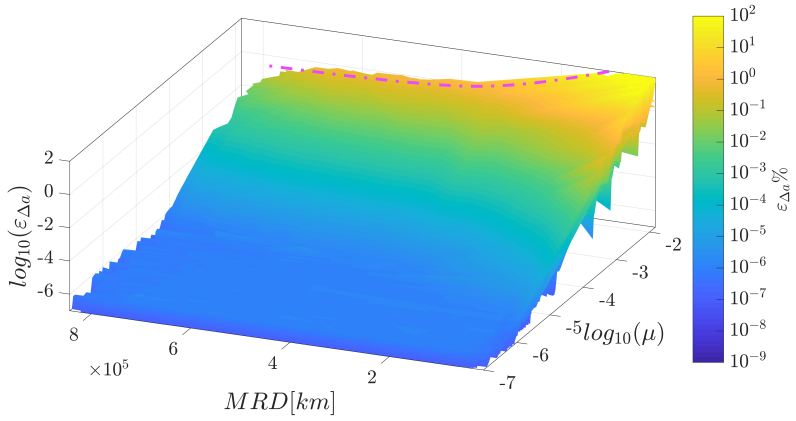

(a) 3D surface of $MRD - \mu - \varepsilon_{\Delta a}$ Map

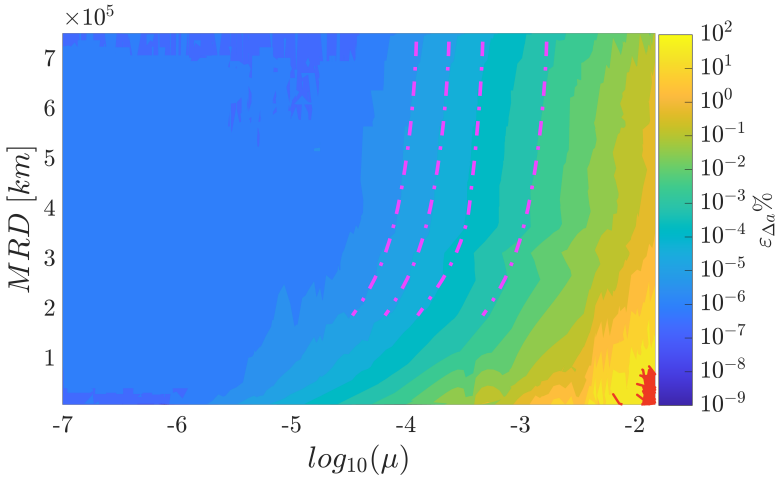

(b) Level curves of $MRD - \mu - \varepsilon_{\Delta a}$ Map

Figure 17: 3D surface and level curves of the $MRD - \mu - \varepsilon_{\Delta a}$ Map represented in Fig. 16. Pink lines highlighting the behavior of the error with the increasing of the MRD. Now the MRD is not normalised to obtain a better visibility of the feature.

3.3 Results and considerations

The error introduced by the Keplerian Map - based propagation has been analysed in Section 3.1 and Section 3.2, searching for a dependence on the Jacobi Constant of the particle and on the Minimum Relative Distance reached between third body and spacecraft. This part is devoted to summarise the results obtained and to fix a suitable domain of application where the model

can be used.

3.3.1 Comparison with Patched Conics approach

To emphasize even more the effectiveness of the Keplerian Map theory, the same error maps that were shown in the previous discussions can be re-computed comparing the CR3BP solution with a different model. To highlight the non-negligible effect of the third body presence in the system, it can be useful to compare the results to those obtained when using the Patched Conics approach [1].
The Patched Conics modelling is an extension of the Two Body Problem, in which the trajectory of the spacecraft is divided in different arcs. In each arc the R2BP model is adopted, neglecting the effect of a secondary attractor. When the spacecraft enters inside the Sphere Of Influence of another celestial body, this becomes the main attractor. In the case of the Sun-Earth system, this concept is applied as in the following example:

1. The particle is orbiting around the Sun and it is far from the Earth. The model used for the system is the R2BP with the Sun as attractor. To predict the whole trajectory, the equations of the R2BP can be numerically integrated [1].

2. If the particle reaches the SOI of the Earth, the integration is stopped and the model is switched to a R2BP where the main attractor is the Earth.

3. The hyperbolic trajectory with respect to the Earth is propagated until the limit of the Earth's SOI is reached again. At this point there is another switch of the model to a R2BP with the Sun as attractor.

In the case in which the SOI of the third body is never reached, the motion is fully modelled with a R2BP with a single main attractor, neglecting completely the presence of another celestial body.
Using this scheme, it is possible to reconstruct an error map similar to those in Section 3.1 and Section 3.2, this time adopting the percentage error defined as:

$$\varepsilon_{\Delta a}^{PC} = \left| \frac{\Delta a^{CR3BP} - \Delta a^{PC}}{\Delta a^{CR3BP} + 1} \right| \cdot 100 \tag{75}$$

in which Δa^{PC} represents the semi-major axis variation using the Patched Conics modeling. If the third body's SOI is never reached, then $\Delta a^{PC} = 0$ and

the relative error is maximum.
Therefore, following the same blocks scheme of Fig. 10, but using the Patched Conics approach instead of the Keplerian Map theory, the error maps in Fig. 18 and Fig. 19 are obtained.

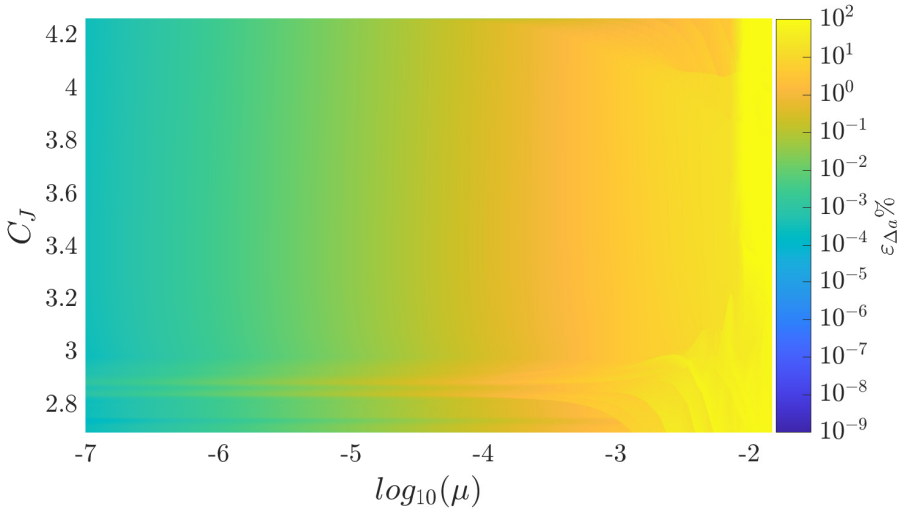

Figure 18: $C_J - \mu - \varepsilon_{\Delta a}$ Map comparing CR3BP and Patched Conics approach. Color-map showing the error defined in Eq. (75). Set of initial conditions of Table 1 and Table 2.

The error maps obtained with the Patched Conics modeling instead of the use of the Keplerian Map has significant higher errors. As can be seen in Fig. 18, the region in which the error is larger for high energies is still present, but now in general the error does not fall below 10^{-3} %. The same can be seen in Fig. 19. With the increasing of the mass parameter μ, the influence of the third body on the particle motion becomes more relevant. Consequently, the two-body problem approximation can not be considered applicable anymore. Thanks to the results shown, it can be stated that there are no cases in which the Patched Conics approach can be used instead of the propagation of Keplerian Map.

3.3.2 Error threshold as criterion for the Keplerian map applicability

From the error maps shown in Section 3.1 and Section 3.2 it is not easy to define a domain of application for the Keplerian Map theory. As expected, the

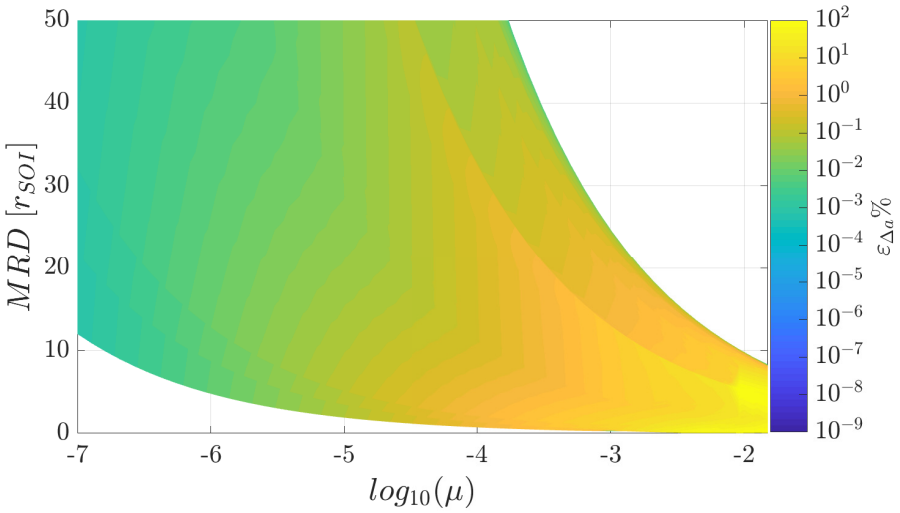

Figure 19: $MRD - \mu - \varepsilon_{\Delta a}$ Map comparing CR3BP and Patched Conics approach. Color-map showing the error defined in Eq. (75). Set of initial conditions of Table 1 and Table 2. MRD normalised to the third body sphere of influence radius (Eq. (71)).

dependence on some system parameters have been found, but none of them allow to define a sharp applicability region. The correctness of the motion propagation with Keplerian Map has been measured with the percentage error of Eq. (70). By imposing a threshold on the error, it is possible to separate the error maps in two different regions, identifying when the Keplerian Map can be applied.
A limit that can be imposed is a percentage error of:

$$\varepsilon_{\Delta a}^{lim} = 10^{-3}\,\% \tag{76}$$

such that:

$$\text{If: } \begin{cases} \varepsilon_{\Delta a} \geqslant 10^{-3}\,\% \rightarrow \text{The Keplerian Map is not applied} \\ \varepsilon_{\Delta a} < 10^{-3}\,\% \rightarrow \text{The Keplerian Map is applied} \end{cases} \tag{77}$$

The error maps on C_J and MRD can be re-printed as a binary plot showing the whole applicability domain of the Keplerian Map as the region in which the error is below $10^{-3}\,\%$.
The binary error maps are shown in Fig. 20 and Fig. 21. The one in $C_J - \mu - \varepsilon$ (Fig. 20) can be exploited with the following reasoning: before starting the

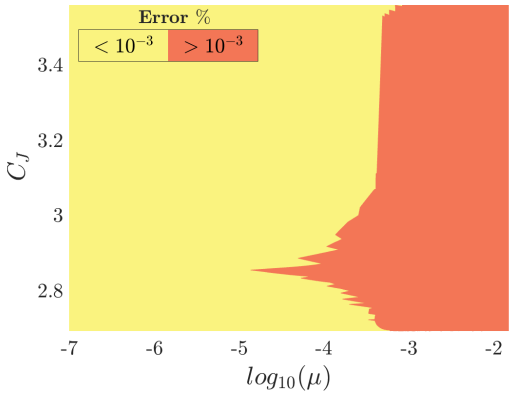

Figure 20: Binary $C_J - \mu - \varepsilon_{\Delta a}$ Map. Color-map showing acceptable and non-acceptable cases according to the error limit of Eq. (76). Same building procedure of the map in Fig. 11.

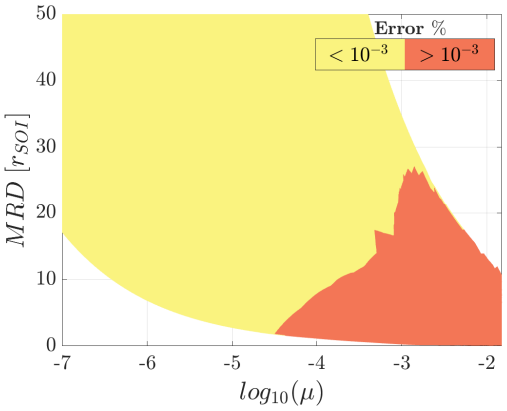

Figure 21: Binary $MRD - \mu - \varepsilon_{\Delta a}$ Map. Color-map showing acceptable and non-acceptable cases according to the error limit of Eq. (76). Same building procedure of the map in Fig. 16.

propagation, the user can compute the Jacobi constant of the system and the mass parameter of the system. Then, the user enters in the map and see if the error is expected to be large or not. If the error expected is acceptable, the user can propagate the motion with the Keplerian Map theory.
Referring to the $MRD - \mu - \varepsilon$ map, it is sufficient to compute the MRD reached to predict the error introduced with the Keplerian Map propagation. If the MRD can be predicted without the numerical propagation of the R3BP equations (possible methods explained in Section 3.3.3), then it is possible to enter in a pre-built map as the one of Fig. 21 and look at the expected error, evaluating whether or not to apply the Keplerian Map. This procedure can be time-saving, especially in optimisation processes, since it avoids the numerical integration of the R3BP equations
It is important to remember that also the map itself has a dependence on the initial conditions of the system. Indeed, as shown in Table 1 and Table 2, the maps created does not cover all the possible initial conditions of the problem, but they are built only for a set of cases.
However, reproducing the maps for other blocks of initial conditions, the morphology of the map remains the same:

- In the $C_J - \mu - \varepsilon$ map there is always the region in which the error increases, and it is always for $C_J < C_{L_5}$. For $C_J > C_{L_1}$ the error has

always a linear dependence on μ as observed.

- In the $MRD-\mu-\varepsilon$ map there is always the optimal region of applicability is in the middle. Indeed, for low MRD the error is always growing, and for high MRD the error stops to decrease.

3.3.3 Minimum Relative Distance prediction

As aforementioned in Section 3.3.2, if it is possible to predict the MRD reached between the particle and the third body, then it is possible to enter in the binary plot of Fig. 21 and to know a priori if the Keplerian Map theory can be applied (if the map settings cover the current initial conditions).
In the context of the CR3BP, Öpik's theory ([19],[20],[21]) is a fully analytical theory used to approximates a close encounter of a spacecraft with the third body. In an extension of the theory developed by Valsecchi [19], it is demonstrated how to analytically predict the Minimum Orbit Intersection Distance (MOID) between particle and third body. The MOID is defined as the minimum distance reached between the osculating orbits of the particle and the third body. Therefore, the MOID does not corresponds to the MRD in most of the times, but can be used as preliminary data to identify the problem.
Other studies [17] developed an almost fully-analytical procedure that allows to predict when the encounter will happen by assuming that the motion of the particle is unperturbed until the closest approach with the third body.
Even if this seems a huge approximation, it is demonstrated that the MRD is predicted with sufficient accuracy so that this method might be used as a preliminary tool.
This procedure is developed for the general R3BP, and it is explained in the following. The maps presented are all built in the case of the CR3BP, since decreasing the complexity of the model can allow to understand better its core properties.
In the case of the CR3BP the position of the third body can be expressed in function of the particle orbital elements (thanks to the relation in Eq. (47)). Therefore, the distance between particle and third body can be expressed in function of the only true anomaly ν and the minimum can be easily computed.
In the general case of the R3BP, the distance between the spacecraft and the third body can be obtained from their position vectors in the inertial frame

with respect to the barycentre of the system:

$$\begin{aligned}\mathbf{r} &= R_3(\Omega)\,R_1(i)\,R_3(\omega+\nu)\begin{bmatrix}\dfrac{a(1-e^2)}{1+e\cos\nu} & 0 & 0\end{bmatrix}^T\\ \mathbf{r_{3B}} &= R_3(\Omega_{3B})\,R_1(i_{3B})\,R_3(\omega_{3B}+\theta_{3B})\begin{bmatrix}\dfrac{a_{3B}(1-e_{3B}^2)}{1+e\cos\theta_{3B}} & 0 & 0\end{bmatrix}^T\end{aligned} \tag{78}$$

such that:

$$\mathbf{\Delta r} = \mathbf{r} - \mathbf{r_{3B}} \;\rightarrow\; \Delta r = \Delta r(\nu,\theta_{3B}) = ||\mathbf{r} - \mathbf{r_{3B}}|| \tag{79}$$

To minimise Δr its total derivative with respect to the particle true anomaly shall be computed [17]:

$$\frac{d\Delta r}{d\nu} = \frac{\partial \Delta r}{\partial \nu} + \frac{\partial \Delta r}{\partial \theta_{3B}}\frac{\partial \theta_{3B}}{\partial \nu} = \frac{\partial \Delta r}{\partial \nu} + \frac{\partial \Delta r}{\partial \theta_{3B}}\frac{\partial \theta_{3B}}{\partial E_{3B}}\frac{\partial E_{3B}}{\partial M_{3B}}\frac{\partial M_{3B}}{\partial E}\frac{\partial E}{\partial \nu} \tag{80}$$

where E is the eccentric anomaly of the particle, M_{3B} and E_{3B} are respectively the mean anomaly and the eccentric anomaly of the third body. The partial derivatives in the second term of Eq. (80) are computed as:

$$\begin{aligned}\frac{\partial \theta_{3B}}{\partial E_{3B}} &= \frac{1+e_{3B}\cos\theta_{3B}}{\sqrt{1-e_{3B}^2}}\\ \frac{\partial E_{3B}}{\partial M_{3B}} &= \frac{1+e_{3B}\cos\theta_{3B}}{1-e_{3B}^2}\\ \frac{\partial M_{3B}}{\partial E} &= \left(\frac{a}{a_{3B}}\right)^{3/2}\frac{1-e^2}{1+e\cos\nu}\\ \frac{\partial E}{\partial \nu} &= \frac{\sqrt{1-e^2}}{1+e\cos\nu}\end{aligned} \tag{81}$$

Indeed, as stated in Eq. (80), there is not the possibility to express θ_{3B} as function of ν, but their derivatives can be related as in Eq. (80).
Setting Eq. (80) equal to zero, it is possible to compute the particle true anomaly at the maximum and the minimum relative distances. Taking the minimum of Δr, the true anomaly of the particle ν^{MRD} at the closest approach with the third body can be obtained. However, this requires to solve

the equation numerically, since it is implicit. Moreover, it has not a single solution, but the ν^{MRD} can be found choosing a proper set of initial conditions $\nu_0^{MRD} \in [0\ ,\ 2\pi]$ and taking the lowest solution.
This tool can be used to approximate the closest approach distance that is reached in one particle orbital period. Knowing the MRD, the mass parameter μ and the initial conditions of the particle, it is possible to enter in the $MRD - \mu - \varepsilon_{\Delta a}$ map and predict the error introduced by the Keplerian Map propagation.

3.3.4 Other error maps

To conclude the results and considerations part, it is important to mention that other error dependencies were analysed. In addition to the error maps presented in Section 3.1 and Section 3.2, the behavior of the error introduced with the Keplerian Map theory were studied in function of other parameters: the Tisserand parameter ($\varepsilon_{\Delta a}(\mathcal{T})$), the initial phasing angle between the particle and the third body ($\varepsilon_{\Delta a}(\gamma_0)$) and the resonance ratio between particle and third body periods ($\varepsilon_{\Delta a}(a/a_{3B})$).
The error maps in those parameters were not studied in deep as the ones in the current work, but they were suggesting that in reality the error has no dependencies on such parameters. On the other hand, as mentioned in Section 7, a further analysis on these parameters might be needed to understand a more refined limit for the Keplerian Map domain. These are the reasons for which only the analysis done on the C_J and MRD are reported in this work.

CHAPTER 4

Model validation

A set of possible limits for the Keplerian Map utilisation have been defined in Section 3. The analysis have been carried in the CR3BP context, since it is an approximated model that allows to exploit some particular system properties (as the Jacobi Integral conservation).
In the current chapter the intent is to remain in the field of the $C3BP$, applying the model developed showing the applicability of the Keplerian Map theory in trajectories prediction for real systems as Earth-Moon and Jupiter-Europa.
The only goal now is to show that propagating the motion of a particle with the Keplerian Map is not always possible, since, under some conditions, it introduces a significant error in the orbital elements prediction. Instead, a real design of trajectory will be carried in Section 6.
Before presenting the examples studied as validation of the model, it can be useful to recap the main results found in Section 3:

- The propagation through the Keplerian Map shall be avoided for high mass parameters μ. In particular, for $\mu > 10^{-4}$ the percentage error introduced is larger than the defined threshold limit $\varepsilon_{\Delta a}^{lim} = 10^{-3}\%$.

- The propagation through the Keplerian Map shall be avoided when the energy of the particle in the Synodic frame is high (meaning a low Jacobi Constant) in systems with high μ. In particular, for $C_J > C_{L_1}$ the error is low for low values of μ, and the model can be used.

- The propagation through the Keplerian Map shall be avoided for systems with high mass parameters and when the particle flies close to the third body. The error introduced in the prediction reaches prohibitive values when the MRD is small, and μ is high.

Then, the procedure that can be adopted to predict the particle motion through the Keplerian Map is the following:

1. A set of prepared error maps including hundreds of thousands of initial conditions shall be available. It is sufficient that the error maps are in their binary version (as in Fig. 20 and Fig. 21).

2. From the knowledge of the initial conditions (orbital elements of the particle, of the third body and mass parameter of the system) it is possible to compute the Jacobi Constant and enter in the $C_J - \mu - \varepsilon_{\Delta a}$ error map, looking at the expected error.

3. With the procedure explained in Section 3.3.3 an approximation of the closest approach distance can be computed, allowing to enter even in the $MRD - \mu - \varepsilon_{\Delta a}$ error map and see the expected error.

4. If in both cases the value of the expected error is small, than it is possible to propagate the motion of the particle with the Keplerian Map, as explained in Section 2.2.

By adopting this procedure, three examples of possible applications are presented in the following.

4.1 Earth - Moon system

Two different examples in the Earth-Moon system are presented, showing the error in the prediction of the orbital elements evolution. The mass parameter of the system is [27]:

$$\mu_{\oplus-\leftmoon} = 1.2151 \cdot 10^{-2} \tag{82}$$

From the error map in Fig. 12a it has been shown that carefulness shall be adopted if the energy of the particle in the Synodic frame (expression in Eq. (60)) is high (low C_J), while the error remains contained for high values of C_J (low energies). This is what is demonstrated with the following examples.

4.1.1 Trajectory with high energy

The first application that is presented concerns the motion of a spacecraft in the Earth-Moon system, with a Jacobi Constant C_J that is lower than the value of C_{L_1}.
The initial conditions of the particle are listed in Table 4. The initial semi-major axis of the particle is $a_0 = 0.67 \cdot R_{3B}$. By computing the initial position

in the dimensionless Synodic reference frame (with the procedure shown in Section 3.1.1), it is possible to compute the value of the Jacobi Constant of the particle:

$$C_J = 3.015668 \tag{83}$$

The initial conditions for the Moon are listed in Table 5. They are taken from

Table 4: Initial conditions of the particle in the Earth - Moon system (trajectory with $C_J < C_{L_1}$).

Orbital Element	Initial Value
a_0 [km]	257837.67
e_0 [-]	0.50
i_0 [deg]	10.00
Ω_0 [deg]	345.00
ω_0 [deg]	25.00
ν_0 [deg]	310.00

NASA Horizons system [28], but the eccentricity of the Moon is set to zero since now the examples are with the CR3BP assumption.

Table 5: Initial conditions of the Moon used in the Earth - Moon system examples. Orbital elements of 30/10/2021 from NASA Horizons [28] but CR3BP case ($e_0 = 0$).

Orbital Element	Initial Value
a_{3B_0} [km]	384832.34
i_{3B_0} [deg]	26.38
Ω_{3B_0} [deg]	10.39
ω_{3B_0} [deg]	236.22
ν_{3B_0} [deg]	254.51

From the definition of the system, it is possible to compute the Jacobi Constant in the Libration points, as shown in Table 6. From the value of the particle's Jacobi Constant (in Eq. (83), it is clear that the particle is orbiting with $C_{L_2} > C_J > C_{L_3}$. In this realm the particle is orbiting with an energy just above $\mathcal{E}_{L_2}$: the trajectory passes in the vicinity of m_1 and m_2 and the exterior realm via a neck around L_2 (as represented in Fig. 9) [3].

Table 6: Jacobi Constant values in the Libration points of the Earth - Moon system in the dimensionless Synodic reference frame.

C_{L_1}	C_{L_2}	C_{L_3}	$C_{L_4} = C_{L_5}$
3.172160	3.188341	3.012147	2.987997

Another thing that can be predicted with the knowledge of the initial conditions of the system, is the MRD reached by the particle with respect to the third body during a period of revolution. This is done with the approximated procedure explained in Section 3.3.3 and then compared to what in reality happens propagating the CR3BP equations:

$$\begin{aligned} &\text{From CR3BP propagation:} && MRD = 2.87 \cdot r_{SOI} \\ &\text{From approximated procedure:} && MRD = 3.45 \cdot r_{SOI} \end{aligned} \tag{84}$$

A relative error in the approximation of the MRD of the 20.21 % is computed from Eq. (84). As expected, the approximated procedure does not allow to obtain an accurate prediction in this case. This is due to the large orbital elements variation that the particle experiences, due to the high mass parameters. With the initial conditions, the knowledge of μ, C_J and MRD, it is possible to enter in the error maps (of Fig. 11 and Fig. 16) and to predict the value of $\varepsilon_{\Delta a}$. The error in the semi-major axis variation will be certainly large since the mass parameter $\mu_{\oplus-\leftmoon}$ is the largest of the Solar System, and furthermore since $C_J < C_{L_1}$ the prediction is expected to give almost completely different results from the ones of the CR3BP.
The motion of the particle for one orbital period is represented in Fig. 22a and Fig. 22b in the Inertial and Synodic reference frames, respectively.
The comparison between CR3BP and Keplerian Map solutions shown that the error $\varepsilon_{\Delta a}$ (computed as in Eq. (70)) is:

$$\varepsilon_{\Delta a} = 16.88\,\% \tag{85}$$

It is worth highlighting that the error is referred to just one orbital period propagation. In real applications there is the need to predict the error for several periods, and this causes the error to grow significantly.
The low accuracy of the propagation through the Keplerian Map can be noticed also looking at the orbital elements evolution with time, that are shown in Fig. 23.

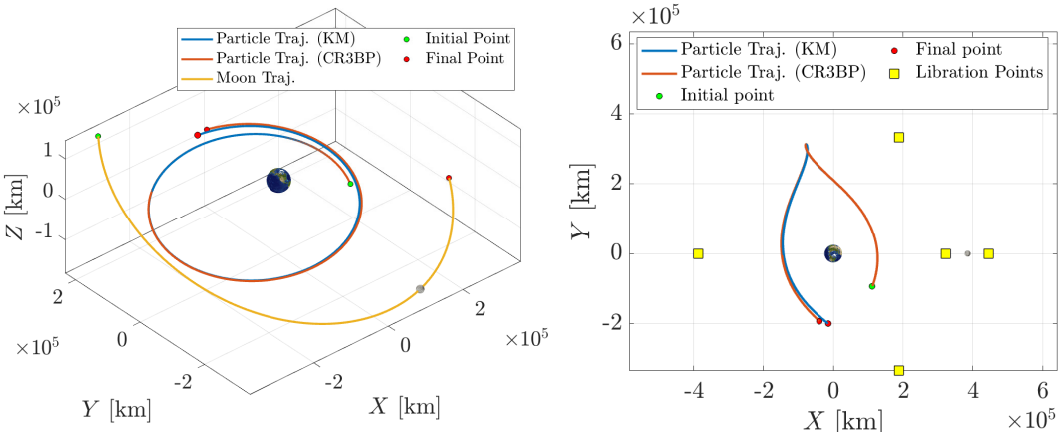

(a) Inertial Barycentric reference frame

(b) Synodic reference frame

Figure 22: Trajectory of the particle with initial conditions in Table 4, propagated with CR3BP and Keplerian Map, represented in the Inertial Barycentric and Synodic reference frames.

This example confirmed that in the Earth-Moon system, especially in high energy cases, the particle's motion can not be propagated with the Keplerian Map, since the error introduced is not negligible. Worst predictions can be obtained decreasing further the MRD and the C_J values.

4.1.2 Trajectory with low energy

As previously mentioned, the initial conditions are now modified in order to validate the model in a different energy regime.
The new initial conditions of the particle are listed in Table 7. The initial conditions of the Moon are instad unchanged. Now the initial semi-major axis of the particle is $a_0 = 0.4 \cdot R_{3B}$. With the new initial conditions, the value of the Jacobi Constant of the particle is:

$$C_J = 3.749205 \tag{86}$$

Now the particle is orbiting with $C_J > C_{L_1}$. This means that the particle cannot move between the realms around m_1 and m_2 [3].
As done in the previous example, the value of the MRD is computed and

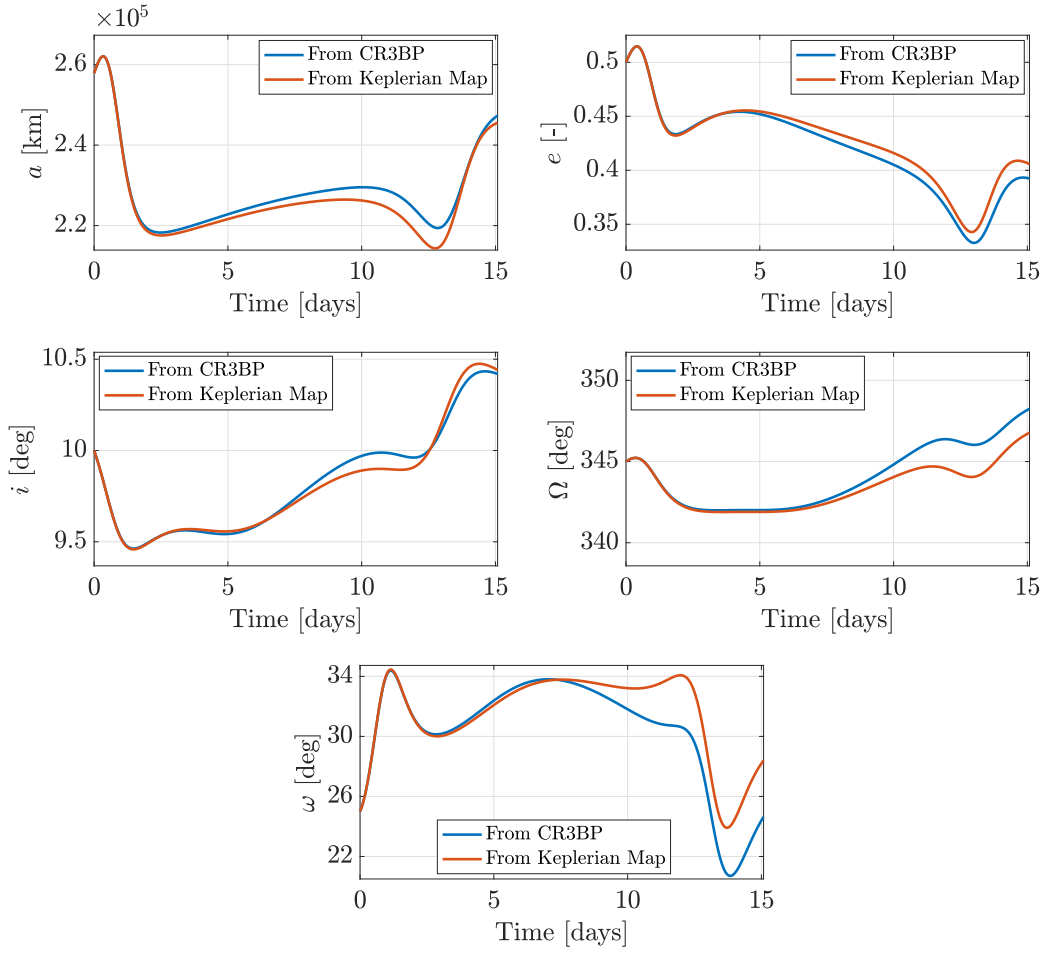

Figure 23: Orbital elements evolution(referred to the case of Section 4.1.1). Comparison of numerical propagation through CR3BP and Keplerian Map.

compared with the real one:

$$\begin{aligned} &\text{From CR3BP propagation:} && MRD = 2.82 \cdot r_{SOI} \\ &\text{From approximated procedure:} && MRD = 2.38 \cdot r_{SOI} \end{aligned} \tag{87}$$

In this case the relative percentage error in the MRD prediction is 15.61%. This is a better approximation than the one previously examined, but the error is still not negligible.
Now $\varepsilon_{\Delta a}$ is expected to be smaller, but still not acceptable for the set threshold of 10^{-3} %. Propagating the motion of the particle for one orbital period with

Table 7: Initial conditions of the particle in the Earth - Moon system (trajectory with $C_J > C_{L_1}$).

Orbital Element	Initial Value
a_0 [km]	153932.93
e_0 [-]	0.50
i_0 [deg]	10.00
Ω_0 [deg]	345.00
ω_0 [deg]	25.00
ν_0 [deg]	10.00

the CR3BP equations and with the Keplerian Map, the resulting error on the semi-major axis variation at the end is:

$$\varepsilon_{\Delta a} = 5.39\,\% \tag{88}$$

It is significantly smaller than the one for high energy trajectories, but as predicted, it remains unacceptable.
The motion of the particle for one orbital period is represented in Fig. 24a and Fig. 24b in the Inertial and Synodic reference frames, respectively. It is evident that now the orbit is far from the Moon, and even if the MRD is not so distant from the Moon SOI, the prediction of the motion is computed with good accuracy with respect to before.
The variation of the particle orbital elements is shown in Fig. 25. As can be seen, they do not experience a large variation during an orbital period, following an error not excessively large.
This example demonstrates that in cases of low energy trajectories, the motion of the particle propagated with the Keplerian Map has an improvement, but confirms that the Earth-Moon case remains out of the limits.

4.2 Jupiter - Europa system

In this section the last example as model validation is presented, showing that in systems with relatively small mass parameter, the propagation of the particle's motion with the Keplerian Map is more accurate than in the examples in Section 4.1.
In particular, we move to the Jupiter - Europa system, in which the mass

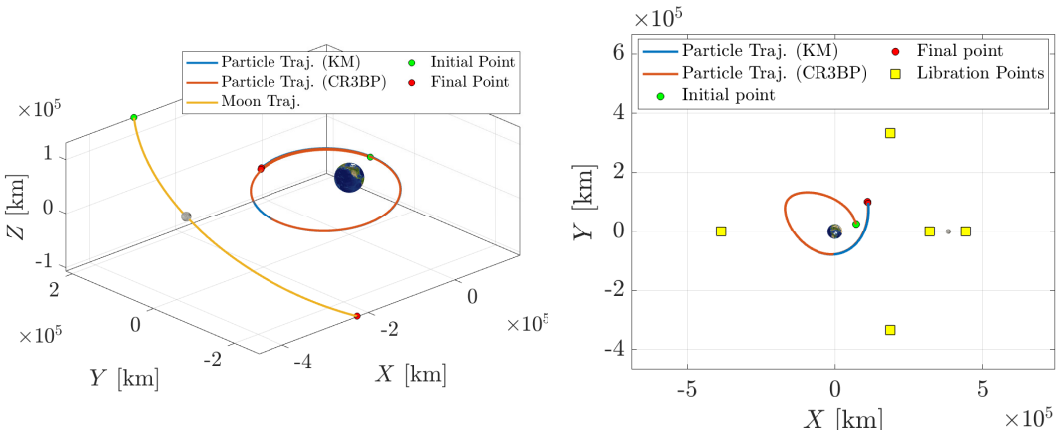

(a) Inertial Barycentric reference frame **(b)** Synodic reference frame

Figure 24: Trajectory of the particle with initial conditions in Table 7, propagated with CR3BP and Keplerian Map, represented in the Inertial Barycentric and Synodic reference frames.

parameter is:

$$\mu_{\mathcal{Y}-E} = 2.5165 \cdot 10^{-5} \tag{89}$$

Since the value of μ is low, it is expected that the motion propagation with the Keplerian Map is almost coincident with the solution of the CR3BP equations. The initial conditions of Europa are taken from the NASA Horizons system [28] at epoch 30/10/2021, and are listed in Table 8.

Table 8: Initial conditions of Europa used in the Jupiter - Europa system example. Orbital elements of 30/10/2021 from NASA Horizons [28] but CR3BP case ($e_0 = 0$).

Orbital Element	Initial Value
a_{3B_0} [km]	671302.58
i_{3B_0} [deg]	2.52
Ω_{3B_0} [deg]	329.36
ω_{3B_0} [deg]	122.42
ν_{3B_0} [deg]	1.32

The initial conditions of the particle are written in Table 9 (the value of the initial semi-major axis is $a_0 = 1.05 \cdot R_{3B}$). From them, it is possible to compute

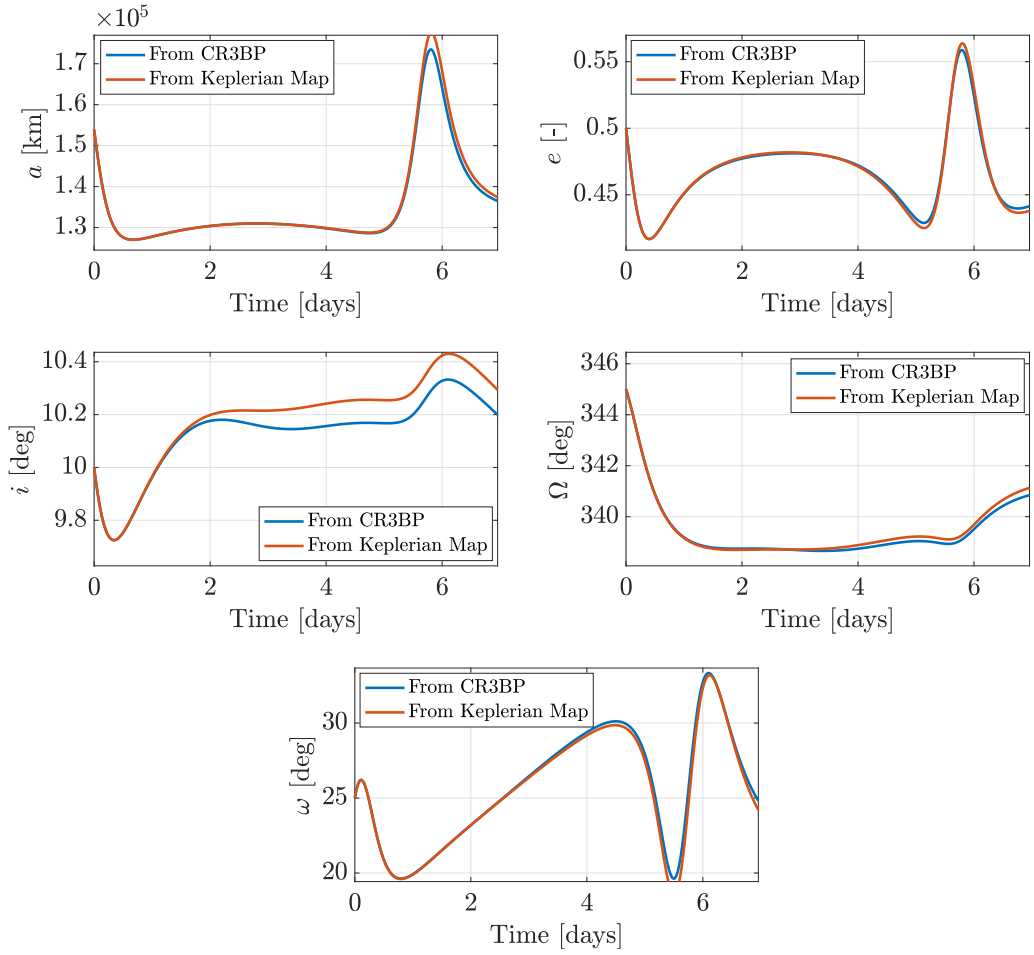

Figure 25: Orbital elements evolution (referred to the case of Section 4.1.2). Comparison of numerical propagation through CR3BP and Keplerian Map.

that:

$$C_J = 2.700158 \tag{90}$$

which is lower than the value of C_{L_5}. This means that the spacecraft has an high energy allowing it to move in the whole realm.
The MRD prediction during one period can be done as in the other examples, through the procedure of Section 3.3.3. The results shows that:

$$\begin{aligned} &\text{From CR3BP propagation:} && MRD = 6.58 \cdot r_{SOI} \\ &\text{From approximated procedure:} && MRD = 6.60 \cdot r_{SOI} \end{aligned} \tag{91}$$

Table 9: Initial conditions of the particle in the Jupiter-Europa system.

Orbital Element	Initial Value
a_0 [km]	704867.70
e_0 [-]	0.50
i_0 [deg]	10.00
Ω_0 [deg]	345.00
ω_0 [deg]	25.00
ν_0 [deg]	72

Thus, the error on the MRD prediction is of the 0.3 %, confirming that the used procedure gives sufficiently accurate results when μ is small.
From the propagation for one orbital period with the CR3BP and with the Keplerian Map, the resulting error is:

$$\varepsilon_{\Delta a} = 1.2 \cdot 10^{-5} \,\% \tag{92}$$

Which is below the threshold of 10^{-3} %, thus the Keplerian Map can be used in this case, granting almost perfect results.
The trajectory of the spacecraft in the Inertial Barycentric reference frame is depicted in Fig. 26. As it can be observed, the motion obtained with the Keplerian Map is basically coincident with the one coming from the CR3BP equations.
The accuracy of the results can be appreciated also in the plot of the orbital elements evolution of the particle, that are represented in Fig. 27. This brief example demonstrated that when dealing with systems with low mass parameter, the Keplerian Map theory can be applied obtaining very accurate results.

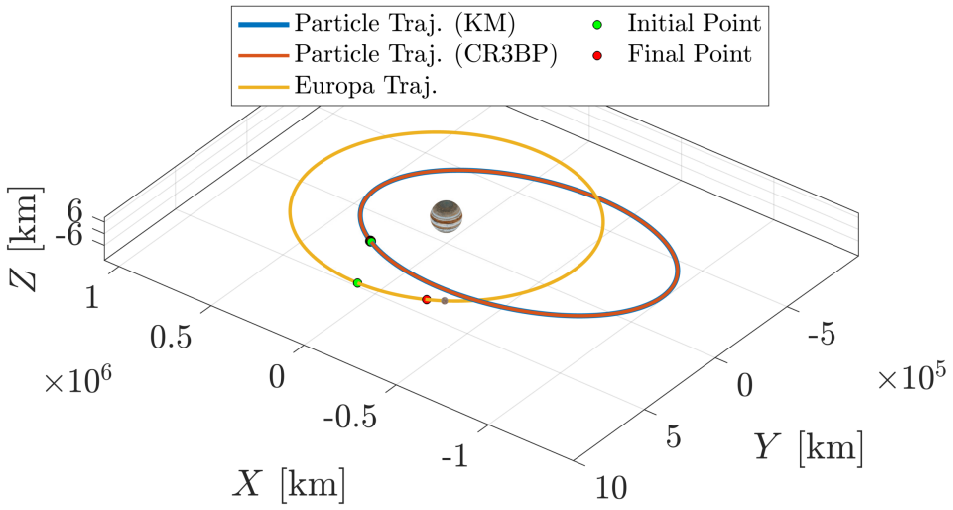

Figure 26: Trajectory of the particle in Inertial Barycentric reference frame of Jupiter-Europa system (initial conditions in Table 9). Comparison between numerical propagation through CR3BP or Keplerian Map (the prediction almost exact).

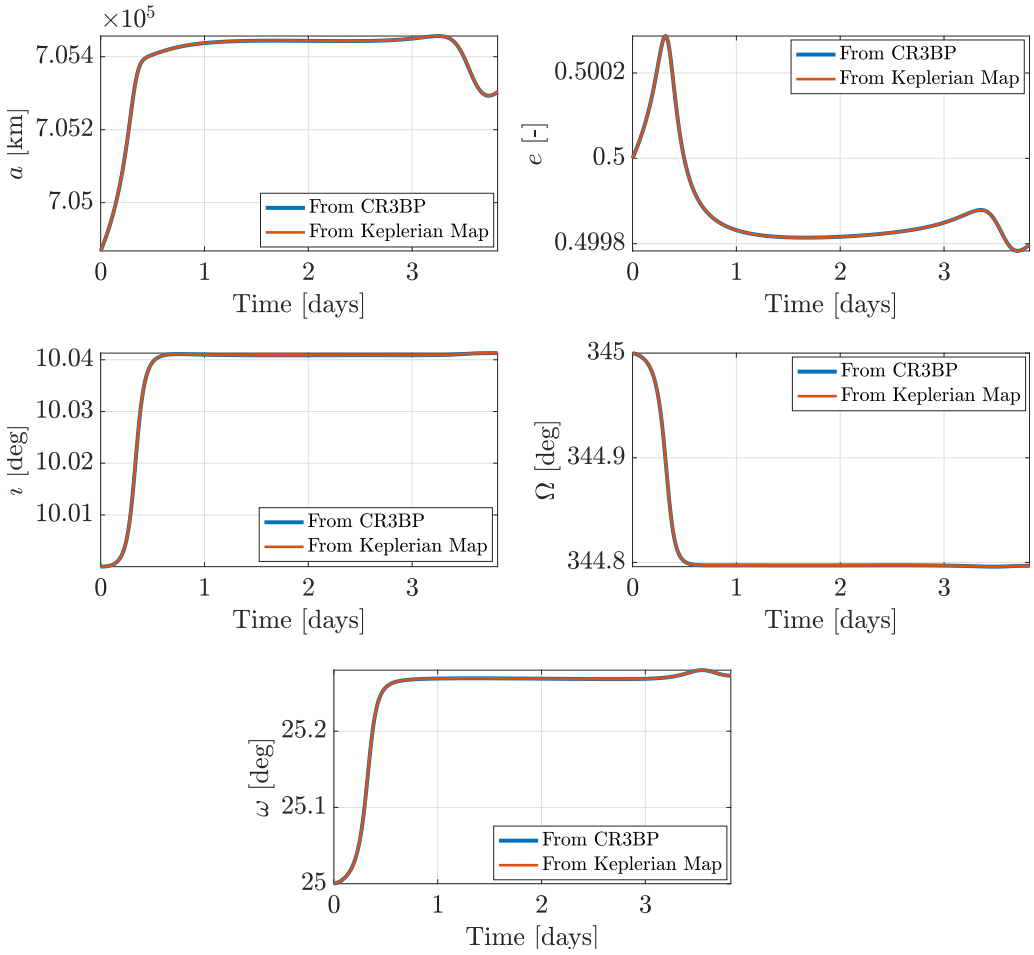

Figure 27: Orbital elements evolution (referred to the Jupiter-Europa example). Comparison of numerical propagation through CR3BP and Keplerian Map (the prediction is almost exact).

CHAPTER 5

Lagrange's Planetary Equations in hyperbolic form

THE analysis done on the limits of the Keplerian Map theory has confirmed that the model cannot be always applied to predict the motion of the spacecraft. In the cases identified in Section 3, there is the necessity to adopt another approach to apporximate the solution of the three-body problem.
With the aim of doing that, a possible alternative is the numerical integration of the Lagrange's Planetary Equations in their hyperbolic form. In this chapter their mathematical model is presented. Then, some remarks are written to conclude if this application can be a valid alternative to the use of the Keplerian Map approach.

5.1 Hyperbolic LPEs Mathematical Model

The concept of Variation of Parameters has been explained in Section 2.1.2, in which the disturbing potential due to the third-body perturbation is written in the case of elliptic motion of the spacecraft with respect to the central planet. Now, some changes have to be done, since the current formulation has to be applied when the particle enters inside the third body sphere of influence: in this case the central planet becomes the third body, but the motion of the particle with respect to him is hyperbolic.
The approach that can be used it to consider an hyperbolic flyby of the particle around the third body, in which the main attractor of the system (e.g. the Sun) acts as perturbing body.
The derivation of the Lagrange's Planetary Equations in their hyperbolic form has been carried out in literature [29], resulting in the following system of

differential equations:

$$\begin{cases} \dfrac{da}{dt} = -\dfrac{2}{na}\dfrac{\partial R}{\partial M_0} \\ \dfrac{de}{dt} = -\dfrac{\sqrt{e^2-1}}{na^2e}\dfrac{\partial R}{\partial \omega} + \dfrac{e^2-1}{na^2e}\dfrac{\partial R}{\partial M_0} \\ \dfrac{di}{dt} = -\dfrac{1}{na^2\sqrt{e^2-1}\sin i}\dfrac{\partial R}{\partial \Omega} + \dfrac{\cos i}{na^2\sqrt{e^2-1}\sin i}\dfrac{\partial R}{\partial \omega} \\ \dfrac{d\Omega}{dt} = \dfrac{1}{na^2\sqrt{e^2-1}\sin i}\dfrac{\partial R}{\partial i} \\ \dfrac{d\omega}{dt} = -\dfrac{\cos i}{na^2\sqrt{e^2-1}\sin i}\dfrac{\partial R}{\partial i} - \dfrac{\sqrt{e^2-1}}{na^2e}\dfrac{\partial R}{\partial e} \\ \dfrac{d\bar{M}_0}{dt} = \dfrac{2}{na}\dfrac{\partial R}{\partial a} - \dfrac{e^2-1}{na^2e}\dfrac{\partial R}{\partial e} \end{cases} \tag{93}$$

where a, e, i, Ω, ω are the orbital elements of the particle, R is the disturbing potential and n is the particle mean motion. $\bar{M}_0$ is the initial hyperbolic mean anomaly of the particle.
It shall be recalled that for hyperbolic orbits, the eccentricity of the particle's orbit is greater than 1, and the following relationships apply [1]:

$$\cos\nu = \frac{\cosh\bar{E} - e}{1 - e\cosh\bar{E}} \qquad \sin\nu = \frac{\sqrt{e^2-1}\sinh\bar{E}}{1 - e\cosh\bar{E}}$$

or inversely: (94)

$$\cosh\bar{E} = \frac{\cos\nu + e}{1 + e\cos\nu} \qquad \sinh\bar{E} = \frac{\sqrt{e^2-1}\sin\nu}{1 + e\cos\nu}$$

where the real part of the hyperbolic eccentric anomaly $\bar{E}$ is defined such that:

$$\bar{E} = 2\tanh^{-1}\left(\sqrt{\frac{e-1}{e+1}}\tan\frac{\nu}{2}\right) \tag{95}$$

Now the disturbing function R that shall be inserted into the LPE of Eq. (93) is obtained considering:

- The attractor that in the previous models was identified as "third body" (with mass m_2), now becomes the main attractor, with mass parameter μ_p
- The celestial body that in the previous models was identified as "main attractor" (with mass m_1), now becomes the disturbing body, with mass parameter μ_s

By adopting this notation it is possible to obtain the third body disturbing function as [9]:

$$R = \frac{\mu_s}{r_{3B}} \left[\left(1 - 2\frac{r}{r_{3B}} \cos\psi + \left(\frac{r}{r_{3B}} \right)^2 \right)^{-1/2} - \frac{r}{r_{3B}} \cos\psi \right] \tag{96}$$

where r_{3B} is the distance between the main attractor and the disturbing body, while ψ is the angle between the spacecraft direction and the direction of the disturbing body with respect to the main attractor (as represented in Fig. 4). Writing the eccentricity direction $\hat{\mathbf{P}}$ and the semi-latus rectum direction $\hat{\mathbf{Q}}$ as in Eq. (13), it is possible to write the $\cos\psi$ as in Eq. (15), which can be algebraically manipulated in the case of hyperbolic orbits, resulting in:

$$\cos\psi = \frac{1}{1 - e\cosh\bar{E}} \left(A(\cosh\bar{E} - e) + B(\sqrt{e^2 - 1}\sinh\bar{E} \right) \tag{97}$$

with A and B defined in Eq. (16). It is necessary to express the disturbing function R through the particle orbital elements, so that it can be partially derived and used for the LPEs. To do so, the reference frame $\{m_2, x'', y'', z''\}$ represented in Fig. 28 can be exploited. It is centered in the body with mass m_2 that now is called main attractor.
The expression of r in Eq. (96) can be written for hyperbolic paths as:

$$r = -\bar{a}\left(1 - e\cosh\bar{E}\right) \tag{98}$$

with $\bar{a} = |a|$, being the semi-major axis on hyperbolic orbits a negative quantity. It is necessary to express $\mathbf{r_{3B}}$ in the inertial frame as:

$$\mathbf{r_{3B}} = \begin{bmatrix} -\dfrac{1}{1-\mu} R_2 \\ 0 \\ 0 \end{bmatrix} \quad \rightarrow \quad \mathbf{r_{3B}^{in}} = R_3(\Omega_p) R_1(i_p) R_3(\omega_p + \theta_p) \cdot \mathbf{r_{3B}} \tag{99}$$

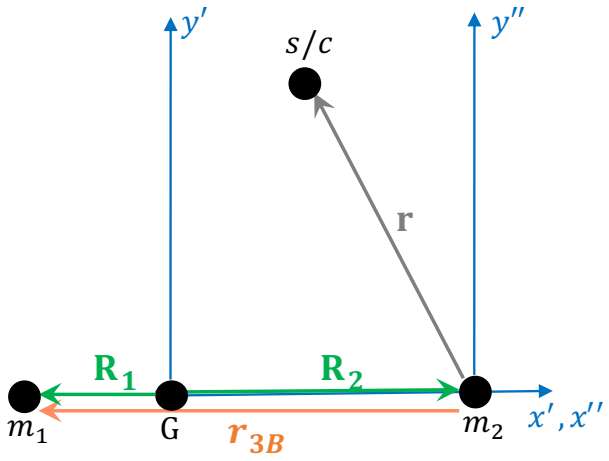

Figure 28: Rotating barycentric reference frame ($\{G, x', y', z'\}$) and planet-centered reference frame ($\{m_2, x'', y'', z''\}$) used to derive the disturbing function R. Axes z' and z'' exiting from the paper.

with R_2 written in Eq. (41), $R_j(\alpha)$ is the rotation matrix of angle α around the j direction, and the orbital elements of the main attractor are $[a_p, e_p, i_p, \Omega_p, \omega_p, \theta_p]$. By writing the position of the disturber in this way, it is possible to easily move from a reference frame to another one (represented in Fig. 28):

- before that the spacecraft enters in the third body SOI, the reference frame used to propagate the motion is centered in the barycentre of the system
- when the propagation is done with the hyperbolic LPEs, the origin of the reference frame is moved to the body with mass m_2, that becomes the primary attractor

Thanks to the aforementioned equations, the disturbing function R in Eq. (96) can be written in function of the particle orbital elements only.
The derivatives of R with respect to the particle orbital elements can be per-

formed as done in the Keplerian Map mathematical model:

$$\begin{cases} \dfrac{dR}{d\bar{a}} = \dfrac{\partial R}{\partial \bar{a}} + \dfrac{\partial R}{\partial \nu}\dfrac{\partial \nu}{\partial \bar{E}}\dfrac{\partial \bar{E}}{\partial \bar{a}} \\ \dfrac{dR}{de} = \dfrac{\partial R}{\partial e} + \dfrac{\partial R}{\partial \nu}\left(\dfrac{\partial \nu}{\partial e} + \dfrac{\partial \nu}{\partial \bar{E}}\dfrac{\partial \nu}{\partial \bar{E}}\dfrac{\partial \bar{E}}{\partial e}\right) \\ \dfrac{dR}{di} = \dfrac{\partial R}{\partial i} \quad ; \quad \dfrac{dR}{d\Omega} = \dfrac{\partial R}{\partial \Omega} \quad ; \quad \dfrac{dR}{d\omega} = \dfrac{\partial R}{\partial \omega} \\ \dfrac{dR}{d\bar{M}_0} = \dfrac{\partial R}{\partial \nu}\dfrac{\partial \nu}{\partial \bar{E}}\dfrac{\partial \bar{E}}{\partial \bar{M}_0} \end{cases} \tag{100}$$

where now the partial derivatives appearing are:

- $$\begin{cases} \dfrac{\partial \nu}{\partial \bar{E}} = \dfrac{\partial \nu}{\partial \cos\nu}\dfrac{\partial \cos\nu}{\partial \bar{E}} = -\dfrac{1+e\cos\nu}{\sqrt{e^2-1}} \\ \dfrac{\partial \nu}{\partial e} = \dfrac{\partial \nu}{\partial \cos\nu}\dfrac{\partial \cos\nu}{\partial e} = \dfrac{\sin\nu}{e^2-1} \end{cases}$$

- $$\bar{a} = \left(\frac{e\sinh\bar{E} - \bar{E} + \bar{M}_0}{\sqrt{a_{3B}^3(1-\mu)}t}\right)^{-2/3} \rightarrow \quad \frac{\partial \bar{E}}{\partial \bar{a}} = \frac{3}{2\bar{a}}\frac{e\sinh\bar{E} - \bar{E} - \bar{M}_0}{1 - e\cosh\bar{E}} \tag{101}$$

- $$e = \frac{\bar{M} - \bar{M}_0 + \bar{E}}{\sinh\bar{E}} \quad \rightarrow \quad \frac{\partial \bar{E}}{\partial e} = \left(\frac{\partial e}{\partial \bar{E}}\right)^{-1} = -\frac{\sin\nu}{\sqrt{e^2-1}}$$

- $$\bar{M}_0 = \bar{M} - e\sinh\bar{E} + \bar{E} \quad \rightarrow \quad \frac{\partial \bar{E}}{\partial \bar{M}_0} = \left(\frac{\partial \bar{M}_0}{\partial \bar{E}}\right)^{-1} = -\frac{1+e\cos\nu}{e^2-1}$$

With the computation of such derivatives it is possible to integrate the LPEs in hyperbolic form, to obtain the evolution of the orbital elements of the particle inside the sphere of influence of the third body.

5.2 Application procedure and remarks

In this part it is explained the algorithm that can be used to propagate the motion of the spacecraft starting from a generic initial condition, trying to

improve the results obtained with the Keplerian Map in Section 3.
Through a proper check done at each integration point, the position of the particle when it crosses the SOI of the third body is obtained through the numerical integration of the Keplerian Map. If the spacecraft will never reach the SOI of the third body, then the propagation is done for a complete orbital period as in the Keplerian Map application, leading to the same results shown in Section 3.
In the case that the particle reaches the SOI, then the integration is stopped and a change of coordinates is performed. If the states of the spacecraft in the reference frame of the Keplerian Map when it crosses the SOI are called $\mathbf{s}_{\mathbf{SOI}}^{\mathbf{km}}$, then the states of the particle with respect to the third body are written as:

$$\mathbf{s}_{\mathbf{SOI}}^{\mathbf{3B}} = \mathbf{s}_{\mathbf{SOI}}^{\mathbf{km}} - (1-\mu)\mathbf{s}_{\mathbf{3B}} \tag{102}$$

where $\mathbf{s_{3B}}$ are the states of the third body with respect to the primary in the inertial barycentric reference frame, at the instant at which the particle crosses its SOI. The mass parameter μ is defined as in Eq. (1).
Thanks to the know procedure that allows to pass from the position and velocity to the orbital elements of the particle, the initial conditions for the hyperbolic LPEs can be computed. They are used as initial point for the numerical integration of the equations, which is stopped when the particle crosses again the sphere of influence of the third body.
At this point it is possible to apply the Eq. (102) and perform the final integration of the motion through the Keplerian Map approach.
This procedure has been adopted to reproduce the error maps present in Section 3. However, it is important to make a consideration: when the mass parameter of the system increases, the concept of Sphere Of Influence is meaningless, since the perturbation of the third body remains significant even outside from it. Therefore, to apply the hyperbolic LPEs inside the SOI of the third body could not be the best approach to improve the model of the Keplerian Map.
This is something that has been confirmed with the $C_J - \mu - \varepsilon_{\Delta a}$ map and the $MRD - \mu - \varepsilon_{\Delta a}$ map obtained with the tool explained in this section (represented in Fig. 29 and Fig. 30). The model of the Keplerian Map appears to be more efficient and most importantly more accurate than the procedure that exploits the hyperbolic LPEs. This can be easily seen in the $C_J - \mu - \varepsilon_{\Delta a}$ map: in the cases in which the particle crosses the third body SOI (marked in Fig. 12b), the error obtained propagating with the hyperbolic LPEs is higher

than when just the Keplerian Map is used. In general, in both the maps the error appears to be higher than the one in Fig. 11 and Fig. 16.
Such consideration does not want to state that there is not the possibility to improve the model, but suggests to move in this direction considering another switching condition, forgetting the concept of SOI when the mass parameter of the system is big (as in the Earth-Moon system).
To conclude, for the aforementioned reasons, it results that the model explained in this section is not able to increase the accuracy of the Keplerian Map propagation, at least not for high mass parameters (where an improvement is needed).

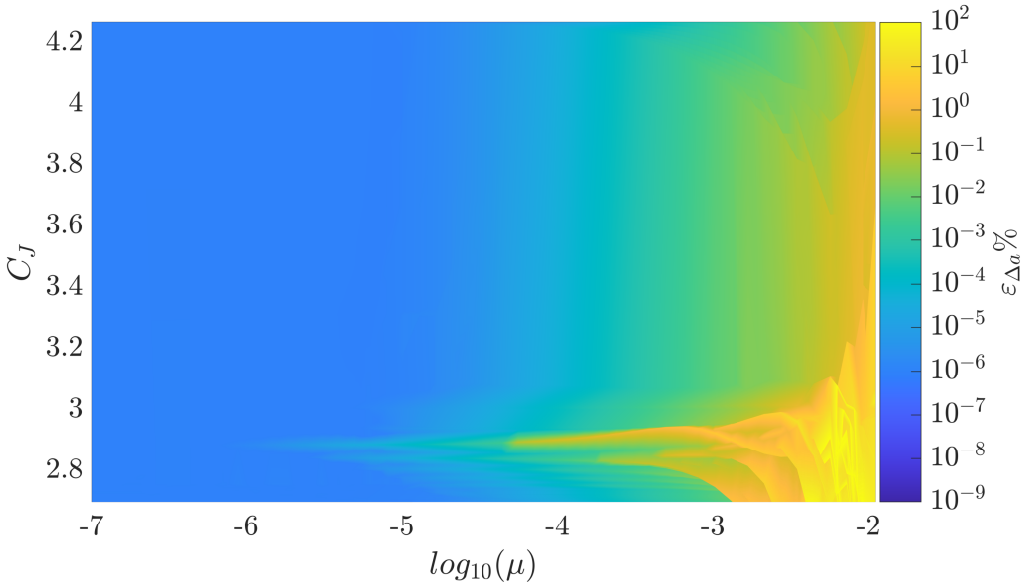

Figure 29: $C_J - \mu - \varepsilon_{\Delta a}$ Map obtained with the Keplerian Map + Hyperbolic LPEs when the particle flies inside the SOI of the third body.

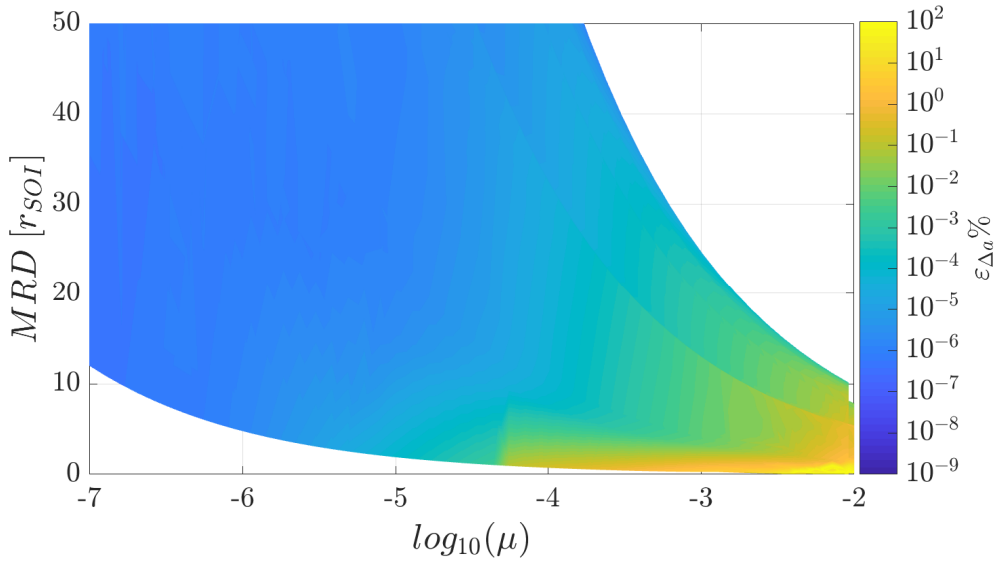

Figure 30: $MRD - \mu - \varepsilon_{\Delta a}$ Map obtained with the Keplerian Map + Hyperbolic LPEs when the particle flies inside the SOI of the third body.

CHAPTER 6

Distant retrograde orbits design with the Keplerian map

THIS final part is dedicated to exploit the Keplerian Map approach to design distant retrograde orbits.
From the analysis carried in Section 3, it is possible to identify different scenarios in which the theory can be applied to predict the motion of the spacecraft (as the Jupiter system, the Mars system, the Saturn system, etc...). In such cases, instead of using the common three-body problem equations, the use of the Keplerian Map entails improvements in the computational time required to propagate the motion, granting results with good accuracy.
In the current work the method has been applied in a multi-bodies perturbed environment to generate Distant Retrograde Orbits (DRO), also called Quasi-Satellite Orbits (QSO). As will be presented in the following section, such orbits allow to to save propellant budget and transfer times, with benefits even for navigation purposes, station keeping techniques and mission objectives.
To identify such orbits it is necessary the use of an optimisation process, which is aimed in finding the required initial conditions of the problem. The use of the Keplerian Map in an optimisation algorithm allows to reach the convergence in a smaller amount of time than when exploiting the three-body problem equations.
In past works [17] it was demonstrated the use of the Keplerian Map in trajectory design from unstable manifolds of the Libration point L_2 to reach a Near-Earth Asteroid (NEA), and multi-flybys trajectory optimisations in the Jovian system. In such applications it was demonstrated that the Keplerian Map introduces a gain in computational time achieved with respect to the N-body problem, opening the door to larger trajectory optimisation processes. However, this method has never been used to design a QSO in past studies, making such application a novelty.

In order to justify the decision of designing distant retrograde orbits, the chapter opens with an introduction about the QSOs to show the advantages introduced by such trajectories. Then, the new disturbing function used in the LPE will be computed, and finally the results obtained will be presented.

6.1 Quasi-Satellite Orbits definition

As anticipated in the introduction part of the chapter, the reason of the choice of a particular orbit in a space mission is not only related to the minimisation of the propellant costs, but other parameters play a key role when designing the trajectory of the mission. In general, the parameters that can be considered as "costs" for the mission are strictly dependent on the mission objectives. For instance, in a mission whose objective is to perform remote sensing above the surface of a celestial body (as a planet, a moon, an asteroid) with the intent of studying its surface, the coverage of the trajectory is an important parameter that determines the kind of orbit chosen.
In a mission in which it is necessary to maximise the coverage and reduce the station keeping costs (that can be high in strongly-perturbed environments), a solution that is proposed is the use of Distant Retrograde Orbits (DRO), also known as Quasi-Satellite Orbits (QSO), particular cases of the "horseshoe" and "tadpole" types of orbits [30]. They represent a useful alternative to gravitationally bounded orbits when a space probe needs to remain for a long time in the neighborhood of a celestial body.
A spacecraft that is orbiting around a planet with almost resonant motion with its moon (i.e. the spacecraft and the moon rotates with almost identical periods around the central planet) is the field of application of the QSO, that are particular retrograde quasi-synchronous orbits. The QSO can also be seen as an orbit around the more massive body and perturbed by the less massive one in a way that forces the probe to stay in its vicinity, at least for a certain period of time.
This peculiar orbits have the goal of obtaining a global longitudinal coverage of the surface of the moon, maximising the latitudinal one, ensuring an almost constant altitude from the surface. Indeed, it might be necessary to maintain a constant altitude over the surface during the remote science phase, when a deep analysis is needed and when fast and close passages are not enough for the study of the terrain.
However, the real advantage of the QSO with respect to other kinds of tra-

jectories exploited in relative dynamics is that it is a naturally-stable orbit, so that the costs related to the station keeping are heavily reduced.
In general, to observe the surface of a body, even other kinds of orbits can be selected. Many times the exploitation of a stable manifold around a Libration point is a solution adopted that allows to maintain the satellite orbiting around an object. The disadvantages in this choice are multiple:

- A close orbit around a Libration point is something that in a perturbed environment requires a costly station keeping strategy to prevent the motion from decaying in an unstable trajectory
- It is almost impossible to obtain a global coverage of the surface exploiting an orbit around a Libration point, since in general they allows a stable motion over the body's surface, covering only a small ground track region (the motion of a moon is usually tidally locked)
- In systems where the third body is very small with respect to the primary, the Libration points L_1 and L_2 are always just above the surface of the secondary, meaning that the altitude of an orbit around them is too near the ground, following a weak coverage, limiting the Field Of View (FOV) of the optical instrumentation and increasing the impact risks

A first study of Quasi-Satellites Orbits has been carried out searching for a long-term stability around the Martian moon Phobos [31]. A dynamical model including Mars gravity and oblateness was developed [32] and then the problem was extended to the R3BP including the eccentricity of the moon. Other studies demonstrated the dynamics of asteroids that are in QSO around some planets [2], but the main scenario in which this kind of orbit are applied is the Martian environment [33].
With the strongly perturbing gravity of Mars and the masses of Phobos and Deimos being too small to capture a satellite, it is not possible to orbit the Martian moons in the usual sense [31]. On the other hand, the mass of Phobos or Deimos can not be neglected in the dynamics of a satellite orbiting at high altitudes from Mars' surface, therefore it is necessary to use the three-body problem to model a motion comprehending a primary (Mars) and a secondary attractor (Phobos or Deimos).
Since Phobos and Deimos are very small, their sphere of influence lies completely below its surface and the Langrangian points L_1 and L_2 are immediately above them [22].

The planetary constants of Mars, Phobos and Deimos are listed in Table 10. As it can be deduced, the mass of the moons are very small compared to the one of Mars. The mass parameters of the systems Mars-Phobos and Mars-Deimos are shown in Table 3. Being the Martian environment a very suitable and

Table 10: Planetary constants of Mars, Phobos and Deimos [27].

μ_{σ} [$\mathbf{km^3/s^2}$]	μ_P [$\mathbf{km^3/s^2}$]	μ_D [$\mathbf{km^3/s^2}$]
$4.283 \cdot 10^4$	$7.088 \cdot 10^{-4}$	$9.616 \cdot 10^{-5}$

familiar case for this kind of orbits, even in the present work they are chosen as applications to show the effectiveness of the Keplerian Map.

6.2 Modeling Martian environment

Before explaining how the mathematical model is built and the optimisation algorithm to generate a Quasi-Satellite Orbit, it is necessary to mention the reference frames adopted in this scenario. In particular, in the modeling of the QSO has been used the SPICE toolkit by NASA [34] to obtain the ephemerides of Phobos and Deimos.
The first frame that can be introduced is the Mars IAU frame (Mars Mean Equator and IAU vector of J2000 frame [35]), which is an inertial barycentric reference frame defined as in Fig. 1, composed with:

- The X-axis directed towards the IAU-vector at Mars (this vector is the cross product of Earth mean north with Mars mean north).
- the Z-axis is directed as Mars' North Pole.
- the Y-axis completes an orthonormal basis with X and Z axes.

In this frame are given the ephemerides of Phobos or Deimos needed for the Keplerian Map mathematical model. Other two frames that can be defined are the Phobos Equatorial frame and Deimos Equatorial frame. They are centered on Phobos/Deimos barycentre, with:

- Z-axis pointing towards the North pole direction of Phobos/Deimos.
- X-axis is defined as cross product between the North pole direction of Phobos/Deimos and the North pole direction of Mars.

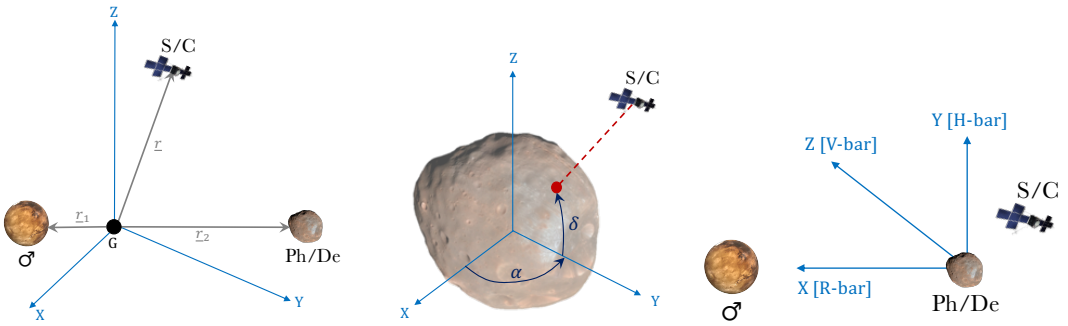

(a) Mars IAU frame **(b)** Phobos/Deimos Equatorial frame **(c)** LVLH frame

Figure 31: Three main reference frames used in the design of the QSO. The Phobos/Deimos Equatorial frame contains even the right ascension and declination.

- Y-axis completes an orthonormal basis with X and Z axes.

These two reference frames are used to project the orbit of the spacecraft onto Phobos'/Deimos' surface, to represent the ground track, adopting the right ascension and the declination of the spacecraft.
The last reference frame is the LVLH (Local-Vertical Local-Horizontal) frame, which rotates with the Mars-Phobos/Deimos direction. It is centered in the moon barycentre, with:

- X-axis (also called R-bar) directed from Mars toward the targeted moon.
- Z-axis (also called V-bar) pointing in the direction of the orbital angular momentum of the moon.
- Y-axis (also called H-bar) completes an orthonormal basis with X and Z axes.

In this frame the spacecraft on the QSO performs a retrograde motion in elliptical epicycles around the moons [22], and it is the frame used for the optimisation process. The Mars IAU frame, the Phobos/Deimos Centered frame and the LVLH frame are shown in Fig. 31.
After a brief introduction in which the main frames adopted in the modeling have been mentioned, it is possible to quickly describe the Martian environment in terms of orbital perturbations. This is relevant for the disturbing potential that is used in the Keplerian Map theory.

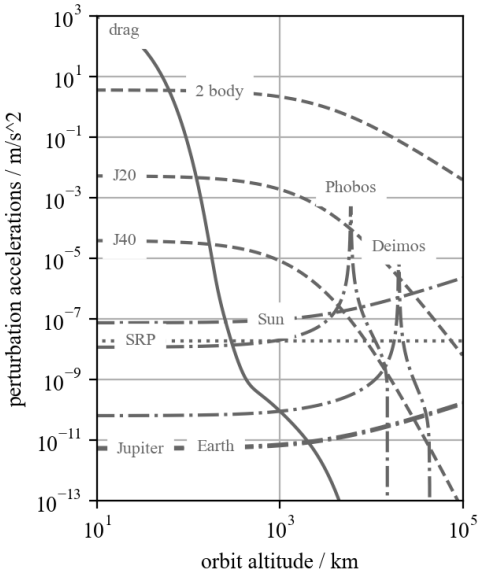

Figure 32: Main perturbations acting in Martian environment [36] with corresponding orders of magnitude as function of the distance from the surface.

In Fig. 32 are represented the order of magnitudes of the main perturbations acting on the orbit of a satellite [36], as function of the distance from Mars' surface. It can be deduced that at Phobos and Deimos distances, the main perturbations that can be considered are Mars J_2, J_4, the Sun presence and the Solar Radiation Pressure (SRP). However, since this discussion is intended to demonstrate the use of the Keplerian Map, in addition to the third body disturb, it will be considered only the effect of Mars J_2. The introduction of this perturbation in the Keplerian Map mathematical model is explained in Section 6.3.

6.3 New disturbing function and Keplerian Map applicability

As anticipated in Section 6.2, in addition to the disturbing potential of the Keplerian Map due to the presence of Phobos/Deimos, another perturbation that is included in the mathematical model is Mars zonal harmonic potential J_2, which plays a significant role even in Phobos and Deimos proximity (as shown in Fig. 32).

The Zonal harmonics Potential function is modeled as an expansion of spherical harmonics functions in Legendre polynomials [37]:

$$R_{ZH} = -\frac{\mu}{r}\sum_{n=2}^{\infty} J_n \left(\frac{R_p}{r}\right)^n P_n\left(\cos\phi\right) \tag{103}$$

in which μ is the planetary constant, R_p the planet mean radius, r the spacecraft distance from the centre of the planet, ϕ the latitude of the spacecraft, J_n a tabulated coefficient experimentally determined and P_n is the Legendre polynomial of order n. The latter, has the expression [37]:

$$P_n(x) = \frac{1}{2^n n!}\frac{d^n}{dx^n}\left[\left(x^2-1\right)^n\right] \tag{104}$$

It is necessary to express the disturbing function R_{ZH} in dependence of the particle orbital elements. This is achieved with the relation between the spacecraft latitude and its position [37]:

$$\cos\phi = \frac{z_{eq}}{r} \tag{105}$$

with z_{eq} the out-of-plane component of the spacecraft position vector in Mars equatorial frame.
The potential function of Mars J_2 is obtained taking the expansion in Eq. (103) up to order 2. The Legendre Polynomial of second order is:

$$P_2(\cos\phi) = \frac{1}{2}\left(3\sin^2\left(\omega+\nu\right)\sin^2\left(i\right)-1\right) \tag{106}$$

which is inserted into the potential, obtaining [6]:

$$R^{\sigma}_{J_2} = -\frac{\mu_{\sigma} R^2_{\sigma}}{r_1^3} J_2 \left(3\sin^2\left(\omega+\nu\right)\sin^2\left(i\right)-1\right) \tag{107}$$

where μ_{σ} is the planetary constant of Mars (written in Table 10), $R_{\sigma} = 3389.9$ km is Mars mean radius [38], the value of J_2 is the value experimentally computed from Phobos-Grunt mission [22]:

$$J_2 = 1.96045 \cdot 10^{-3} \tag{108}$$

The term r_1 in Eq. (107) is the distance of the spacecraft with respect to Mars:

$$r_1 = \sqrt{r^2 + \left(\frac{\mu}{1-\mu}\frac{a_{3B}(1-e_{3B}^2)}{1+e_{3B}\cos\theta_{3B}}\right)^2 + 2r\cos\theta\frac{\mu}{1-\mu}\frac{a_{3B}(1-e_{3B}^2)}{1+e_{3B}\cos\theta_{3B}}} \tag{109}$$

By inserting the expression of r_1 in $R_{J_2}^{\mathcal{O}}$ and computing the angle θ as in Eq. (46) , the J_2 disturbing function is written in the orbital elements of the particle, and can be added to the total disturbing function:

$$R_{tot} = R_{KM} + R_{J_2}^{\mathcal{O}} \tag{110}$$

with R_{KM} the disturbing function of the Keplerian Map, computed as in Eq. (44).
The partial derivatives of the total disturbing function in Eq. (110) are computed through Eq. (50), and then inserted into the LPE of Eq. (9) to compute the orbital elements evolution with time.
It is worth highlighting that Phobos and Deimos are assumed with spherical gravitational field, therefore no disturbing terms are present in the total disturbing potential. This assumption has been done to not overload the mathematical model, and remembering that the analysis is focused on the use of the Keplerian Map.
Before presenting the scheme adopted to generate the initial conditions of the QSO, it is useful to spend few words about the Keplerian Map applicability.
Since now the model is developed in the R3BP context, it makes no sense to speak about Jacobi Integral. However, other considerations can be done regarding the value of μ and the MRD.
In both systems Mars/Phobos and Mars/Deimos, the mass parameter is quite small (orders of 10^{-8} and 10^{-9} as written in Table 3), meaning that the expected error in terms of orbital elements variation is very small. In addition to this, it shall be remarked that Phobos and Deimos have their sphere of influence that lies completely inside their surface. This means that the spacecraft will remain always outside from it, and the MRD will be always above the unity.
From these two considerations is safe to say that the Keplerian Map theory is a suitable method that can be used for the propagation of the particle motion in this case.

6.4 Optimisation Process

An optimisation algorithm is exploited to generate the QSO initial conditions, such that the orbit is naturally stable for 30 days. The trajectory is considered stable if the spacecraft remains in a certain range of altitude over the moon surface, without going too far or too close from it. The cost function to be

minimised involves also a parameter related to the maximum latitude covered by the ground track on the moon surface. Indeed, as aforementioned, one of the real advantages of the QSO is that it allows to achieve high levels of coverage. However, the higher is the inclination of the orbit with respect to the moon (high inclination corresponds to high maximum latitude), the lower will be the stability period of such QSO [33]. In this section is summarised the structure of the optimisation algorithm adopted and how the cost function is defined.
The optimisation variables, in the LVLH frame, consist on the relative displacement between S/C and moon along the x direction, tangential velocity component and the out-of-plane velocity. Therefore the initial states of the particle in the LVLH frame are:

$$\mathbf{s_0^{rel}} = [\, x_0 \,,\; 0 \,,\; 0 \,,\; 0 \,,\; v_{y_0} \,,\; v_{z_0} \,]^T \tag{111}$$

where x_0, v_{y_0} and v_{z_0} are the degrees of freedom of the optimisation, while the other initial states are imposed as zero, meaning that initially the satellite has null velocity along the radial direction, and lies on the conjunction between the moon and Mars.
The initial states are then transformed in the Mars IAU frame. In order to do that, it is necessary to obtain the position and the velocity of Phobos/Deimos with respect to the barycentre at the initial epoch $\mathbf{s^0_{P/D}}$ through SPICE toolkit [34]. Defining the rotation matrix from LVLH frame to the Mars IAU frame as R^{IAU}_{LVLH}, then:

$$\mathbf{s_0} = \begin{bmatrix} \mathbf{r_0} \\ \\ \mathbf{v_0} \end{bmatrix} = \begin{bmatrix} \mathbf{r^0_{P/D}} + R^{IAU}_{LVLH} \cdot \mathbf{r^{rel}_0} \\ \\ \mathbf{v^0_{P/D}} + R^{IAU}_{LVLH} \cdot \mathbf{v^{rel}_0} + \dot{R}^{IAU}_{LVLH} \cdot \mathbf{r^{rel}_0} \end{bmatrix} \tag{112}$$

are the initial states of the spacecraft in Mars IAU frame.
This initial states can be translated in the initial Keplerian elements around the barycentre through the well known transformation. They can be used as initial conditions for the numerical integration of the LPE, that are propagated for 30 days.
The choice of such time span is in line with what is present in literature [31]. Numerical studies on the QSO demonstrated that the higher the stability period, the lower the maximum latitudes of coverage. One month of stability is a good compromise, but even orbits with longer stability have been computed. After that the propagation has been done, the states of the particle during the

30 days $\mathbf{s(t)}$ are transformed in Phobos/Deimos Equatorial frame $\mathbf{s^{eq}(t)}$ with the relation:

$$\mathbf{s^{eq}(t)} = R_{IAU}^{EQ} \cdot \big(\mathbf{s(t)} - \mathbf{s_{P/D}(t)}\big) \tag{113}$$

where $\mathbf{s_{P/D}(t)}$ are the states of Phobos/Deimos at a given time t, and R_{IAU}^{EQ} is the rotation matrix from Mars IAU frame to Phobos/Deimos equatorial frame. In this frame it is possible to compute the ground track of the satellite over the moon surface, and obtain the parameters determining the quality of the QSO:

- The maximum latitude achieved by the spacecraft over the moon surface ϕ_{max} during the time span
- The average altitude of the satellite with respect to the moon h_{avg} during the time span
- The maximum and minimum altitude reached by the satellite with respect to the moon h_{min}, h_{max} during the time span

With the first two quantities, it is possible to define the cost function to be minimised:

$$\mathcal{J} = h_{avg} \cdot \left(\rho_1 + \frac{1}{\phi_{max}}\right) \tag{114}$$

with ρ_1 set to 0.1 after a trial and error process.
Moreover, h_{min} and h_{max} are used to see if the QSO obtained is a valid one or not, in particular:

$$\text{if} \begin{cases} h_{min} < 20 \text{ km} \\ \quad \text{or} \\ h_{max} > 150 \text{ km} \end{cases} \Bigg\| \rightarrow \text{ QSO not valid} \tag{115}$$

If the QSO is not valid, then the cost function is set to $\mathcal{J} = 10^4$, penalising the current solution in the optimisation process.
The cost function $\mathcal{J}$ is given to an heuristic optimisation method (as the Genetic Algorithm, Particle Swarm, etc...) to find its minimum.
This is the scheme adopted to generate a QSO with high maximum latitude and constant, low altitudes. In the next parts of the chapter are presented the results of the optimisation.

6.5 Analysis of the results

From the optimisation process described in Section 6.4, it is possible to obtain the set of initial conditions $\mathbf{s_0^{rel}}$ so that the spacecraft trajectory propagated for 30 days gives the best QSO in terms of average altitude and maximum latitude.
In this section are firstly reported the trajectories for Phobos and Deimos orbits, then the results are commented highlighting the use of the Keplerian Map. Finally, a comparison with the results obtained when propagating through the R3BP equations is done, focusing on the time required to the optimisation algorithm to converge.

6.5.1 Phobos QSO

The solution that is presented is the one associated with the initial conditions listed in Table 11, in which there are listed also the main features of the orbit. The QSO can be appreciated in Mars IAU frame in Fig. 33. As can be seen, the paths of the spacecraft and of Phobos are almost overlapped, but in reality the S/C is relatively rotating around the moon.
The motion of the probe around Phobos in the LVLH frame is depicted in Fig. 35, and the associated ground track is shown in Fig. 34.

Table 11: Initial states in Phobos LVLH frame and features of the corresponding QSO if the motion is propagated for 30 days. Initial epoch: 21^{th} December, 2021 $13:30$ UTC

$\mathbf{s_0^{rel}} = [-60.89 \text{ km}, 0, 0, 0, 14.79 \text{ m/s}, 9.96 \text{ m/s}]^T$			
h_{min}	h_{max}	h_{avg}	ϕ_{max}
38.27 km	163.58 km	76.92 km	49.99 deg

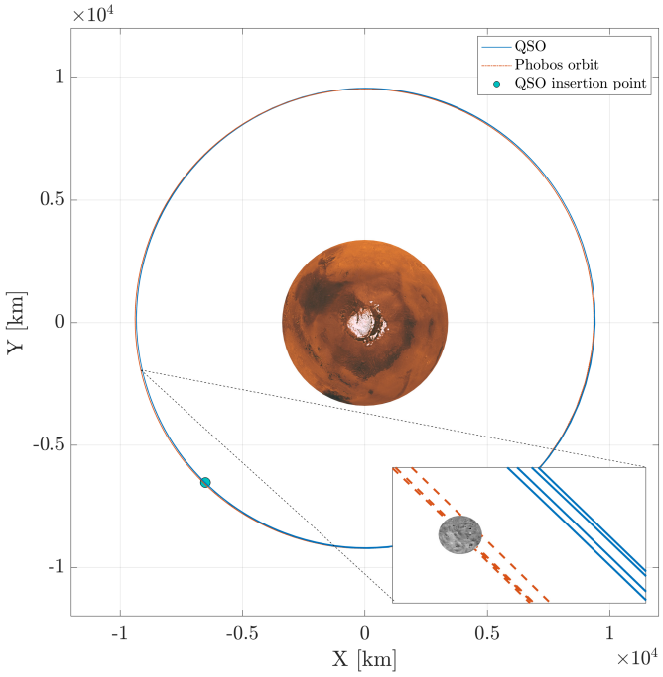

Figure 33: QSO around Phobos represented in Mars IAU frame. Trajectory propagated for one day (to obtain a better visibility).

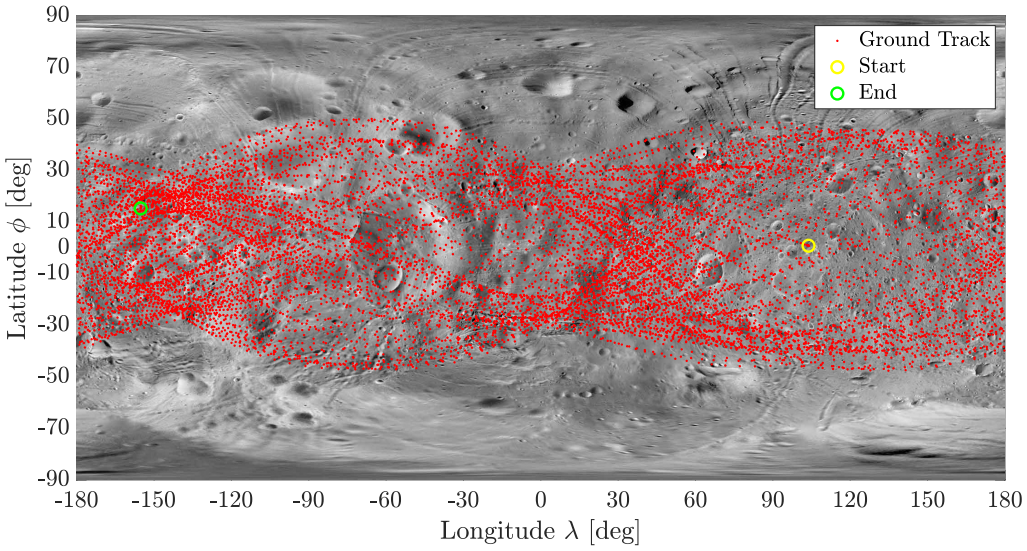

Figure 34: Ground track of the QSO around Phobos, with initial and final points.

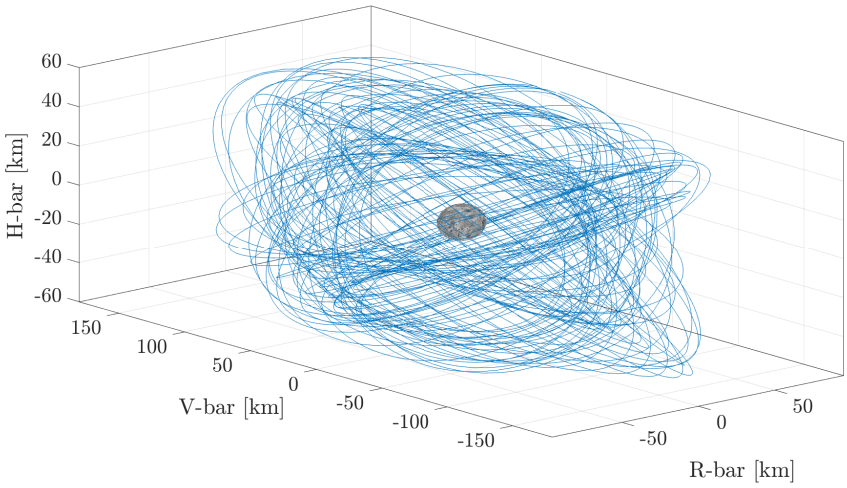

(a) Phobos QSO - 3D view

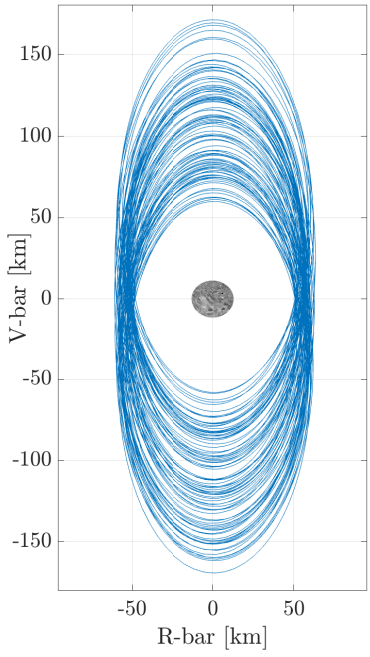

(b) Phobos QSO - Upper view

Figure 35: QSO around Phobos in LVLH frame seen from two different point of views.

A last result that can be shown regards the evolution of the orbital elements of the particle in the inertial barycentric reference frame. They are represented in Fig. 36. From them it is possible to observe a periodic variation with larger frequencies and one with shorter due to the orbital perturbation effects. The error introduced with the Keplerian Map remains quite small for all the orbital elements. If α_i is the $i-th$ orbital element, the evolution of the error with time obtained comparing the numerical solution of the R3BP equations and the one with the Keplerian Map, is:

$$\varepsilon_{\alpha_i}(t) = \left| \frac{\alpha_i(t)^{KM} - \alpha_i(t)^{R3BP}}{\alpha_i(t)^{R3BP}} \right| \cdot 100 \tag{116}$$

where $\alpha_i(t)^{R3BP}$ is the $i-th$ orbital element of the particle at time t obtained with the R3BP numerical integration (with the addition of the J_2 perturbation), while $\alpha_i(t)^{KM}$ is referred to the orbital element obtained from the LPE integration.
The errors ε_{α_i} are represented in Fig. 37. For all the orbital elements the relative percentage error remains below $10^{-5}\%$ (with exception of some peaks in the case of the argument of pericentre that reach $10^{-4}\%$), confirming the almost exact numerical propagation through the Keplerian Map theory.

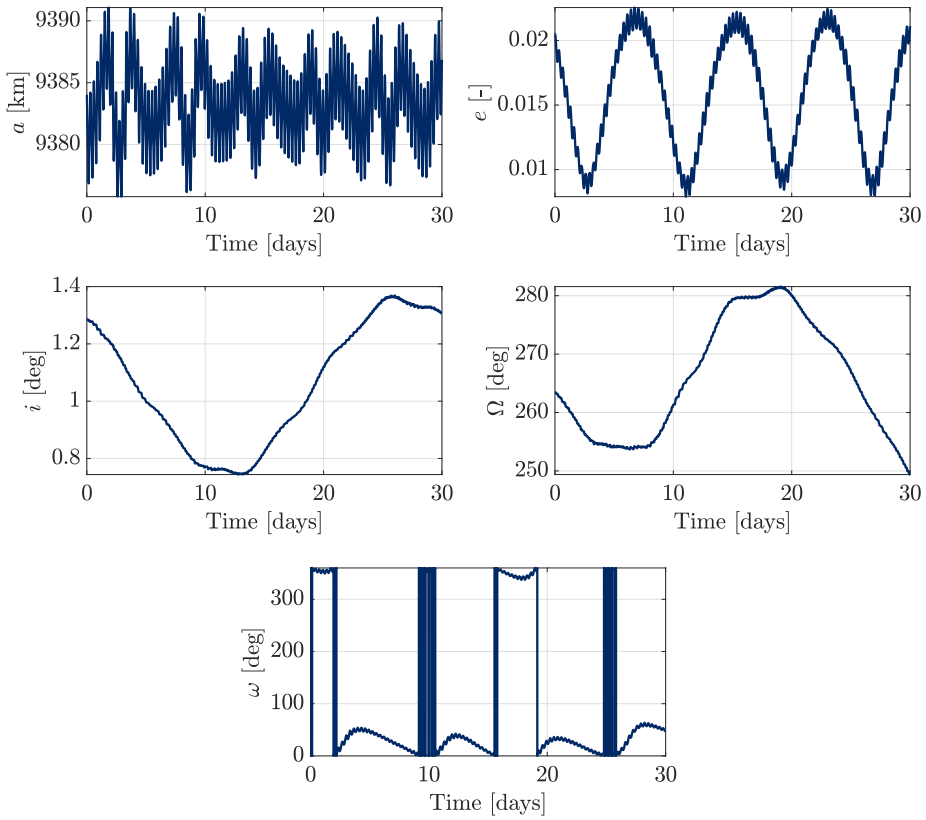

Figure 36: Orbital elements evolution with time for Phobos QSO.

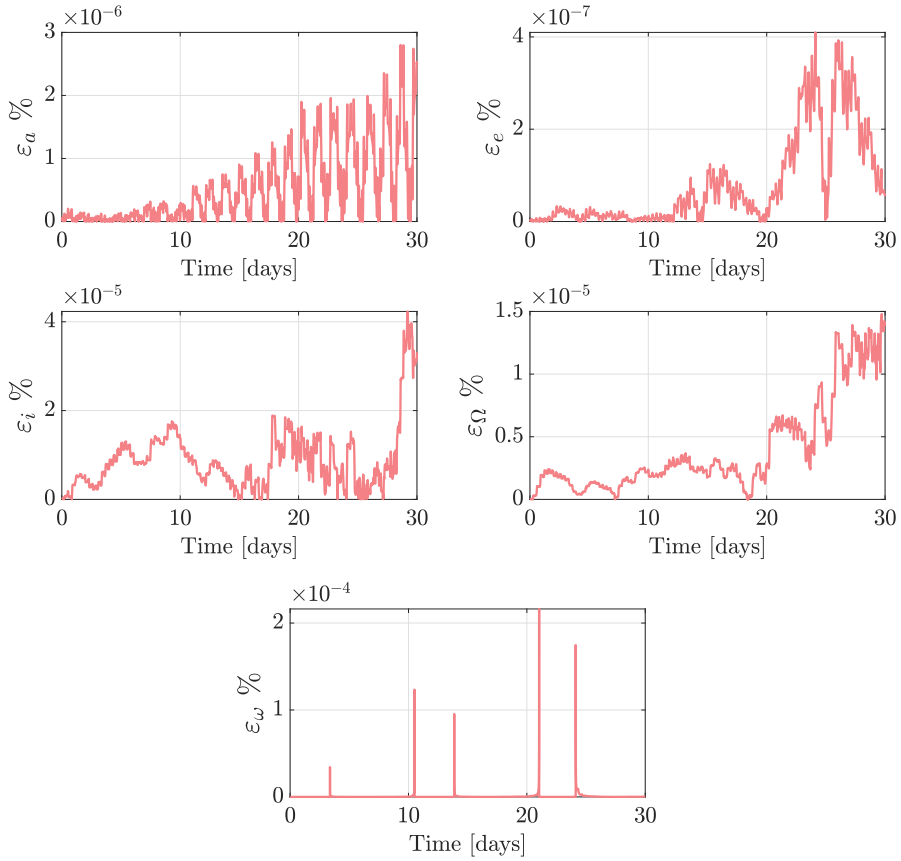

Figure 37: Relative percentage error (defined in Eq. (116)) between numerical integration of R3BP equations and LPE evolution with time for each orbital element, referred to Phobos QSO.

Table 12: Initial states in Deimos LVLH frame and features of the corresponding QSO if the motion is propagated for 30 days. Initial epoch: 21^{th} December, 2021 $13:30$ UTC

$\mathbf{s_0^{rel}} = [\,-93.45$ km , 0 , 0 , 0 , 5.50 m/s , 4.12 m/s $\,]^T$			
h_{min}	h_{max}	h_{avg}	ϕ_{max}
85.54 km	194.75 km	112.46 km	48.31 deg

6.5.2 Deimos QSO

The same results shown for Phobos QSO in Section 6.5.1 are now presented for the QSO around Deimos. The output of the optimisation process is written in Table 12, with the associated features of the trajectory during the 30 days.
With respect to the QSO around Phobos, now the spacecraft flew farther from the surface of the moon, but reaches almost the same longitudinal coverage. Deimos has a mass parameter that is an order of magnitude smaller than the one of Phobos, therefore its attraction on the probe is less effective.
The larger distances can be appreciated in the plots where the path is depicted. Firstly, with the motion in Mars IAU frame shown in Fig. 38, then with the transformation into the LVLH frame (represented in Fig. 40).
The associated ground track is shown in Fig. 39, where it can be noticed that now the spacecraft is "rotating" slower around the moon. The orbital elements evolution with time during the time span is reported in Fig. 41. To conclude, the error comparing the results from the R3BP and the ones from the LPE numerical integration is shown in Fig. 42. Even in this case, a propagation with high accuracy is confirmed from these plots.

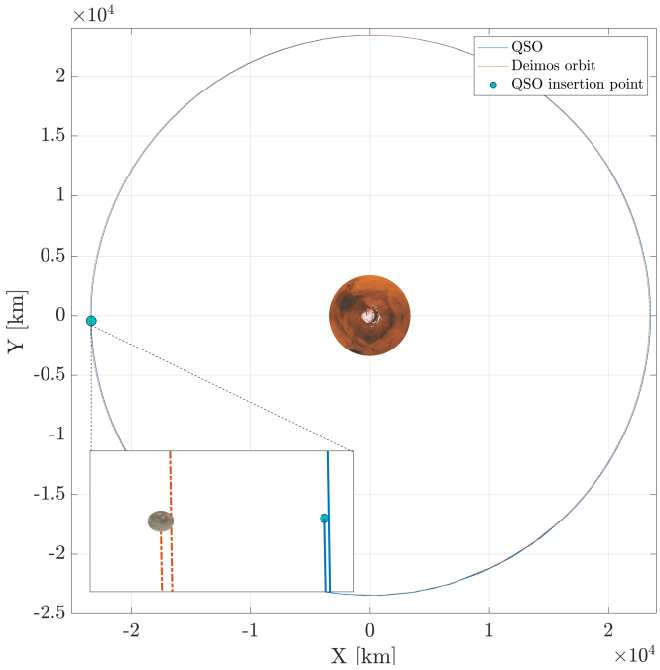

Figure 38: QSO around Deimos represented in Mars IAU frame. Trajectory propagated for two days (to obtain a better visibility).

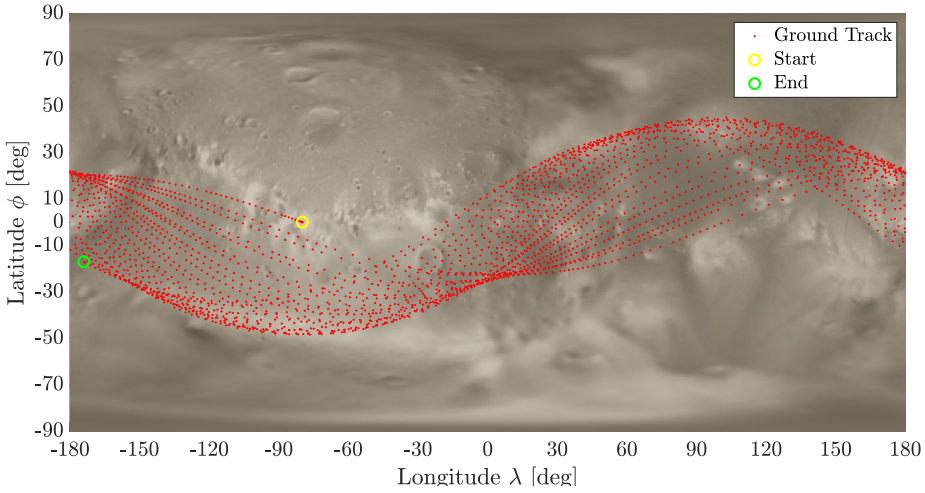

Figure 39: Ground track of the QSO around Deimos, with initial and final points.

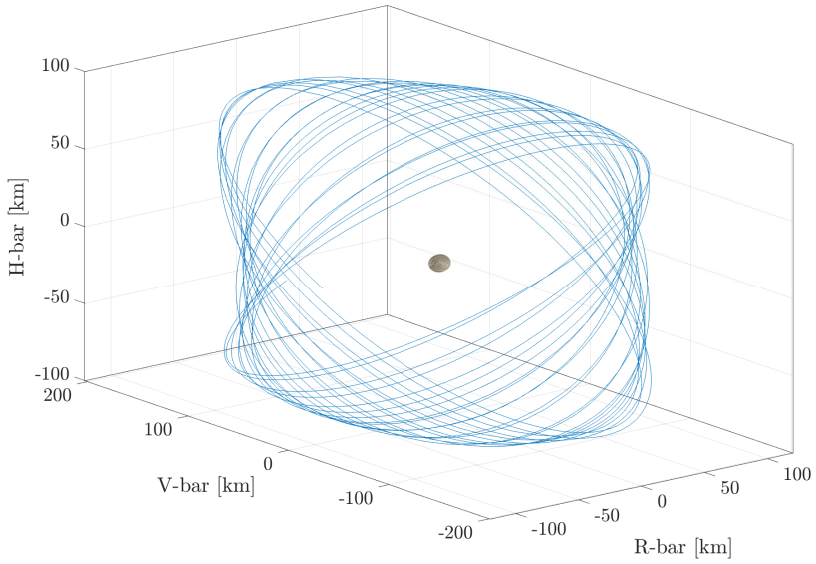

(a) Deimos QSO - 3D view

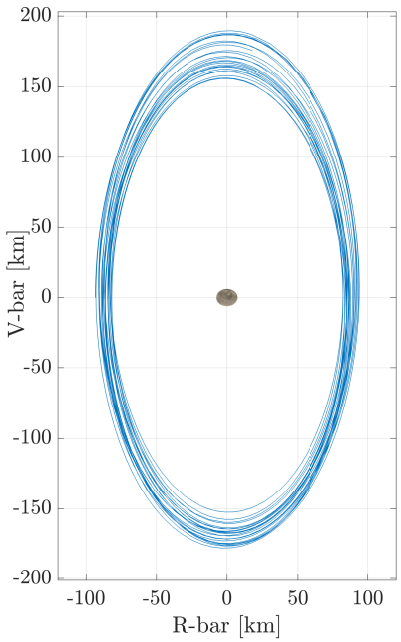

(b) Deimos QSO - Upper view

Figure 40: QSO around Deimos in LVLH frame seen from two different point of views.

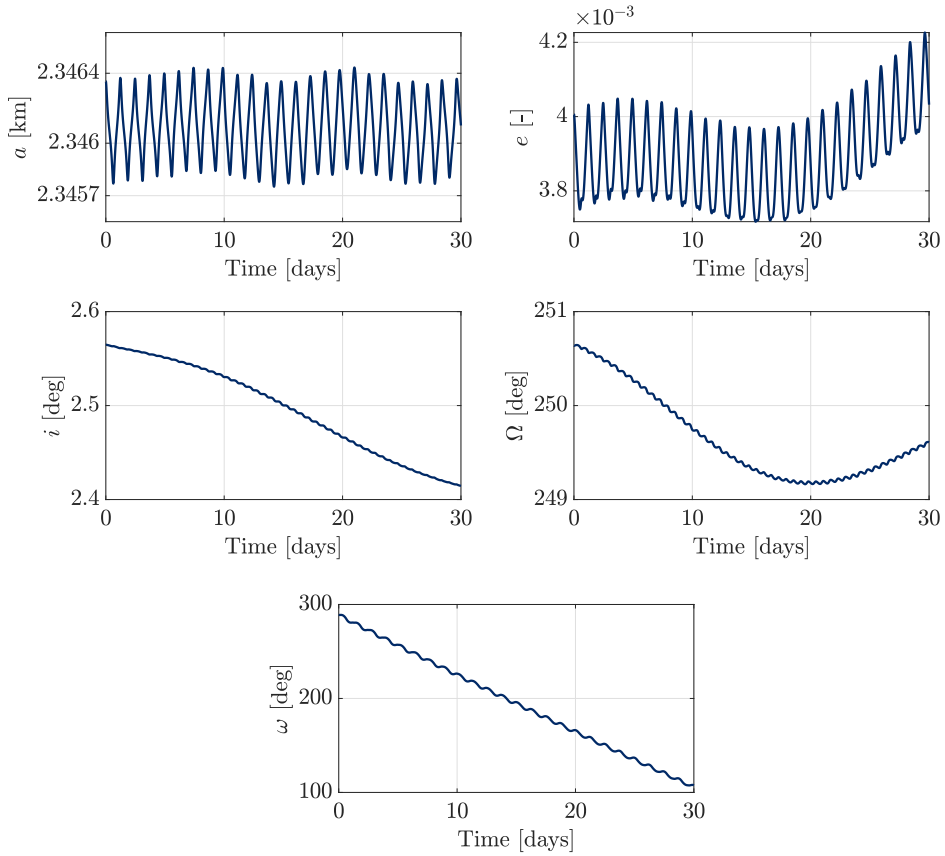

Figure 41: Orbital elements evolution with time for Deimos QSO.

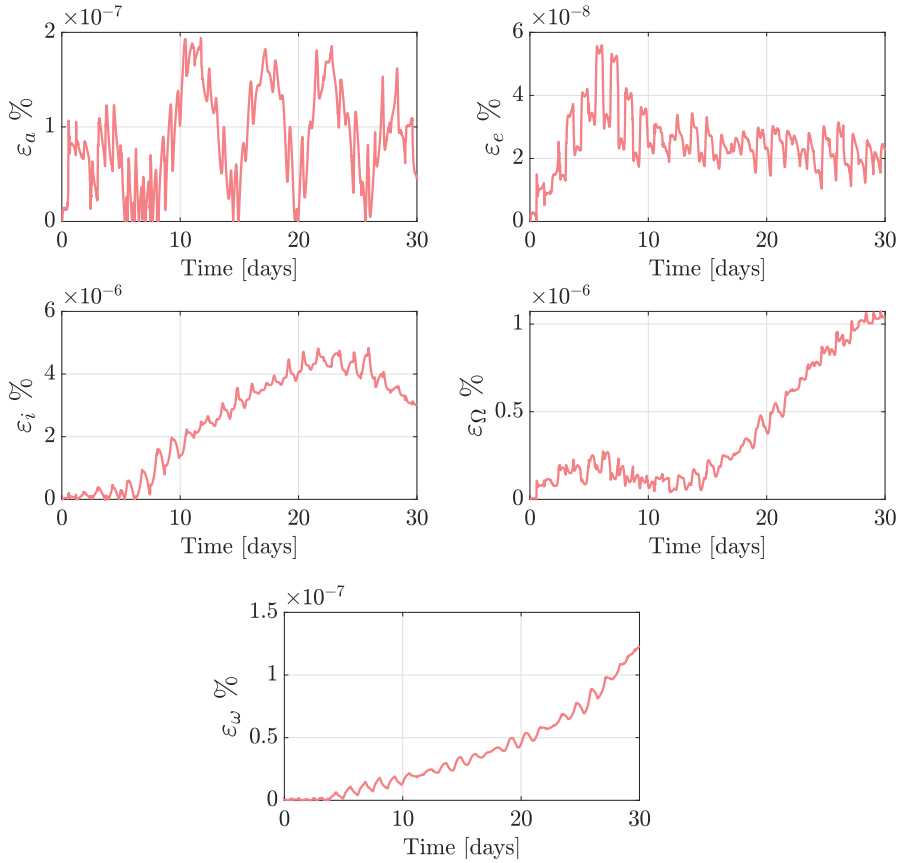

Figure 42: Relative percentage error (defined in Eq. (116)) between numerical integration of R3BP equations and LPE evolution with time for each orbital element, referred to Deimos QSO.

6.6 CPU time comparison

The last consideration that can be done on the design of a QSO throughout the Keplerian Map, concerns the smaller computational time needed to integrate the equations. In short periods propagation the difference with the numerical integration of the R3BP equations is not so relevant, since it amounts to few seconds. Whenever the number of times that the motion is propagated becomes more significant (as in the current case), the efficiency of the Keplerian Map is more evident. With the use of the Genetic Algorithm by MATLAB, the

computational times required to generate the same QSO are shown in Table 13.

Table 13: Computational time comparison required for the optimisation process aimed in finding the initial conditions of Phobos and Deimos QSO. Processor: $1.8GHz$ Intel Core i7

QSO around:	**R3BP**	**LPE with KM**
Phobos	172.7 min	140.4 min
Deimos	193.0 min	159.8 min

As it can be seen the numerical integration of the Lagrange's Planetary Equations with the Keplerian Map allows to save approximately the 18% of the time, since the optimisation algorithm reaches earlier the convergence. It is important to highlight that the comparison with the R3BP in the Genetic Algorithm is carried out with the same "random points" evaluated at each generation. Indeed, in MATLAB the random numbers generation is not truly random, but it works pseudo-random number generating algorithm. Each time that the optimisation algorithm is launched, it is possible to force the random number generation to be restarted equal to the one in the previous case. This is what is done in Monte Carlo simulation or in simulation-based optimisation procedures, when there is the needing to compare the results obtained with successive launches of the algorithm that works with random points evaluations.

CHAPTER 7

Conclusions and Further Developments

THE studies presented in this thesis were focused on searching for a domain in which the theory of the Keplerian Map could be used successfully, without introducing a significant error on the propagation of the particle's trajectory. The analysis has been carried out looking at the problem from different perspectives, exploring the behavior of the error in function of different system parameters.

From the previous works that developed the Keplerian Map theory and demonstrated its validity in particular cases, a further step has been done in determining in which scenarios this approach can be adopted. If previously it was thought that the theory could not be applied for close encounters in which the particle crosses the third body sphere of influence, from this novel study it can be stated that also the energy of the particle with respect to the third body plays a significant role. The most relevant result remains the confirmation that for heavy systems (with high mass parameter), the Keplerian Map cannot be adopted if the required accuracy on the prediction is stringent. As explained through the work, this limit is due to the definition of the mathematical model itself: the disturbing function considers the orbital elements with respect to the barycentre of the system, whilst the use of the Lagrange's Planetary Equations requires to express it with respect to the primary. However, it has been demonstrated that whenever the mass of the secondary attractor is sufficiently small, it is possible to apply the approach efficiently, assuring an high accuracy on the prediction.

The only off-limits case in which the theory cannot be applied for a long period propagation remains the Earth-Moon system. In this case the effect of the Moon is so strong on the spacecraft's dynamics that a different method shall be used to approximate the solution of the three-body problem. A possible al-

ternative to the Keplerian Map in this case could be the numerical integration of the Lagrange's Planetary Equations in their hyperbolic form, in which the disturbing potential is expressed with respect to third body and the primary is considered as perturbing body. This method might be used when the particle enters the third body sphere of influence, and then the switching to the Keplerian Map is performed when the probe exits from it. Studies on this possible application have been carried out in the current work, but the final results shown that this approach seems not to be a more accurate alternative than the Keplerian Map. The problem might be the erroneous concept of sphere of influence that has poor meaning in systems in which the secondary attractor has significant mass (as in the Earth-Moon system). Further studies are suggested in this direction, trying to replace this concept with another "switch condition", such that an efficient numerical propagator can be used even in the Earth-Moon system.

A completely novel application of the Keplerian Map theory was presented in this work. The Martian system fulfill the requirements in terms of mass parameter to apply the approach, and the use of an optimisation algorithm to identify Quasi-Satellite Orbits highlighted that the Keplerian Map is a considerable time-saving method when an high number of propagation is needed, granting predictions with high accuracy. Other possible scenarios in which the same procedure can be applied to identify a QSO are the Jupiter system and the Saturn system.

Another possible continuation of the studies on the applicability domain of the Keplerian Map can be the sensitivity analysis on other system parameters. As mentioned in the related chapter, other error maps were built varying different quantities as the Tisserand parameter, the initial phasing angle and the resonance ratio. No dependencies of the error on them have been found, but deeper studies of the effect of such quantities can be carried out trying to confirm or deny this result.

Thanks to this work a further step has been done to achieve the final goal of developing a propagator aimed in approximating the solution of the three-body problem exploiting different methods, in which the main protagonist is the Keplerian Map theory.

References

[1] H. D. Curtis, *Orbital Mechanics for Engineering Students*, 4th ed. Elsevier, 2014, ch. 3,5,8.

[2] D. J. Scheeres, *Orbital Motion in Strongly Perturbed Environments*. Elsevier, 2012.

[3] W. S. Koon, M. W. Lo, J. E. Mardsen, and S. D. Ross, *Dynamical Systems, The Three-Body Problem, and Space Mission Design*. 2006, ch. 2,4.

[4] D. A. Vallado, *Foundamental of astrodynamics and applications*, 1st ed. McGraw-Hill, 1997, ch. 2,7.

[5] S. D. Ross and D. J. Scheeres, "Multiple Gravity Assists in the Restricted Three-Body Problem," *SIAM Journal on Applied Dynamics Systems*, vol. 6, no. 3, pp. 576–596, 2007. DOI: https://doi.org/10.1137/060663374.

[6] R. H. Battin, *An Introduction to the Mathematics and Methods of Astrodynamics*, 1st ed. AIAA, 1999, ch. 10.

[7] B. Kaufman, "Higher order theory for long-term behavior of Earth and Lunar orbiters," *National Technical Information Service*, 1972. DOI: 10.21236/ad0754738.

[8] C. Colombo, "Planetary Orbital Dynamics (PlanODyn) Suite for Long Term Propagation in Perturbed Environment," *6th International Conference on Astrodynamics Tools and Techniques (ICATT)*, Mar. 2016, Darmstadt (Germany).

[9] ——, "Long-Term Evolutions of Highly-Elliptical Orbits: Luni-Solar Perturbation Effects for Stability and Re-Entry," *Frontiers in Astronomy and Space Sciences*, vol. 6, no. 34, p. 34, 2019. DOI: https://doi.org/10.3389/fspas.2019.00034.

[10] R. Neves, *Multi-Fidelity Modelling of Low-Energy Trajectories for Space Mission Design*. Cranfield University, 2019. [Online]. Available: https://arxiv.org/abs/2006.03872.

[11] T. Y. Petrosky and R. Broucke, "Area-Preserving Mapping and Deterministic Chaos for Nearly Parabolic Motions," *Celestial Mechanics*, vol. 42, pp. 53–79, 1988. DOI: https://doi.org/10.1007/BF01232948.

[12] T. Y. Petrosky, "Chaos and Cometary Clouds in the Solar System," *Physics Letters A*, vol. 117, no. 7, pp. 328–332, 1988. DOI: https://doi.org/10.1016/0375-9601(86)90673-0.

[13] E. M. Alessi, "Semi-Analytical Approach for Distant Encounters in the Spatial Circular Restricted Three-Body Problem," *Journal of Guidance, Control, and Dynamics*, vol. 39, no. 2, pp. 351–359, 2015. DOI: https://doi.org/10.2514/1.G001237.

[14] R. Neves, J.-P. Sánchez, C. Colombo, and E. M. Alessi, "Analytical and Semi-Analytical Approaches to the Third-Body Perturbation in Nearly Co-Orbital Regimes," *69th International Astronautical Congress*, Oct. 2018, Bremen (Germany).

[15] R. Neves, "Techniques for Distant Encounters in the Circular-Restricted Three-Body Problem: The Keplerian Map - Work Report," 2018.

[16] J. P. S. Cuartielles, C. Colombo, and E. M. Alessi, "Semi-Analytical Perturbative approaches to third body Resonant Trajectories," *66th International Astronautical Congress*, Oct. 2015, Jerusalem (Israel).

[17] L. Giudici, "Keplerian map theory for high-fidelity prediction of the third-body perturbative effect," *Politecnico di Milano, School of Industrial and Information Engineering, Department of Aerospace Science and Technology, Master thesis in Space Engineering, Supervison: Camilla Colombo*, 2020.

[18] E. S. Agency. (). "JUpiter ICy moons Explorer (JUICE) mission overview," [Online]. Available: https://sci.esa.int/juice.

[19] G. B. Valsecchi, E. M. Alessi, and A. Rossi, "An analytical solution for the Swing-By Problem," *Celestial Mechanics and Dynamical Astronomy*, vol. 123, pp. 151–166, 2015. DOI: https://doi.org/10.1007/s10569-015-9631-6.

[20] G. B. Valsecchi, "Geometric Conditions for Quasi-Collisions in Öpik's Theory," *Lecture Notes in Physics*, vol. 682, 2006. DOI: https://doi.org/10.1007/3-540-32455-0_6.

[21] G. B. Valsecchi, A. Milani, G. F. Gronchi, and S. R. Chesley, "Resonant returns to close approaches: Analytical theory," *Astronomy and Astrophysics*, vol. 408, no. 3, pp. 1179–1196, 2003. DOI: https://doi.org/10.1051/0004-6361:20031039.

[22] P. J. S. Gil and J. Schwartz, "Stable Orbits About the Martian Moons," *Journal of Guidance, Control, and Dynamics*, vol. 16, no. 3, 2010. DOI: https://doi.org/10.2514/3.21028.

[23] P. E. El'yasberg, *Introduction to the Theory of Flight of Artificial Earth Satellites*. (Translated from Russian). NASA, 1967.

[24] A. J. Hobson, *Just the Maths*, 1st ed. 2008, ch. 17.7.

[25] F. M. Denaro, *Metodi di calcolo numerico per l'ingegneria*. Liguori Editore, 2004.

[26] F. Topputo, *Modelling and Simulation of Aerospace Systems: Lectur Notes*. 2021.

[27] NASA. (). "Jet Propulsion Laboratory's solar system dynamics website," [Online]. Available: http://ssd.jpl.nasa.gov/.

[28] ——, (). "Jet Propulsion Laboratory's Horizons system," [Online]. Available: https://ssd.jpl.nasa.gov/horizons/.

[29] N. J. Rappaport, G. Giampieri, and J. D. Anderson, "Perturbations of a Spacecraft Orbit during an Hyperbolic flyby," *Icarus*, vol. 150, pp. 168–180, 2000. DOI: 10.1006/icar.2000.6559.

[30] S. F. Dermott and C. D. Murray, "The dynamics of tadpole and horseshoe orbits: I. Theory," *Icarus, Volume 48*, vol. 48, no. 1, pp. 1–11, 1981. DOI: https://doi.org/10.1016/0019-1035(81)90147-0.

[31] S. Spiridonova, K. Wickhusen, R. Kahle, and J. Oberst, "Quasi-Satellite Orbits around Deimos and Phobos motivated by the DePhine Mission Proposal," *Advances in Space Research*, Jun. 2017, Matsuyama (Japan).

[32] W. E. Wiesel, "Stable Orbits About the Martian Moons," *Journal of Guidance, Control, and Dynamics*, vol. 16, no. 3, 1993. DOI: https://doi.org/10.2514/3.21028.

[33] J. Oberst, K. Wickhusen, K. Willner, K. Gwinner, S. Spiridonova, R. Kahle, A. Coates, A. Herique, D. Plettemeier, M. Díaz-Mechelena, A. Zakharov, Y. Futaana, M. Pätzold, P. Rosenblatt, D. J. Lawrence, V. Lainey, A. Gibbings, and I. Gerth, "DePhine: The Deimos and Phobos Interior Explorer," *Advances in Space Research*, vol. 62, no. 8, pp. 2220–2238, 2018. DOI: https://doi.org/10.1016/j.asr.2017.12.028.

[34] NASA. (). "NAIF: SPICE toolkit main page," [Online]. Available: https://naif.jpl.nasa.gov/naif/toolkit.

[35] ——, (). "NAIF: SPICE documentation, reference frames," [Online]. Available: https://naif.jpl.nasa.gov/pub/naif/toolkit_docs/C/req/frames.

[36] I. Suchantke, A. Soucek, F. Letizia, V. Braun, and H. Krag, "Space Sustainability in Martian Orbits: First Insights in a Technical and Regulatory Analysis," *First International Orbital Debris Conference*, vol. 7, no. 3, pp. 439–446, 2019. DOI: https://doi.org/10.1016/j.jsse.2020.07.003.

[37] V. A. Chobotov, *Orbital Mechanics*, 3rd ed. AIAA Education, 2002, ch. 8,9,10.

[38] D. R. Williams. (). "NASA Mars Fact Sheet." Visited on: 17/11/2021, [Online]. Available: https://nssdc.gsfc.nasa.gov/planetary/factsheet/marsfact.